

# **NuFact 2012**

**Monday 23 July 2012 - Saturday 28 July 2012**

**Jefferson Lab**

**and**

**The College of William and Mary**

**Proceedings**

# Table of contents

Status of RAL and CERN Proton Driver Scenarios, Thomason, J.W.G.....	1
Progress on the Neutrino Factory Target System Design, Sayed, H.K.....	5
FFAG Design for a 10 GeV Neutrino Factory for the IDS-NF, Berg, J.S.....	9
Jefferson Lab Electron Model of a Muon Recirculated Linear Accelerator, Roblin, Y.R.....	13
Neutrino-nucleus interactions, Mosel, U.....	17
Improved Measurement of Electron Antineutrino Disappearance at Daya Bay, Qian, X.....	25
Progress in the Construction of the MICE Cooling Channel, Luo, T.-H.....	32
MICE Step I: First Measurement of Emittance with Particle Physics Detectors, Blackmore, V....	36
Imaging of internal density structure of volcanoes with cosmic muon: past and recent works Miyamoto, S.....	40
Mu2e: A search for Charged Lepton Flavor Violation at FNAL, Hungerford, E.V.....	44
Toward a Higgs Factory Muon Collider, Johnson, R.P.....	48
The CERN to Frejus project: from neutrino beams to MEMPHYS, Duchesneau, D.....	52
Status of Target and Magnetic Horn Studies for the CERN to Fréjus Super Beam Vassilopoulos, N.....	56
Optimizing the neutrino factory capture section, Hansen, O.M.....	60
Opportunities for Leptonic CP Violation and Neutrino Mass Hierarchy at Medium Baselines Terranova, F.....	64
Design of an efficient cooling lattice for a Neutrino Factory, Stratakis, D.....	67
Progress Towards Parametric-Resonance Ionization Cooling in the Twin-Helix Channel Maloney, J.A.....	71

# Status Of RAL And CERN Proton Driver Scenarios

J W G Thomason<sup>1</sup>, R Garoby<sup>2</sup>, S Gilardoni<sup>2</sup>, L J Jenner<sup>3, 4</sup>, J Pasternak<sup>1, 3</sup>

<sup>1</sup>STFC, RAL, ISIS, OX11 0QX, UK

<sup>2</sup>CERN, BE/HDO, 1211 Geneva 23, Switzerland

<sup>3</sup>Imperial College, London, SW7 2BW, UK

<sup>4</sup>Fermilab, Batavia, USA

**Abstract.** The proton driver is a key component of any accelerator based neutrino facility. Possible upgrades to either the ISIS facility at RAL or the CERN accelerator chain could be envisaged as the starting point for a proton driver shared with a neutrino facility. The current status of plans will be described.

**Keywords:** Accelerator, proton driver, neutrino factory

**PACS:** 29.20.D-

## INTRODUCTION

The concept of sharing a high power (MW-class) proton driver between other facilities and a neutrino facility is an attractive, cost-effective solution which is being studied in site-specific cases, particularly in the context of the neutrino factory (NF) [1]. To meet the NF specification the proton driver will be required to deliver a multi-GeV, 4 MW proton beam at 50 Hz to the target. In addition, the NF specifies a particular time structure consisting of three short (1 – 3 ns rms) bunches separated by about 120  $\mu$ s. In order to achieve such short bunches, a dedicated bunch compression system must be designed to deal with the very strong space-charge forces.

## PLANS AT RAL

### ISIS Megawatt Upgrades

Rutherford Appleton Laboratory (RAL) is the home of ISIS, the world's most productive spallation neutron source. ISIS has two neutron producing target stations (TS-1 and TS-2), driven at 40 Hz and 10 Hz respectively by a 50 Hz, 800 MeV proton beam from a rapid cycling synchrotron (RCS), which is fed by a 70 MeV H<sup>-</sup> drift tube linac [2]. Potential upgrades of the ISIS accelerators to provide beam powers of 2 – 5 MW in the few GeV energy range could be envisaged as the starting point for a proton driver shared between a short pulse spallation neutron source and the NF. Although the requirements for the NF baseline proton energy and time structure are different from those for a spallation neutron source, an additional RCS or FFAG booster bridging the gap in proton energy and

performing appropriate bunch compression seems feasible.

After initial work to address obsolescence issues with the present ISIS linac (which could involve installation of a higher energy linac and a new optimised injection system into the present ring [3]), the next upgrade stage is a new  $\approx$ 3.2 GeV RCS that can be employed to increase the energy of the existing ISIS beam to provide powers of  $\approx$ 1 MW. This new RCS would require a new building, along with a new  $\approx$ 1 MW neutron producing target station. There are a number of possible candidates for the  $\approx$ 3.2 GeV, 50 Hz RCS, but studies are presently focused on a 3.2 GeV doublet-triplet design with five superperiods (5SP) and a 3.2 GeV triplet design with four superperiods (4SP), both of which will include features required for fast injection directly from the existing ISIS RCS, together with the option for optimised multi-turn injection from a new 800 MeV H<sup>-</sup> linac [4].

The final upgrade stage is to accumulate and accelerate beam in the  $\approx$ 3.2 GeV RCS from a new 800 MeV linac for 2 – 5 MW beams [5]. It should be noted that a significant collimation section or 'achromat' would be required after the linac to provide a suitably stable beam for injection into the RCS.

### Common Proton Driver

In a common proton driver for a neutron source and the NF, based on a 2 – 5 MW ISIS upgrade, bunches of protons are shared between the two facilities at  $\approx$ 3.2 GeV, and a dedicated RCS or FFAG booster must then accelerate the NF bunches to meet the requirements for the NF baseline. Possible bunch

sharing scenarios [6] suggest that 6.4 – 10.3 GeV RCS and FFAG booster designs are to be considered.

Booster RCS designs [7] have concentrated on achieving the necessary acceleration and bunch compression with present-day, cost-effective RCS technology, but although the preliminary lattice design has been produced a great deal of work remains to be done to produce a full conceptual scenario. FFAG options are yet to be explored, and would be based on technology which remains to be fully tested, but in principle would offer the advantage of allowing all the bunches to be extracted to the NF target with the same energy (unlike the RCS where the 120  $\mu$ s sequential extraction delay required by the NF baseline would give time for the main magnet field to vary between bunches).

The NF specification requires compression of the proton bunch length from the  $\approx$ 100 ns for the neutron source to 1 – 3 ns at the NF target. Several methods have been proposed in order to reach this goal, based on either adiabatic compression during acceleration or fast phase rotation at the end of acceleration (or in an additional compressor ring).

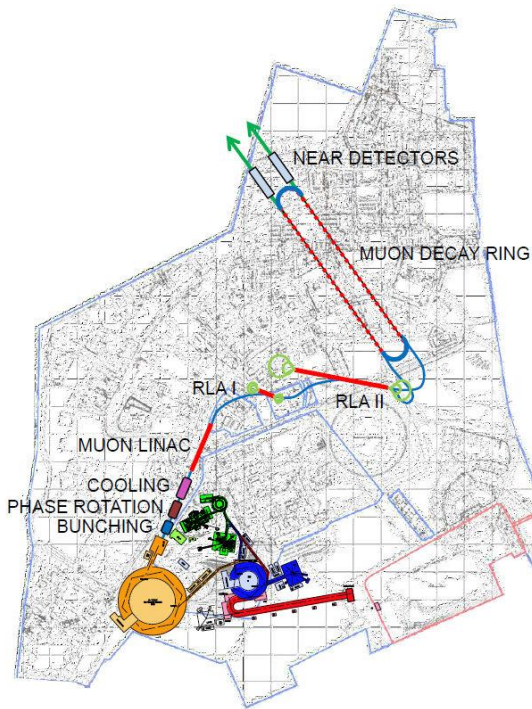


**FIGURE 1.** Schematic layout of the NF on the Harwell Oxford site with neutrino beams pointing at Norsaq in Greenland. The conceptual layout of the proton driver is shown with ISIS (green),  $\approx$ 3.2 GeV RCS (blue), 800 MeV linac (red) and dedicated NF booster (orange).

The site-specific NF design at RAL is in a preliminary stage, and will require extensive effort on

beam dynamics and accelerator engineering (and strategic research and development in a number of key areas such as high power front ends, RF systems, stripping foils, kickers and diagnostics) before it can be regarded as viable. The common proton driver could fit onto the RAL site, on land already set aside for large facilities and research expansion, but the complete NF would require the use of part of the Harwell Oxford Campus. A possible schematic layout of the NF on the Harwell Oxford site is shown in figure 1, however MW-class ISIS upgrades are unlikely to be realised in the foreseeable future unless a decision is made to site the NF at RAL, and funding for the common proton driver is forthcoming.

## PLANS AT CERN

### The Neutrino Factory

The CERN NF scenario would be based on the proposed 5 GeV, high-power version of the Superconducting Proton Linac (SPL) [8], which can deliver  $10^{14}$   $H^-$  ions at a repetition rate of 50 Hz [9]. In the recent past, the SPL study evolved into an international collaboration whose aim is the optimisation of the architecture of a pulsed superconducting high-power proton linac. The most recent design of the SPL and the description of the goals of the collaboration, can be found in [10].

In the CERN scenario, the chopped beam from the SPL would be injected into an isochronous accumulator ring in which 120 ns long bunches are formed without the need for an RF system. The absence of synchrotron motion in the accumulator ring makes it important to study the stability of the beam in the presence of space-charge. As presented in [11], transverse stability can be obtained with a suitable choice of chromaticity and longitudinal stability can be achieved by limiting the longitudinal broad-band impedance to a few ohms. Two-dimensional phase-space painting is used in the stripping injection into the accumulator ring, allowing the temperature of the stripping foil to be kept below 2000 K. The beam parameters after accumulation are obtained as a compromise between the competing requirements of minimising the heating of the injection foil, maximising the aperture, and adequate compensation of the space-charge forces and are set to allow for RF phase-rotation in the downstream compressor ring. The size of the two rings is determined by the requirement that successive bunches must arrive at the correct location in the compressor ring. The compressor ring has a large phase-slip factor, which is needed for the fast phase rotation. Tracking simulations have been performed using the ORBIT

code [12], and demonstrate good performance of the compressor ring. The simulations have also been used to investigate the transverse phase space and show that the transverse space-charge can be tolerated due to the limited number of turns of the beam in the compressor ring and the relatively large dispersion, which effectively lowers the tune shift by enlarging the beam size. More details of the CERN proton driver scenario can be found in [13]. The low energy normal-conducting part of the SPL is currently under construction under the name of “Linac4” [14], as part the LHC Injectors Upgrade Project [15] aimed at increasing the LHC luminosity during the next decade. Beam commissioning is planned in 2014-2015, followed by a reliability run. Linac4 will then be available as a replacement for the current proton linac (Linac2) as soon as the PSB has been modified for charge exchange injection at 160 MeV.

Figure 2 shows a preliminary layout of the NF on the CERN site, using the SPL followed by a transfer channel towards the accumulator and compressor rings. This geometry is constrained by the location of Linac4 and the space needed for the muon front-end and muon acceleration chain.



**FIGURE 2.** Preliminary layout of the NF on the CERN site, with neutrino beams pointing at the Pyhäsalmi mine in Finland.

## Super-Beams And Beta-Beams

As well as provision for the NF, other new proposals are being made for experiments at CERN requiring higher beam power to produce neutrinos by either exploiting the SPS or assuming the construction

of a 2 MW, 50 GeV synchrotron using the low-power SPL as the injector, or of the 4MW, 5 GeV SPL-based proton driver.

### Neutrino Experiments With Existing Accelerators

The CNGS experiment [16] is currently operating using a 500 kW proton beam from the SPS and sending neutrinos to the Gran Sasso underground laboratory 730 km away. The SPS performance is expected to improve by the end of the decade, as a result of the ongoing upgrade programme of the LHC injectors [15]. The recently started LAGUNA-LBNO Design Study [17] is aimed at making use of the increased SPS beam power, tentatively set at 750 kW, for generating a conventional  $\nu_\mu$  beam and sending it to a new underground experiment located in Pyhäsalmi (Finland), at a distance of 2300 km. Beyond the upgrade of the SPS and PS complex which is foreseen in the context of the high-luminosity upgrade of the LHC, this proposal assumes some additional improvements (under study in the context of the LAGUNA-LBNO Design Study) and the construction of a new transfer line from the SPS to a new target area and decay tunnel oriented towards Finland.

### Neutrino Experiments Based On The SPL

In the context of the LAGUNA-LBNO Design Study a High Power Proton Synchrotron (HP-PS) is being studied which would deliver 2 MW of beam power onto the target and decay tunnel first used by the SPS and aimed at Pyhäsalmi. The exact energy will be defined in interaction with the experimenters within LAGUNA-LBNO, but is expected to be in the range 30 – 50 GeV. Thereafter the accelerator will be designed using the work done for PS2 [18] [19]. The injector will be a slower cycling and hence lower power version of the SPL. Unlike PS2, the HP-PS will be dedicated to neutrino production and will not be connected to the SPS.

Another possibility is that the SPL beam is accumulated in a 200 – 300 m circumference fixed-energy ring (which does not need to be isochronous as in the NF case), using charge exchange injection. To generate a conventional low energy  $\nu_\mu$  beam from  $\pi$  decay, the beam is fast ejected from the accumulator onto the target. In such a scenario, a fraction of the linac beam ( $\approx 200$  kW) could be diverted to a radioactive ion production system of ISOL-type to generate a beta-beam [20].

## REFERENCES

1. R. J. Abrams *et al.* IDS-NF-020 (2011).

2. D. J. S. Findlay *Proc. PAC'07 (Albuquerque, USA, June 2007)* p 695 (2007).
3. C. M. Warsop *et al. Proc. IPAC'11 (San Sebastian, Spain, September 2011)* p 2760 (2011).
4. J. W. G. Thomason *et al. Proc. HB2008 (Nasville, USA, August 2008)* p 434 (2008).
5. D. C. Plostinar *et al. Proc. IPAC'11 (San Sebastian, Spain, September 2011)* p 2100 (2011).
6. J. W. G. Thomason and J. Pasternak *Proc. IPAC'11 (San Sebastian, Spain, September 2011)* p 2757 (2011).
7. J. Pasternak and L. J. Jenner *Proc. IPAC'11 (San Sebastian, Spain, September 2011)* p 2751 (2011).
8. F. Gerigk *et al.* Tech. Rep. CERN-CERN (2006).
9. R. Garoby *Proc. SRF'09 (Berlin, Germany, September 2009)* p 930 (2009).
10. F. Gerigk *et al.* Tech. Rep. CERN-ATS-CERN (2010).
11. E. Benedetto *Proc. NuFact'09 (Chicago, USA, July 2009)* p 283 (2009).
12. <http://neutrons.ornl.gov/APGroup/Codes/orbit.htm>
13. R. Garoby Tech. Rep. CERN-NEUTRINO-FACTORY-NOTE-157 (2009).
14. L. Arnaudon *et al.* Tech. Rep. CERN-AB-ABP/RF and CARE-Note-2006-022-HIPPI (2006).
15. R. Garoby *et al. Proc. IPAC'12 (New Orleans, May 2012)* p 1010 (2012).
16. K. Elsener ed. The CNGS (Conceptual Technical Design), CERN 98-02 (1998).
17. LAGUNA-LBNO Design Study European Commission 7<sup>th</sup> Framework Programme - Grant agreement no: 284518 (2011).
18. M. Benedikt, B. Goddard *Proc. PAC'09 (Vancouver, Canada, May 2009)* p 1828 (2009).
19. R. Garoby Synergies between the needs of LHC, neutrinos and Radioactive Ion Beams CERN sLHC Project Report 0034 (2010).
20. Final report of the EURISOL Design Study EUROPEAN COMMISSION CONTRACT No. 515768 RIDS, [http://www.eurisol.org/doc\\_details.php?operation=download&docu=1075](http://www.eurisol.org/doc_details.php?operation=download&docu=1075) (2009).

# Progress On The Neutrino Factory Target System Design

Hisham Kamal Sayed\*, H.G. Kirk\* and K.T. McDonald†

\*Brookhaven National Laboratory, Upton, NY 11973

†Princeton University, Joseph Henry Laboratories, Princeton University, NJ 08544

**Abstract.** The baseline target system for a Neutrino Factory or Muon Collider is a free liquid-metal (mercury) jet inside a 20-T capture solenoid magnet. A peak solenoid field of 15 T at the mercury target location is being considered as an alternative to simply the target system. The tapering field profile, from  $B_i = 15 - 20\text{-T}$  down to  $B_f = 1.5 - 2\text{-T}$  over distance  $z_f - z_i$ , is optimized to maximize the muon yield at 50 m downstream of the mercury target within a defined energy window. The axial magnetic field is specified analytically using a inverse-cubic form, and the off-axis field is computed from a series expansion based on axial derivation of the axial field. The simulation is performed using the MARS15 code, and results of the dependence of the muon yield on the field profile are discussed.

**Keywords:** Muon Target, Muon Collider, Neutrino Factory

**PACS:** 41.85.-p, 41.75.-i, 29.25.-t, 29.27.Eg

## INTRODUCTION

A Neutrino Factory offers an appealing opportunity to study neutrino oscillations with unprecedented high sensitivity [1, 2], and would be a first step towards a Muon Collider. The intense high-energy neutrinos of the Neutrino Factory are generated from a muon beam derived from the decay of pions produced in a target for a 4-MW proton beam of energy  $\approx 8 \text{ GeV}$ .

The baseline design of the Neutrino Factory (see Fig. 1) generates  $5 \times 10^{20}$  neutrinos per year in the beam directed to a distant neutrino detector [1, 2]. Low-energy pions produced in the target are captured in a 20-T solenoid magnet, which leads adiabatically into a 1.5-T solenoid channel where they decay to muons. Thereafter, the low-energy muons pass through bunching and phase rotation stages, followed by ionization cooling. Finally, muons are accelerated to 25 GeV in multiple accelerating stages and stored in a decay ring.

The current baseline design of the muon-production target system is shown in Fig 2. The target material in consideration is a liquid mercury jet which intercepts the multi-GeV proton beam within the confines of a 20-T solenoid field. The disrupted region of the mercury jet, due to the interaction with the proton beam, is replaced before the arrival of the following proton pulse, at repetition rates up to 50 Hz.

Alternative target capture-solenoid field profile have been investigated and a comparison to the current baseline is presented.

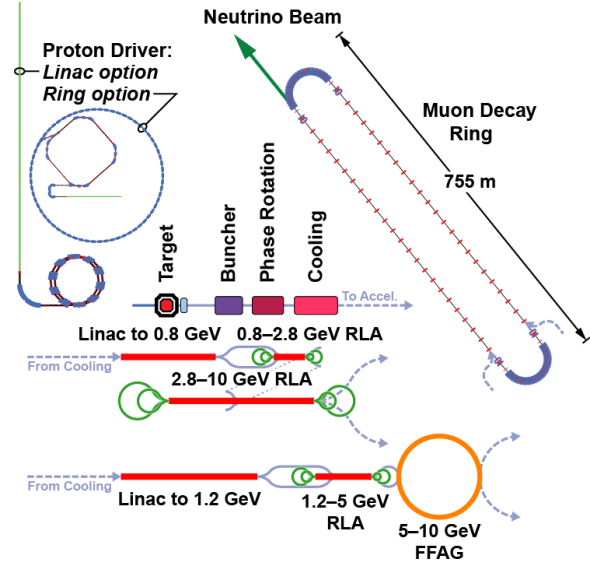


FIGURE 1. Neutrino Factory layout (From [2]).

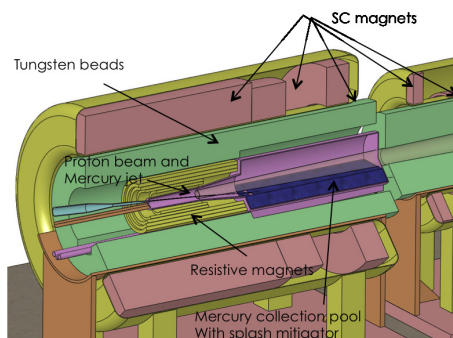


FIGURE 2. Neutrino Factory/ Muon Collider Target Layout.

**TABLE 1.** Baseline target parameters [5].

Hg Jet	Proton Beam (Gaussian Distribution)
$\theta_{\text{jet}} = 0.137 \text{ rad}$	$\theta_{\text{beam}} = 0.117 \text{ rad}$
$R_{\text{jet}} = 0.404 \text{ cm}$	$\sigma_{x,y} = 0.1212 \text{ cm}$

## THE TARGET SYSTEM

The main requirement of the target system is to deliver an intense, low-energy muon beam of  $10^{14}$  muons/s from the incident proton beam ( $\approx 4$  MW proton beam power;  $10^{15} \text{ p/c}$  at 8 GeV). The incident proton beam interacts with the mercury target jet producing pions. Low-energy pions are then collected and transported to decay channel using a tapered solenoid field. The 20-T solenoid field is generated by a set of coils (5-T copper magnet insert, 10-T Nb<sub>3</sub>Sn coil and 5-T NbTi outsert). Subsequent superconducting coils taper the field down to 1.5 T over a distance of 15 m.

The proton beam is tilted with respect to the solenoid magnetic axis (and with respect to the mercury jet), and directed to the mercury collection pool which additionally serves as the proton beam dump. Superconducting coils (particularly their organic insulation) can tolerate radiation doses up to 10 MGy (0.1 mW/g over an operational life of 10 years of  $10^7$  s each [3]). He-gas-cooled tungsten beads are used to shield the superconducting coils from radiation damage. The 4-MW beam power requires the outer radius of the shield and subsequently the inner radius of the superconducting coils near the target to be  $\approx 120$  cm [3, 4]. It is of interest to eliminate the resistive coils (which would reduce the peak field to 15 T) and use the freed space for shielding.

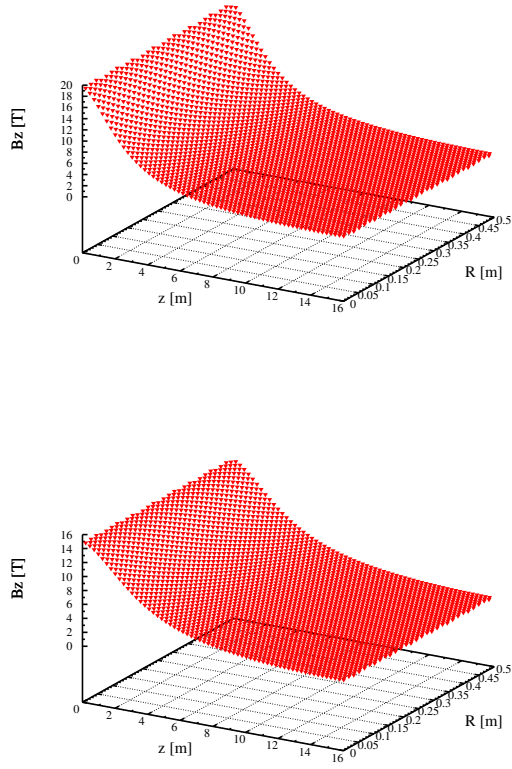
The beam-target parameters used in this study are given in Table 1 [5]. The baseline configuration of the target produces  $0.4 N_\mu / N_p$  at the end of the decay channel ( $z = 50$  m).

## Target Capture Tapered solenoid

The current baseline (20-T peak field) solenoid field along the solenoid axis is shown in Fig. 3 along with one of the proposed alternative options. Alternative solenoid field profiles effect on particle production and capture was studied. The axial field was modeled by an inverse-cubic taper eq. (1) [6].

$$B_z(0, z) = \frac{B_i}{[1 + a_1(z - z_i) + a_2(z - z_i)^2 + a_3(z - z_i)^3]^p}, \quad (1)$$

$$a_1 = -\frac{B'_i}{pB_i}, \quad (2)$$

**FIGURE 3.** 20-T and 15-T target solenoid field maps.

$$a_2 = 3 \frac{(B_i/B_f)^{1/p} - 1}{(z_f - z_i)^2} - \frac{2a_1}{z_f - z_i}, \quad (3)$$

$$a_3 = -2 \frac{(B_i/B_f)^{1/p} - 1}{(z_f - z_i)^3} - \frac{a_1}{(z_f - z_i)^2}, \quad (4)$$

where  $B_i$  and  $B_f$  are the initial (peak) and final axial fields at  $z = z_i$  and  $z_f$  respectively, and  $p$  is the power to which the cubic fit is exponentiated. The off-axis field was calculated from the series expansions, based on the axial field (1), given in eqs. (5)-(6),

$$B_z(r, z) = \sum_n (-1)^n \frac{a_0^{(2n)}(z)}{(n!)^2} \left(\frac{r}{2}\right)^{2n}, \quad (5)$$

$$B_r(r, z) = \sum_n (-1)^{n+1} \frac{a_0^{(2n+1)}(z)}{(n+1)(n!)^2} \left(\frac{r}{2}\right)^{2n+1}, \quad (6)$$

where  $a_0^{(n)}$  is the  $n$ th derivative of  $a_0$ ,

$$a_0^{(n)} = \frac{d^n a_0}{dz^n} = \frac{d^n B_z(0, z)}{dz^n}. \quad (7)$$

## MARS SIMULATION SETUP

The MARS15 simulation code [7] was used to simulate the particle production off the target. The beam-pipe geometry was simplified to have a constant 30-cm radius for  $z = 0\text{-}50$  m to simulate particle loss due to scraping.

## MUON PRODUCTION OFF THE TARGET

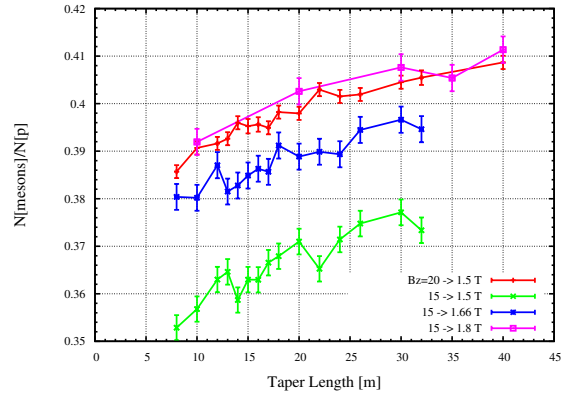
The particle production was simulated using a variety of solenoid field profiles, using peak field of 20 T and 15 T while varying the taper length ( $z_f - z_i$ ) from 5 m up to 40 m. The final constant field,  $B_f$ , was varied in 3 steps (1.5, 1.66, and 1.8 T) as well. The number of muons (and remaining pions) with kinetic energy in the range 80-140 MeV, and in the aperture  $r < 30$  cm, at  $z = 50$  m from the target (entrance to the buncher/phase rotator) was used as the figure of merit in comparing the performance of the capture solenoid profile. Future studies will use the muon yield at the end of the buncher/phase rotator as the figure of merit).

Figure 4 shows the number of positive mesons (muons and pions) as function of the taper length for various values of the axial  $B_i$ . The simulations show that  $N_{\text{meson/proton}}$  decreased by 8% when the peak solenoid field was decreased from  $B_i = 20$  to 15 T, if the final field was kept constant at  $B_f = 1.5$  T. As the final constant field was increased to 1.8 T for the 15-T peak field case, the ratio  $N_{\text{meson/proton}}$  matched that of the  $B_z = 20\text{-}1.5\text{-T}$  case.

The solenoid taper length has a distinct influence on the number of the transported meson to the decay channel. The ratio  $N_{\text{meson/proton}}$  increases linearly with the taper length, based on the figure of merit used here. As the taper length increases to 40 m,  $N_{\text{meson/proton}}$  rises by 6%.

The distribution of the meson radii at  $z = 0$ , shown in Fig. 5(top), extends out to 10 cm for peak solenoid fields of 15-20 T. In the current baseline design the aperture at the target is set to 7.5 cm. In instances where the peak solenoid field is 15 T the distribution slightly shifts to larger radii as expected; in these cases it is recommended that the aperture at the target be increased to 10 cm. As the solenoid field tapers down to 1.5 T (or 1.8 T) the maximum radius of the muon distribution extends to 30 cm.

The transverse-momentum distributions, shown in Fig. 5(bottom), verify that the target solenoid captures mesons with maximum transverse momentum of 0.25 GeV/c at the target, and the exchange of transverse and longitudinal momentum in the tapered-field region down to 1.5 T (1.8 T) reduces the spread of transverse momenta.



**FIGURE 4.** Number of positive mesons (muons and pions) counted at  $z=50$  m as a function of the solenoid taper length.

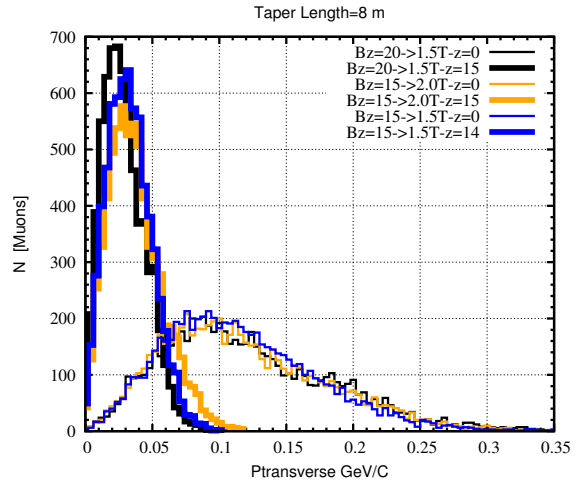
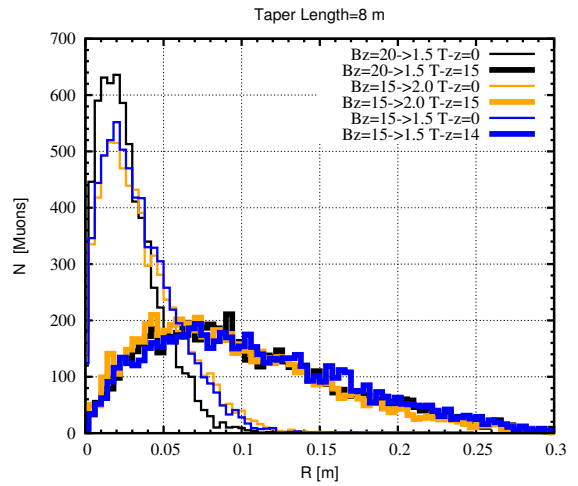


**FIGURE 5.** Distributions of meson radius (top), and of transverse momentum (bottom), at  $z = 0$  and 15 m (in bold) for three solenoid field profiles with taper length of 8 m.

## CONCLUSION

An alternative capture-solenoid field has been studied for the mercury jet target for a Neutrino Factory or Muon Collider. The influence of the field strength and the taper length on the meson yield within KE of 80-140 MeV at  $z = 50$  m downstream from the target was examined.

The solenoid field profile with 15-T peak at the mercury-target location was studied in comparison to the current baseline value of 20 T. Three parameters were considered for optimization; the taper length,  $z_f - z_i$ , and the tapered field strength in both ends,  $B_i$  and  $B_f$ . The axial magnetic field profile was specified analytically using an inverse-cubic equation and the off-axis field was computed from a series expansion. Particle transport and decay simulations were performed using the MARS15 code. We found that using a field taper of 15 down to 1.8 T will result in the capture of the same number of mesons as the baseline case of 20 down to 1.5 T, according to the criteria used for particle yield as  $z = 50$  m. In addition, we found that a 10-cm aperture at the target location would be sufficient for if the peak field were reduced to 15 T.

## ACKNOWLEDGMENTS

This work was supported in part by the US DOE Contract No. DE-AC02-98CHI10886.

## REFERENCES

1. A. Bandyopadhyay *et al.*, *Physics at a future Neutrino Factory and super-beam facility*, Rep. Prog. Phys. **72**, 106201 (2009).
2. S. Choubey *et al.*, *International Design Study for the Neutrino Factory: First Progress Report*, IDS-NF-017 (2010), <http://www.cap.bnl.gov/mumu/IDS/IDS-ProgRep-2014-16.pdf>
3. N. Souchlas *et al.*, *Energy Flow and Deposition in a 4-MW Muon-Collider Target System*, Proc. IPAC12, p. 2588.
4. R.J. Weggel *et al.*, *Shielding of Superconducting Coils for a 4-MW Muon-Collider Target System*, Proc. IPAC12, p. 2591.
5. X. Ding *et al.*, *Optimization of a mercury jet target for a neutrino factory or a muon collider* Phys. Rev. STAB **14**, 111002 (2011).
6. K.T. McDonald, *Analytic Forms for an Adiabatic Tapered Solenoid Gaussian Approximation to the Field Near  $z = 0$* , <http://www.hep.princeton.edu/~mcdonald/mumu/target/taper.pdf>
7. N. Mokhov and N. Krivosheev, *The MARS Code System* (2010), <http://www-ap.fnal.gov/MARS/>

# FFAG Design for a 10 GeV Neutrino Factory for the IDS-NF

J. Scott Berg

*Brookhaven National Laboratory; Building 901A; PO Box 5000; Upton, NY 11973-5000; USA*

**Abstract.** I give the design parameters for a linear non-scaling FFAG optimized to accelerate the IDS-NF muon beam from 5 to 10 GeV. The results are given for several values of the long drift length. The corresponding parameters for a 12.6 to 25 GeV FFAG are also given. For a 10 GeV neutrino factory, I analyze the choice between scenarios with or without an FFAG in the acceleration chain.

**Keywords:** fixed field alternating gradient accelerator, neutrino factory

**PACS:** 29.20.-c

## 5–10 GEV FFAG DESIGN

In [1], a design for a 12.6–25 GeV FFAG for a neutrino factory is described. Recent physics results [2, 3] have led to a reduction in the maximum energy of a neutrino factory to 10 GeV [4].

I designed an optimized lattice for a 5–10 GeV FFAG using an identical optimization procedure to the lattice in [1]. The choice of a factor of 2 in energy is based on past studies which indicated that a factor of 2 was near optimal: when a sequence of 2, 3, or 4 FFAGs was used to accelerate a neutrino factory beam by a factor of 8 in energy, each FFAG accelerating by an equal factor in energy, the sequence of 3 had the lowest cost, the sequence of 4 had a somewhat higher cost, and the sequence of 2 had a significantly higher cost.

Due to the smaller energy range, the  $a$  parameter (see [5]) needs to be 0.1120, higher than the 0.074827 that was used for the 12.6–25 GeV FFAG (these both correspond to approximately a 5% longitudinal emittance distortion in the approximation that the time of flight is perfectly parabolic). In both cases we leave 17 drifts free for injection, extraction, and utilities (4 drifts are allocated to this). One may be able to accomplish injection and extraction with fewer cells in the 5–10 GeV case than in the 12.6–25 GeV case; that should be investigated. All remaining cells contain an RF cavity to maximize the average accelerating gradient per cell, so as to minimize the effect of transverse amplitude on the time of flight [6]. The cost described in [7] is minimized. With a double cell cavity, engineering drawings indicate that it would be difficult to make the long drift much less than 4.3 m. The design for a machine with this drift length is given in Table 1, and compared with the design for a 12.6–25 GeV FFAG. I also give designs for reduced long drift lengths to indicate the benefit of reducing that drift length. Note that for the design with the 4.3 m drift, the beam may be too large to fit within the 30 cm aperture of the 25.5 MV cavities, and we may therefore require lower gradient cav-

ities.

While one could make a design which has more turns, that would require an increase in the circumference and a reduction in the amount of RF in the machine. This would reduce the machine cost, both due to less RF and a reduction in the magnet apertures and fields (which overcomes the cost of additional magnets). However, this would further reduce the energy gain per cell, (already lower than what we had for the 12.6–25 GeV FFAG), thus increasing the effect of the transverse amplitude on the longitudinal motion [6]. This effect is already difficult to deal with based on our tracking results thus far, and I think it is a bad idea to exacerbate it.

We wish to compare the cost of an acceleration system with a linac and two RLAs to the cost of an acceleration system with a linac, one RLA, and an FFAG. Starting with the energy breakpoints for the IDS-NF baseline linac and RLA designs [8], I estimate that for the acceleration scenario without an FFAG, the linac will accelerate to a total energy of 0.8 GeV and the first RLA to 2.8 GeV. With the FFAG, the linac will instead accelerate to 1.2 GeV. Starting on a preliminary costing [9, 10] of the 25 GeV facility, I scale the FFAG cost according to the cost line in Table 1; for the linac I divide the cost by the number of cells, then multiply by the ratio of the difference in energy gain to the energy gained in the final cell of the IDS-NF design. This is used because the beam is close to the crest near the end of the linac. For the RLAs, I linearly interpolate the cost per GeV in the inverse of the high energy value, then multiply by the actual energy gain. The results are shown in Table 2. The difference between the costs for the two scenarios accelerating to 10 GeV is much less than the uncertainty of this calculation. I therefore see no cost advantage in using an FFAG. Applying this same cost scaling to a scenario accelerating to 25 GeV with either two or three RLAs shows a clear advantage in using the FFAG.

Table 1 gives stored energies for the magnets for both systems. The stored energies in the magnets appears to

**TABLE 1.** Parameters for the FFAG designs.

Injection energy (GeV)	12.6	5	5	5	5	5	5	5
Extraction energy (GeV)	25	10	10	10	10	10	10	10
Long drift (m)	5.0	4.3	4.0	3.8	3.6	3.4	3.2	3.0
Short drift (m)	0.75	0.75	0.75	0.75	0.75	0.75	0.75	0.75
Cells	67	55	53	53	53	53	51	51
D length (m)	1.994466	1.620155	1.407454	1.481612	1.550139	1.614460	1.375857	1.437968
D angle (mrad)	147.626	179.015	184.550	183.086	181.829	180.725	186.552	185.440
D shift (mm)	39.012	44.874	43.635	43.414	43.224	43.069	41.563	41.277
D field (T)	4.43410	2.60811	3.07698	2.91080	2.77279	2.65478	3.19420	3.04971
D gradient (T/m)	-14.0598	-7.3583	-9.0320	-8.4690	-7.9849	-7.5614	-9.5610	-9.0156
F length (m)	0.965155	0.756990	0.641052	0.703935	0.769636	0.837441	0.684476	0.753383
F angle (mrad)	-26.924	-32.388	-32.999	-32.268	-31.639	-31.087	-31.676	-31.120
F shift (mm)	14.371	17.141	16.322	15.893	15.450	14.986	14.245	13.747
F field (T)	-1.43705	-0.87525	-1.05424	-0.94040	-0.84563	-0.76625	-0.95533	-0.85640
F gradient (T/m)	18.8800	10.1626	12.9054	11.5936	10.4508	9.4611	12.6004	11.2634
Cavities	50	38	36	36	36	36	34	34
RF voltage (MV)	1212.571	905.740	859.522	864.833	871.983	880.459	826.089	835.383
turns	11.6	6.4	6.7	6.7	6.6	6.6	7.0	6.9
D radius (mm)	130	175	169	167	165	163	157	156
D max field (T)	6.3	3.9	4.6	4.3	4.1	3.9	4.7	4.5
D stored energy (kJ)	899	473	534	489	451	419	480	450
F radius (mm)	160	205	195	198	201	204	192	195
F max field (T)	4.5	3.0	3.6	3.2	2.9	2.7	3.4	3.1
F stored energy (kJ)	204	117	130	121	114	107	121	113
Circumference (m)	699	492	434	434	434	434	380	380
Decay (%)	7.0	6.8	6.4	6.3	6.3	6.2	5.8	5.7
Energy gain/cell (MV)	15.9	14.2	14.0	14.1	14.2	14.3	14.0	14.1
Cost (A.U.)	162	130	128	124	122	120	118	115

**TABLE 2.** Cost comparison of acceleration scenarios. Numbers in the first column are percentage values from [10]; other numbers are scaled from them as described in the text.

Linac	11	16.9	9.0	10.0	14.0
Energy (GeV)	0.9	1.5	0.7	0.8	1.2
RLA 1	18	25.2	13.1	14.8	22.5
Energy (GeV)	3.6	6.0	2.3	2.8	5.0
RLA 2	43	83.7	28.0	35.8	
Energy (GeV)	12.6		7.6		
RLA 3			76.6		
Energy (GeV)	29			23.3	
FFAG	25.0	25.0	25.0	10.0	10.0
Total	101	125.8	126.7	60.7	59.8

vary more strongly than the costs for the systems. This is partly due to the cost model used [7]: in that model, the cost of a magnet does not go to zero as its length goes to zero, which is based on the observation that a short, large aperture magnet is dominated by the cost of the magnet ends.

There are (at least) two deficiencies in this design that need to be corrected. The first is that the number of turns should be a half integer. The second is that the design has not been properly optimized for a time of flight which is not a purely parabolic function of energy. Nonetheless, I

expect the final designs to be similar to the ones shown here.

## SYSTEM WITH A 4 GEV BREAKPOINT

Instead of completely constructing a 10 GeV neutrino factory in one shot, one might like to have intermediate stages where one could perform useful physics. In the scenarios above, the FFAG-based scenario has a natural breakpoint at 5 GeV. In addition, there are natural breakpoints at 1.2 GeV, 1.6 GeV, 3.3 GeV (corresponding to 0, 0.5, and 2.5 passes through the linac in the first RLA) corresponding to delays in constructing parts of the second RLA. In fact, any intermediate energy in that first RLA should be achievable.

However, the question was raised whether one could have a lower cost option by choosing a breakpoint at 4 GeV. The argument (J. Pasternak) is that the reduction in cost of the relatively inefficient lower energy stages outweighs the increase in cost of the FFAG, even if the FFAG becomes less efficient.

An FFAG was designed at this energy, and its parameters are given in Table. There was a significant cost increase from the 5 GeV FFAG, and the design could only achieve a small number of turns. The reason for this is

**TABLE 3.** Parameters of a 4-10 GeV FFAG design

Injection energy (GeV)	4
Extraction energy (GeV)	10
Long drift (m)	4.3
Short drift (m)	0.75
Cells	83
D length (m)	1.608696
D angle (mrad)	113.489
D shift (mm)	45.220
D field (T)	1.58481
D gradient (T/m)	-5.9657
F length (m)	0.763496
F angle (mrad)	-18.894
F shift (mm)	11.476
F field (T)	-0.52225
F gradient (T/m)	7.6329
Cavities	67
RF voltage (MV)	1637.213
turns	4.1
D radius (mm)	203
D max field (T)	2.8
D stored energy (kJ)	269
F radius (mm)	241
F max field (T)	2.4
F stored energy (kJ)	109
Circumference (m)	742
Decay (%)	7.4
Energy gain/cell (MV)	17.4
Cost (A.U.)	206

**TABLE 4.** Costs of acceleration scenarios with a 4 GeV breakpoint.

Linac	12	12
Energy (GeV)	1	1
RLA 1	19.2	19.2
Energy (GeV)	4	4
RLA 2	29.8	
FFAG		36.9
Energy (GeV)	10	10
Total	61.0	68.1

likely twofold: first, that the increase in the energy range increased the time of flight range (which is a quadratic function of the energy range). This requires more RF voltage in proportion to that time of flight increase to have a tolerable longitudinal emittance distortion [5]. The second reason for the cost increase is that the tune range has increased, meaning that the beta functions will be larger at the two energy extremes: at the low end because one approaches the half integer resonance, and at the high end due to the weaker focusing. The result is an increased magnet aperture and therefore an increased cost.

Table 4 shows a cost comparison between acceleration scenarios with a 4 GeV breakpoint. The cost of an RLA scenario is similar to what one would have with the

5 GeV breakpoint. However, the FFAG scenario suffers a significant cost increase. The scenarios are relatively close in cost considering the accuracy of this estimate, but the fact that the cost of the FFAG scenario increases when reducing the lower energy from 5 to 4 is clear.

The cost comparison implicitly assumed that the RLA-only scenario used 4.5 linac passes for the second RLA. However, due to the relatively small energy range (only a factor of 2.5), the switchyard might get too dense with 4.5 passes. Thus one might be forced to fewer passes (if 4.5 passes were possible, one might question whether more passes would be possible with a larger energy range in the RLAs), and the cost would rise. Thus, 4 GeV appears to be a particularly inconvenient energy breakpoint in the acceleration scenario.

## CHOICE OF AN ACCELERATION SCENARIO

- A higher energy is preferable to a lower one for detector performance.
- The choice between a RLA-only scenario and a scenario with an FFAG with a 5 GeV breakpoint is cost-neutral
- The performance concerns with an FFAG, namely the longitudinal distortion resulting from the time of flight dependence on transverse amplitude, may very well appear in the RLAs as well, since they have no chromaticity correction (though they do have some synchrotron oscillation, which will change the nature of the effect). We have not done sufficient tracking studies at this point to know one way or another.
- The scenario with a acceleration 5 GeV breakpoint provides a set of convenient intermediate breakpoints where one could stop construction (before installing RLA arcs) and do physics.
- The RLA-only scenario would require either partially constructing the second RLA to get to the 5 GeV energy, or would require that the first RLA be designed to 5 GeV, then some of the linac from the first RLA would be moved to the second RLA.

The primary argument against the scenario with an FFAG is that it adds a different type of accelerator to the machine, without a well-defined cost benefit. The last bullet above provides a path to accelerate to 5 GeV with the same cost as the FFAG scenario. However, the cost to reach 10 GeV will be somewhat higher in this scenario, since the arcs will need to be designed for 5 GeV instead of 2.8 GeV and there will be a longer focusing channel in the straight of the first RLA. In addition, there will be more decays. Furthermore, the modifications to that first RLA will require re-commissioning that machine when

moving to the 10 GeV, potentially negating some of the operational benefit of not having an FFAG. FFAGs are also likely to be useful for a muon collider, so one will need to gain operational experience with them eventually. An additional concern is the longitudinal distortion from one FFAG stage making the next FFAG stage more difficult, but as pointed out above, it is not clear that this effect is absent from the RLAs.

## Post-Conference Discussions

At an IDS-NF plenary meeting following the NuFact conference, discussions within the physics and detector community led to the conclusion that having an intermediate energy breakpoint below 10 GeV was not of interest. This eliminated the primary benefit of having the FFAG in the acceleration scenario for a 10 GeV neutrino factory. It was therefore decided to have an acceleration scenario with a linac and two RLAs for the IDS-NF neutrino factory (10 GeV) design.

## ACKNOWLEDGEMENTS

Some of the arguments here arose from discussion with colleagues at NuFact 2012. In particular I should mention Michael Zisman, Jaroslaw Pasternak, Patrick Huber, and Ken Long.

This manuscript has been authored by employees of Brookhaven Science Associates, LLC under Contract No. DE-AC02-98CH10886 with the U.S. Department of Energy. The United States Government retains a non-exclusive, paid-up, irrevocable, world-wide license to publish or reproduce the published form of this manuscript, or allow others to do so, for United States Government purposes.

## REFERENCES

5. J. Scott Berg, “Minimizing Longitudinal Distortion in a Nearly Isochronous Linear Nonscaling Fixed-Field Alternating Gradient Accelerator,” *Phys. Rev. ST Accel. Beams* **9**, 034001 (2006).
  6. J. Scott Berg, “Amplitude Dependence of Time of Flight and its Connection to Chromaticity,” *Nucl. Instrum. Methods A* **570** (2007) 15.
  7. Robert B. Palmer and J. Scott Berg, “A Model for Determining Dipole, Quadrupole, and Combined Function Magnet Costs,” in *Proceedings of EPAC04, Lucerne, Switzerland* (EPAC, EPS-AG, 2004) 902.
  8. R. J. Abrams *et al.* (The IDS-NF Collaboration), “Interim Design Report,” IDS-NF-020, arXiv:1112.2853 (2011).
  9. A. Kurup, N. Bliss, N. Collomb, and A. Grant, “Costing Methodology and Status of the Neutrino Factory,” to appear in the proceedings of the 2012 International Particle Accelerator Conference, New Orleans, LA, USA, May 20–25, 2012.
  10. Ajit Kurup, “Status of Costing the Neutrino Factory Accelerator Facility,” presentation at the 8th Plenary Meeting of the IDS-NF, April 18, 2012, <https://www.ids-nf.org/wiki/GLA-2012-04-18>.
1. J. S. Berg *et al.*, “Status of the Non-Scaling Fixed Field Alternating Gradient Ring Design for the International Design Study of the Neutrino Factory,” to appear in the proceedings of the 2012 International Particle Accelerator Conference, New Orleans, LA, USA, May 20–25, 2012.
  2. F. P. An *et al.*, “Observation of Electron-Antineutrino Disappearance at Daya Bay,” *Phys. Rev. Lett.* **108**, 171803 (2012).
  3. J. K. Ahn *et al.* (Reno Collaboration), “Observation of Reactor Electron Antineutrinos Disappearance in the RENO Experiment,” *Phys. Rev. Lett.* **108**, 191802 (2012).
  4. K. Long, J. Pozimski, and J. S. Berg, “The International Design Study for the Neutrino Factory,” to appear in the proceedings of the 2012 International Particle Accelerator Conference, New Orleans, LA, USA, May 20–25, 2012.

# Jefferson Lab Electron Model of a Muon Recirculated Linear Accelerator\*

Y. R. Roblin<sup>1</sup>, V. Morozov<sup>1</sup>, A. Bogacz<sup>1</sup>, K. Beard<sup>2</sup>, R. Rousset<sup>3</sup>

<sup>1</sup>*Jefferson Lab, Newport News, VA 23606,*

<sup>2</sup>*Muons, Inc., Batavia, IL,*

<sup>3</sup>*Rensselaer Polytechnic Institute, Troy, NY 12180*

(Dated: November 27, 2012)

Neutrino factories (NF) and Muon Colliders (MC) require rapid acceleration of muon beams. A recirculating linear accelerator (RLA) together with high momentum acceptance recirculating arcs designed to transport more than one orbit, provides a fast and economical means of achieving this goal. We propose to test this concept by building a small machine, Jefferson Lab Electron Model of a Muon Recirculating Linear Accelerator (JEMMRLA). Scaling the muon momentum by the muon to electron mass ratio and changing the RF frequency from 200 MHz to 1.5 GHz leads to a compact machine which fits in a 25x7 m footprint.

The electron beam of initial momentum of 4.5 MeV/c is injected at the center of a linac comprised of two 1.5 Ghz cavities. The recirculating arcs are made of fixed field combined function magnets providing quadrupole and dipole fields.

## I. INTRODUCTION

Neutrino oscillations are currently one of the most exciting and promising axis of research in high energy physics. Previous experiments have focussed on studying oscillations coming from neutrinos produced by the sun, cosmic rays interactions with the atmosphere and nuclear reactors.

According to the standard model, neutrinos come in three flavors and oscillate between these states. The amount of mixing amongst these flavors is indicative of whether or not CP symmetry is violated which in itself has consequences regarding the distribution of matter and anti-matter in the universe.

The abundance of neutrinos in the universe also raises questions regarding their contributions to the dark matter, another extensively debated topic.

Finally, the question of whether or not a neutrino is distinguishable from an anti-neutrino is being investigated.

In order to best explore these questions, it became clear that a neutrino factory was needed.

The International Neutrino Factory Design Study[1] was created in 2007 to explore the physics and publish an initial design report for such a machine.

The IDS collaboration formed working groups, one of which being the accelerator working group. Within this group, we proposed and designed the first stage of acceleration of the muons based of the concept of recirculated linacs (RLA).

## A. Motivation

In order to arrive at an efficient design for the neutrino factory, research and development has to be conducted. In particular, test machines and experiments have been proposed and built to demonstrate critical aspects. MERIT [2], MICE [3] and EMMA [4] are such experiments. They respectively tested the mercury jet target, the ionization cooling channel and the acceleration of the muons with a FFAG.

In the same spirit, we are proposing to build a small electron machine, Jefferson Lab Electron Model of a Muon RLA (JEMMRLA) to demonstrate the concept of muon RLA acceleration at a smaller scale substituting electrons for muons.

RLA are a very attractive choice for the early acceleration of the muon beam. Namely, they are able to tolerate phase slippage (up to 20deg), possess large acceptance and also provide longitudinal compression thereby reducing the momentum spread. The RF is efficiently utilized by maximizing the number of recirculations. This can be accomplished by introducing mirror symmetric quadrupole focusing in the linac [5], pulsing the quadrupoles [6] and designing multipass return arcs to eliminate or simplify the use of switchyards present in conventional recirculated machines such as CEBAF[7].

## II. MUON ACCELERATION

The neutrino factory concept has been described [1] elsewhere. In short, a proton beam is applied to a high Z target (mercury for example) and produces pions in a wide energy and phase space range. These are collected and then sent to a decay channel where muons are generated. After various longitudinal phase space manipulations and transverse emittance cooling, both species of muons are accelerated by a first stage linac followed by a RLA and finally a FFAG ring to a final momentum of around 10 GeV. The resulting muons are directed to a

---

\*Notice: Authored by Jefferson Science Associates, LLC under U.S. DOE Contract No. DE-AC05-06OR23177. The U.S. Government retains a non-exclusive, paid-up, irrevocable, world-wide license to publish or reproduce this manuscript for U.S. Government purposes.

decay ring and decay into neutrinos. The long straight section of the decay ring is aimed at detectors placed in underground facilities several thousand miles away. In this paper, we concentrate on the first stage of acceleration via the RLA.

### A. Recirculated Linear Acceleration

In order to maximize the number of neutrinos produced in the decay one has to accelerate the muons rapidly. This is done first by a superconducting linac which takes the muons from 220 MeV/c to 900 MeV/c. The RLA acceleration follows this first stage. Muons of both species are injected in the middle of a second linac. Achromatic return arcs provide the reinjection into the same linac which is traversed up to 4.5 times for an energy gain of 0.6 MeV/c each time. Upon extraction at the end of the linac, the muons are at 3.6 GeV/c and ready for the next stage.

#### 1. Return Arcs

The initial design for return arcs involved separating the passes and assigning one return arc per pass. The dogbone[8] shaped return arcs are connected to the linacs by means of a switchyard. The drawback of this approach is that it requires one return arc per pass leading to difficulties in designing the switchyard when trying to stack more than two such arcs.

In an attempt to overcome this, an arc design based on a nonlinear nonscaling fixed-field alternating gradient (NS-FFAG) was proposed [9]. While it did permit the transport of two momenta and therefore halved the number of arcs, it also suffered drawbacks. Mainly, the challenge of optimizing the optics with non-linear terms and in particular, the small dynamic aperture.

Next, a linear non-scaling FFAG lattice was studied [10]. While it markedly improved the dynamic aperture and machine sensitivity to errors, it still had a significant footprint requiring many magnets owing to the fact that the basic FFAG cell has alternating in and outbends.

More recently we proposed an alternate design made up of linear combined function magnets. Like the FFAG's it is capable of transporting up to two passes with momentum ratio of up to two. By using only magnets bending in the same direction, we were able to significantly reduce the footprint over a traditional FFAG design [11].

#### 2. Multipass Arcs

Figure 1 depicts the layout of one such multipass arc. It is based upon a unit cell made up of 24 magnets. This cell exhibits mirror symmetry allowing it to be repeated seven times. The first and last cell are outbending cells while the five remaining cells are inbending. Each cell

bends exactly 60 degrees. All magnets are combined function magnets made up of a dipole and a quadrupole field. By adjusting the setpoints for these, one can produce an optic which transports two orbits with momentum ratio of up to two.

In the design shown here, the high momentum orbit has been chosen to go through the center of the magnets while the low momentum is off-center by as much as 16.5 cm. The design is achromatic and also guarantees that the outgoing orbit offset is the same as the incoming orbit. This permits reinjection in the linac for subsequent acceleration.

A few notable points in this design. Firstly, there is no need for a switchyard to connect it to the linac. The first two magnets in the first cell only carry a dipole component allowing the muons to be injected in the arc with enough separation. The same thing is done symmetrically for the last two magnets of the last cell.

Both muon species are accelerated in the linac in the same direction. However, when they come to the arc, they travel in opposite directions owing to the dipole bending opposite charges in opposite directions. The symmetries in the arc guarantee that the muon beams will be reinjected in the linac on axis.

Secondly, out of 24 magnets per cell, only 12 have independent values. This is still more than the minimum number required to satisfy the constraints on the orbit and the dispersion pattern (we want the whole arc to be achromatic). Hence, it is possible to explore alternate designs where the internal five cells need not to be symmetric with the two outbending cells. One can also change the periodicity, allow both orbits to be off-center or provide for long straight sections into which one can add diagnostics or even accelerating cavities.

All these options can be modeled but ultimately one wants to demonstrate their feasibility and build a demonstration machine for this purpose.

## III. SCALED ELECTRON MODEL

### A. Goals

We are proposing to build a small electron machine, Jefferson Lab Electron Model of Muon RLA (JEMM-RLA) to demonstrate the concept of muon RLA acceleration at a smaller scale substituting electrons for muons. This will enable us to find cost efficient designs for the neutrino factory. This also has implications for the larger muon collider which will make use of RLA's in the first stage of acceleration.

### B. Concept

If one substitutes electrons to stand in for the muons, then the energies are scaled proportionally to the ratio of the masses of muon to electron. In addition, one can

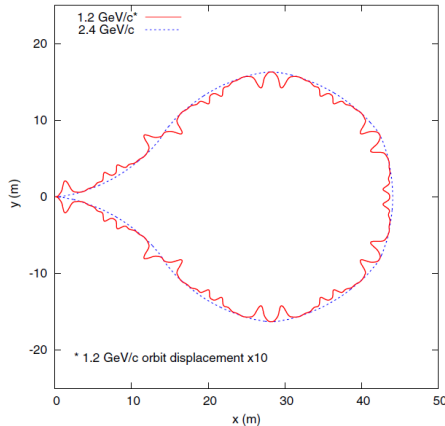


FIG. 1: Geometric layout of the 1.2 and 2.4 GeV/c orbits for the return arc

choose a higher linac frequency (from 200 MHz to 1.5 GHz) to provide a geometric scaling of 7.5. As a result, the linac and two recirculating arcs fit in a 25x7 meters footprint.

A 4.5 MeV electron beam is injected in the middle of the linac and accelerated up to 4.5 times resulting in 18 MeV. The first return arc will provide transport for the 6 MeV and 12 MeV orbits while the opposite arc accommodates the 9 MeV and 15 MeV orbits. The linac is comprised of two cavities, each accelerating 1.5 MeV. Three quadrupoles deliver the mirror symmetric focussing required.

The return arcs are scaled from the muon machine design and have 7 cells each comprised of 24 magnets. The length of each cell is 2.2 meters making it possible to manufacture it as a single curved vacuum chamber.

We studied the feasibility of the concept by prototyping a combined function magnet suitable for this small machine. It is based off the design of an existing FEL magnet and is a modified Panovsky type quadrupole equipped with extra coils to produce the dipole field [12].

It has a 8.6 cm wide x 2.2 cm high aperture, a total length of 6.6 cm and produces a 0.5 T integrated quadrupole field as well as  $4.10^{-3}$  T.m integrated dipole field. Because of its geometry and proximity to other magnets, it is critical to have accurate field maps for optics studies. The RADIA [13] magnet modeling code was utilized to carry out the preliminary studies and generate maps for subsequent tracking. Figures 4 and 5 illustrate this. Once we arrive at a more definitive design for the magnet, full TOSCA[14] simulations will be made to generate the final field maps.

### C. Preliminary Studies

The lattice described in III B was built and simulated using ELEGANT[15]. We demonstrated the existence of the closed orbits as well as the robustness of the lattice under magnet misalignments, mispowering and diagno-

tic errors. Figures 2 and 3 illustrate this. We are planning to further explore alternate lattice as well as optimizing the magnet designs and diagnostic placements in order to minimize the costs.

### D. Costing

A preliminary costing study for the design proposed in section III B was carried out. The powering scheme chosen for the costing employs twelve voltage regulated power supplies of 3kW of capacity each. These will be utilized to drive the quadrupole coils in series. Each power supply drives 14 sets of quadrupole coils. This arises from the symmetries in the system. We have seven identical cells and within a 24 magnets cell, there is mirror symmetry requiring only 12 different values. Therefore, each supply can power 7 (cells) x 2 (identical set-points in a cell) = 14 quadrupoles. Further tuning will be provided by instrumenting some of these quadrupoles with shunts. The dipole coils are powered in series as well requiring 12 more supplies and 7 shunts to individually adjust each dipole pair in each cell.

Vacuum pump needs were estimated by considering one curved vacuum chamber per cell, with rectangular cross-section. Ports will be provided in these chambers to connect primary and ion pumps.

The magnet cost were derived from a similar design for the FEL[12] that has been built and is currently in use. The diagnostics are costed from fully instrumenting each magnet with stripline or button bpms. This includes the cost of electronics but not of the VME crates and inboard computers (IOC) which are listed separately. This rough first estimate puts the cost of this demonstration machine at around \$ 3.3M.

The labor estimates for the design, construction and installation of the machine are around 7 FTE over a period of five years.

It is likely that the construction cost can be reduced by considering alternate designs with less magnets and

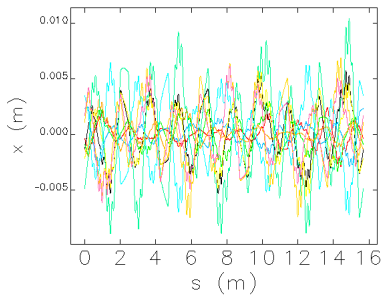


FIG. 2: Closed orbits before correction for perturbed machine

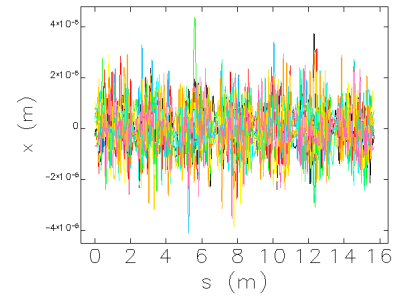


FIG. 3: Closed orbits after correction with SVD steering algorithms

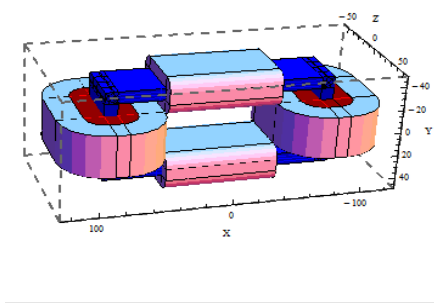


FIG. 4: RADIA model for the combined function magnet showing the quadrupole and dipole inner coils.

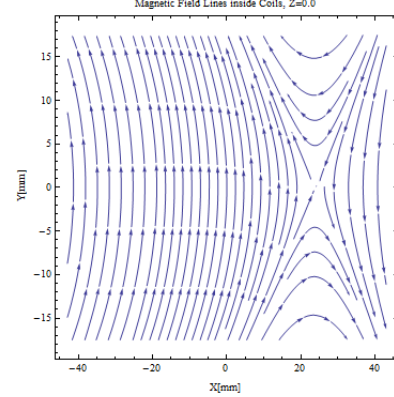


FIG. 5: Calculated Magnetic field at the center of the magnet

optimizing the diagnostic placement.

### E. Conclusion

We have proposed to build a small test machine, JEMMRLA to validate the concept of the first stage of

acceleration of the Muon Factory. We carried out preliminary studies and demonstrated the feasibility of this small electron machine. Cost estimates were made.

- 
- [1] S. Choubey et al. (IDS-NF Collaboration) (2011), 1112.2853.
  - [2] J. R. J. Bennett, L. Bruno, C. J. Densham, P. V. Drumm, T. R. Edgecock, et al. (2004).
  - [3] G. Gregoire, L. Chevalier, M. Catanesi, M. Castellano, P. Fabbricatore, et al. (2003).
  - [4] R. Edgecock, D. Kelliher, S. Machida, et al., in *11th European Particle Accelerator Conference, Genoa, Italy* (2008).
  - [5] S. Bogacz, Nucl.Phys.Proc.Suppl. **155**, 334 (2006).
  - [6] S. Bogacz, G. Wang, and R. Johnson (2009).
  - [7] C. Leemann, D. Douglas, and G. Krafft, Ann.Rev.Nucl.Part.Sci. **51**, 413 (2001).
  - [8] S. Bogacz, Nucl.Phys.Proc.Suppl. **149**, 309 (2005).
  - [9] G. Wang, R. Johnson, S. Bogacz, and D. Trbojevic (2009).
  - [10] V. Morozov, S. Bogacz, and D. Trbojevic, Conf.Proc. **C100523**, 3539 (2010).
  - [11] V. S. Morozov, S. A. Bogacz, Y. R. Roblin, and K. B. Beard, Phys. Rev. ST Accel. Beams **15**, 060101 (2012), URL <http://link.aps.org/doi/10.1103/PhysRevSTAB.15.060101>.
  - [12] G. H. Biallas, N. Belcher, D. Douglas, T. Hiatt, and K. Jordan, Conf.Proc. **C070625**, 602 (2007).
  - [13] J. C. O. Chubar, P. Elleaume, J. Synchrotron Rad **5**, 481 (1998).
  - [14] C. G. Company, Tech. Rep., Cobham Group Company (2005).
  - [15] M. Borland, Tech. Rep. AP-LS287, Argonne National Lab (2000).

# Neutrino-nucleus interactions

U. Mosel and O. Lalakulich

*Institut für Theoretische Physik, Universität Giessen, Germany*

**Abstract.** Interactions of neutrinos with nuclei in the energy ranges relevant for the MiniBooNE, T2K, NO<sub>ν</sub>A, MINERvA and MINOS experiments are discussed. It is stressed that any theoretical treatment must involve all the relevant reaction mechanisms: quasielastic scattering, pion production and DIS. In addition, also many-body interactions play a role. In this talk we show how a misidentification of the reaction mechanism can affect the energy reconstruction. We also discuss how the newly measured pion production cross sections, as reported recently by the MiniBooNE collaboration, can be related to the old cross sections obtained on elementary targets. The MiniBooNE data seem to be compatible only with the old BNL data. Even then crucial features of the nucleon-pion-Delta interaction are missing in the experimental pion kinetic energy spectra. We also discuss the meson production processes at the higher energies of the NO<sub>ν</sub>A, MINERvA and MINOS experiments. Here final state interactions make it impossible to gain knowledge about the elementary reaction amplitudes. Finally, we briefly explore the problems due to inaccuracies in the energy reconstruction that LBL experiments face in their extraction of oscillation parameters.

**Keywords:** Neutrino interactions, Pions, Energy reconstruction

**PACS:** 24.10.Jv,25.30.Pt

## INTRODUCTION

Investigations of neutrino interactions with nucleons can on one hand give valuable information on the axial properties of the nucleon. While the vector couplings of nucleons and their resonances have been explored since many decades in high-precision electron scattering experiments, the axial properties of nucleons are still connected with much larger uncertainties. On the other hand, such experiments also give novel information on neutrino properties, i.e. their masses and mixing angles. For both types of analyses it is mandatory to know the neutrino energy. This is not an easy task since neutrinos are produced as secondary decay products of primarily produced hadrons and thus the neutrino beams are not monoenergetic. This requires a reconstruction of the neutrino energy from final state observations. Such reconstructions have to rely on the assumption of a well-defined reaction mechanism.

The identification of this mechanism becomes difficult when the targets are not nucleons, but nuclei. Apart from the ever-present Fermi-smearing and the action of the Pauli-principle there can be significant final state interactions (FSI) that may hide the special characteristics of the primary interaction vertex. In addition, experiments usually do not observe the full event. An example is given by Cherenkov counter experiments which can only see pions and high-energy protons. Indeed, in the MiniBooNE (MB) experiment all events with 1  $\mu$  and 0 pions were identified as quasielastic-like scattering of a neutrino on a quasifree nucleon and the energy was reconstructed on that basis.

However, the actual reaction mechanism may be significantly more complicated. There can be events in which first a pion was produced which then got stuck in the nucleus due to FSI and thus did not get out to the detector. Such an event contributes to the quasielastic-like event rate [1]. In addition, there can be primary interactions of the neutrino with 2 nucleons (so-called 2p-2h interactions) [2]. All these latter events were identified as QE scattering events by the MB experiment and thus had to be subtracted out from the data by means of event generators.

These event generators have to be reliable for very different reactions types. This is illustrated in Fig. 1 which shows that the MB experiment had to deal with QE scattering and pion production, while deep inelastic scattering (DIS) events contributed very little. The situation has changed when one goes to the MINOS experiment; here, at a mean energy of 5 GeV, quasielastic (QE) scattering, pion production and DIS all contribute approximately with equal size. Any event generator thus has to be able to describe all these different reaction types with an equally good accuracy.

In the following we discuss some aspects of a theoretical treatment of neutrino-induced reactions on nuclei. We start off with a discussion of event-identification and energy reconstruction in connection with QE scattering, then investigate pion production and the special difficulties that appear in the understanding of the present-day experiments MINOS and NO<sub>ν</sub>A. Finally, we give a brief discussion on how our understanding of reaction mechanisms affects the extraction of oscillation parameters.

All results that we are going to discuss are based on

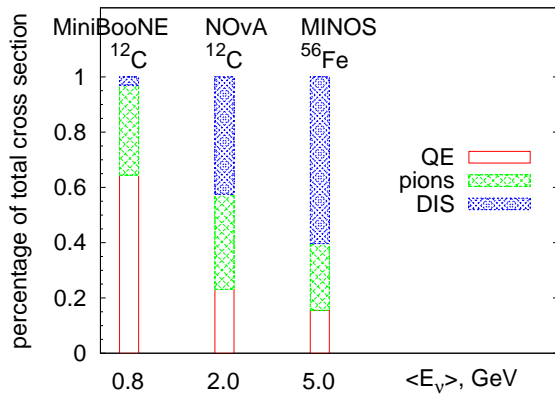


**FIGURE 1.** (Color online) Reaction mechanisms at the 3 experiments presently running at Fermilab. The numbers below each of the vertical bars give the average neutrino energy for that experiment. The contribution labeled 'pions' contains all resonance as well as background contributions.

the GiBUU transport model. GiBUU stands out from all the other neutrino event generators in that it aims to solve the Kadanoff-Baym transport equations [3] in the Botermans-Malfliet approximation [4] for off-shell transport. It has been widely tested on very different classes of nuclear reactions, starting from relativistic heavy-ion collisions to electron and neutrino-induced reactions. For all details of this model, its theoretical foundation and its practical implementation, we refer to a recent review [5]. The results to be discussed in this conference report have recently been published in Refs. [6, 7, 8, 9] where details about the calculations can be found.

## EVENT IDENTIFICATION

Fig. 2 shows both the QE-like and the extracted QE cross sections as obtained in the MB experiment. While the uppermost data points give the actually measured cross section for all events without any pions, dubbed 'QE-like', the lower, extracted points are obtained after subtracting the so-called stuck-pion events, i.e. events in which pions or  $\Delta$ s were first produced, but then got reabsorbed so that they are no longer present in the final state. This subtraction is model dependent, in the case of the MB experiment it has been performed with the NUANCE event generator. The calculated true QE cross section (thick solid line) lies well below even these extracted data. This latter difference has been explained by the presence of 2p-2h excitations [2, 10] that in the MB experiment cannot be distinguished from true QE events, because the nucleons are not observed. It has also been shown that the misidentification of the reaction

mechanism leads to errors in the reconstructed neutrino energy [11, 12, 8].

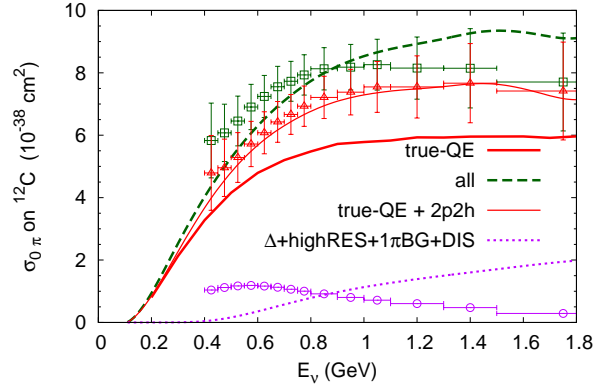


**FIGURE 2.** (Color online) QE-like cross section originating from QE and 2p-2h processes only (solid line) and from all processes (dashed line) within the GiBUU calculations. The thick solid curve gives the true QE cross section. "Measured" (squares) and "extracted" (triangles) MiniBooNE data points are taken from [13]. The difference between them (open circles) is to be compared with the GiBUU 'stuck pion' cross section (dotted line). All data are plotted vs reconstructed energy, whereas the theoretical curves are plotted vs true neutrino energy.

Since the extracted QE data contain a generator dependence due to the background subtraction of stuck-pion events, any analysis of the actual data must involve both QE, pion production and pion absorption. While Ref. [12] contained a sophisticated treatment of QE only, the work of Ref. [11] did treat pion production in addition, however, without any pion FSI. We have, therefore, performed in [8] a complete study of all three necessary ingredients. That this is necessary can be seen by going back to Fig. 2 which exhibits an astonishing behavior already in the QE-like data. The QE-like and the extracted QE cross sections show most of their difference at the lowest energies whereas they become much closer at the highest energies; this difference is shown by the open circles. As discussed above, this difference should be due to stuck-pion events and the pion production probability steeply increases with beam energy. Thus, the opposite behavior was to be expected. In [8] we have shown that this unexpected behavior is caused by errors made in the energy reconstruction due to the misidentification of the reaction process. Fig. 3 shows that for true QE events the reconstruction procedure works very well, but for all other reactions it leads to a lower reconstructed energy than the true energy. At the same time the functional shape of the stuck-pion cross sections as a function of reconstructed energy is quite different from that of that same cross section as a function of true energy. This is illustrated by the dotted line in Fig. 2 which gives the cross section for stuck-pion events as a function of true energy;

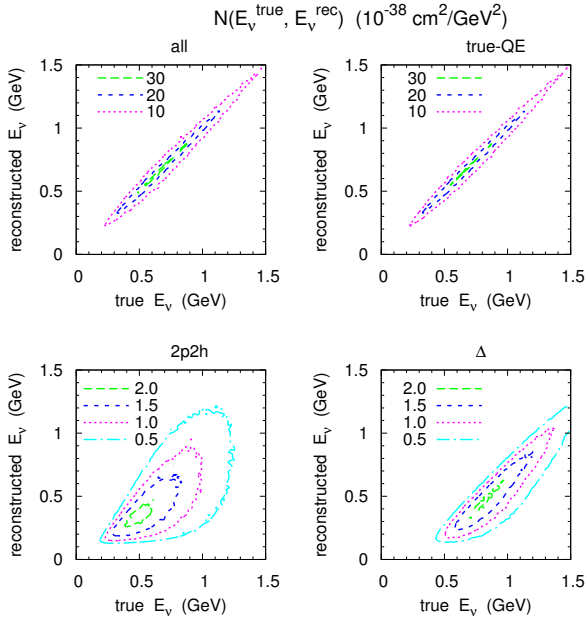


**FIGURE 3.** (Color online) 2-D density of the QE-like cross section  $N(E^{\text{true}}, E^{\text{rec}})$  (the so-called migration matrix) versus true and reconstructed neutrino energies for all events and for events of various origins, all for the MB flux. Figure taken from [8].

it indeed increases with energy as it should whereas the same quantity as a function of reconstructed energy starts up high and then decreases as a function of energy (open circle symbols); for a more detailed discussion see [8].

In view of these rather large uncertainties in the extraction of physical properties one is tempted to look for better strategies to identify a certain reaction type. In particular, for the case of QE scattering it is worthwhile to remember that tracking detectors are much better suited to correctly identify a reaction mechanism because they rely not only on the absence of a pion, but also on the presence of one outgoing nucleon. This is illustrated in Figs. 4,5. The figures shows nicely that Cherenkov detectors always measure a too-high cross section, because other event types cannot be distinguished from true QE. Tracking detectors miss part of the total cross section because they will not see events in which the initial proton kicks out a second proton or undergoes charge exchange into a neutron. However, tracking detectors allow a much cleaner event identification than Cherenkov counters: nearly all the events ascribed to QE scattering are indeed from that source.

This is found to be true also when there are 2p-2h processes in the first, primary interaction of the neutrino with the nucleus. The naive expectation that then the knock-out of 2 particles is favored [14] is overshadowed by the strong FSI effects on the outgoing nucleons. These

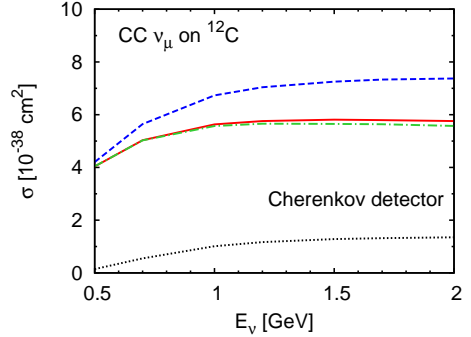


**FIGURE 4.** (Color online) Total QE cross section on  $^{12}\text{C}$  (solid lines) compared to the method used to identify CCQE-like events in experiments (dashed line). The figure shows the method commonly applied in Cherenkov detectors. The contributions to the CCQE-like events are also classified [CCQE-like from initial QE (dash-dotted) and from initial  $\Delta$  (dotted lines)]. Figure taken from [1].

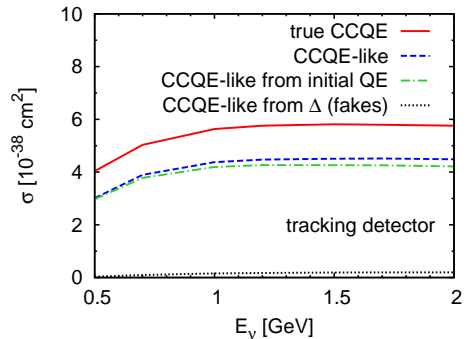


**FIGURE 5.** Same as Fig. 4, but for Tracking Detector

FSI lead to a sort of ‘avalanching’ so that the energy of a single nucleon is quickly distributed over many of them. Thus the multiplicity of the outgoing nucleons is only a rather weak indicator of the primary process. This can be seen in the results shown in Fig. 6. The two-nucleon knock-out contains nearly equal contributions from true QE and initial 2p-2h processes so that the identification of either one will be very difficult, if not impossible. However, the same figure also shows that the one-and-only-one nucleon knock-out channel is – apart from  $\Delta$  contributions – dominated by true QE.

This channel could thus be used to identify true QE scattering if the  $\Delta$  contribution can be controlled.

## PION PRODUCTION AROUND 1 GEV

The difference between the measured QE-like and the extracted QE cross sections determined by MB is due to

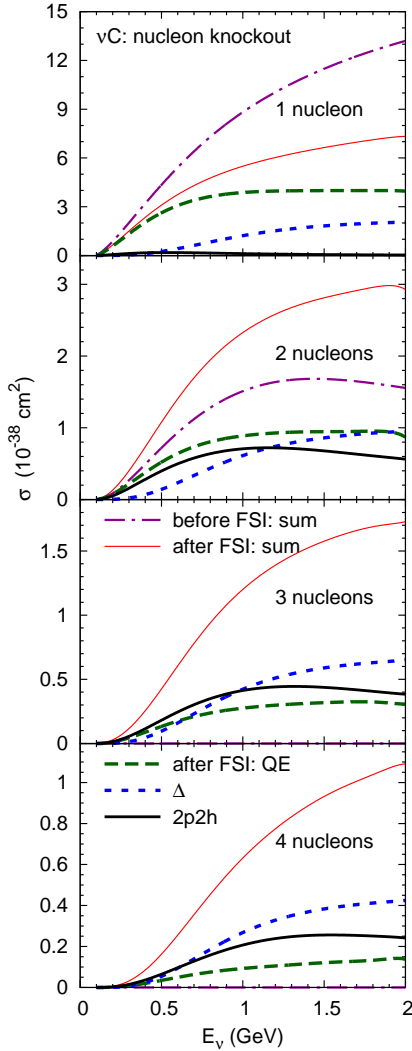


**FIGURE 6.** (color online) Cross-section for multi-nucleon knock-out as a function of neutrino energy. In each case the total cross section is given by the thin solid line. The QE contribution is indicated by the long-dashed line. The short dashed line shows the  $\Delta$  contribution, while the 2p-2h contribution is indicated by the thick solid line. All these lines show the results after FSI, while the dot-dashed curves shows the total cross section before FSI. Figure taken from [6].

stuck-pion events. There is then obviously a close connection between this difference and the pion production cross sections also measured by MiniBooNE [15, 16]. Until recently, the only comparisons of theoretical calculations with these data were those in Refs. [17] that both showed a significant underestimate of the experimental data and a significantly different spectral shape of the produced pions. These calculations used the old ANL data as input and the full MiniBooNE flux for both charge states of the pion.

We have recently extended these studies by using both the ANL and the BNL data [19, 18] as an input to the calculations [9]. Since the BNL data are consistently higher than the ANL data (see Figs. 7,8) we obtain a band of predictions for the pion production cross section. In addition, the calculations for  $\pi^0$  production were now redone with the same cut on the neutrino energy  $0.5 \text{ GeV} < E_\nu < 2.0 \text{ GeV}$  as that used in the experimental analysis.

The results of these calculations are shown in Fig. 9. The difference between the two dashed curves (before FSI) and the two solid curves (after FSI) gives a band of uncertainty due to the uncertainty in the elementary input. While the results before FSI follow the data fairly well, the results after FSI underestimate it significantly and contain a structure in the momentum distribution that is not there in the data. This is surprising since this structure is due to pion absorption through the  $\Delta$  resonance and has been experimentally observed in photoproduc-

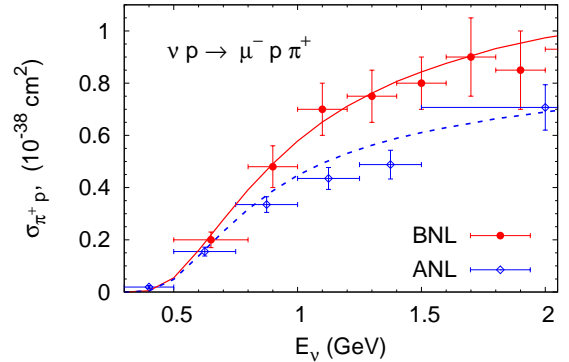


**FIGURE 7.** (Color online) Single-pion production cross section on a proton target obtained in the BNL [18] (circles; solid curve) and the ANL experiments [19] (diamonds; dashed curve) for  $1\pi^+$  production. The curves give the lower (ANL-tuned) and upper (BNL-tuned) boundaries on the elementary input as used in GiBUU.

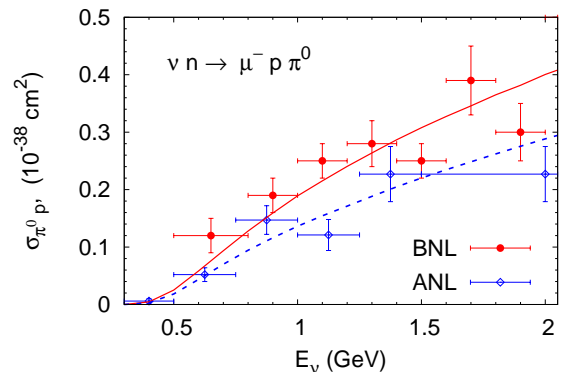


**FIGURE 8.** Same as Fig. 7 for  $1\pi^0$  production.

tion of  $\pi^0$  mesons on nuclei [20].

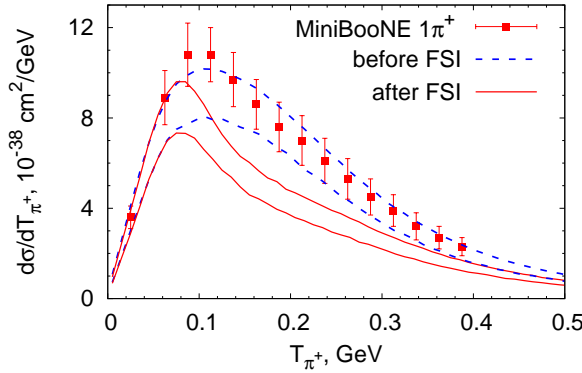


**FIGURE 9.** Kinetic energy distribution of the outgoing  $\pi^+$  for single-pion production at MiniBooNE. Data are from [15]. The upper and lower dashed curves give the results before FSI using the BNL and the ANL elementary cross sections, resp. The solid lines give the corresponding results after FSI. Figure taken from [9].

The MiniBooNE experiment had determined its neutrino flux by using hadronic production cross sections. The analysis of QE scattering by Nieves et al. [10] has shown that a good description of the MB QE data can be reached when the actual flux is assumed to be 10% higher than determined by the MB experiment; such a renormalization is still within the uncertainties of the flux determination by MB. Applying the same correction to the pion data brings them into better overall agreement with our theoretical results [8]. However, even then there is still an indication of the difference in shape of the experimental and theoretical distributions. This has to be clarified through a new look at the data. The special shape of the distribution obtained in the calculations is a conse-

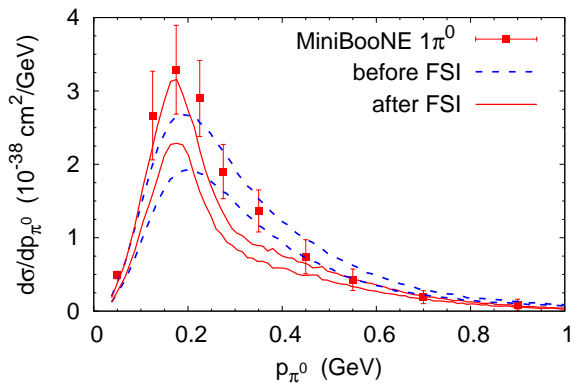


**FIGURE 10.** Same as Fig. 9, but for the momentum distribution of the outgoing  $\pi^0$ . Data are from [16]. Figure taken from [9].

quence of FSI and these final state interactions should be the same as in photoproduction of pions. Upcoming new data from electroproduction at JLAB could also be most useful to clarify this question.

## INTERACTIONS IN THE SIS REGIME

The long baseline experiments MINOS and NOvA at Fermilab both work at a higher neutrino energy than MiniBooNE. While NOvA uses a relatively sharp flux peaking at about 2 GeV, MINOS works with a broader distribution of incoming neutrino energies with a peak around 3 GeV and an average around 5 GeV. Fig. 1 illustrates that while NOvA has about equal parts of QE scattering, pion production and DIS the MINOS experiment is clearly dominated by DIS, however there is still a significant amount of pion production and a small contribution of QE scattering. Both experiments work in the transition area between resonance dominated physics and DIS that is located above a baryon mass of about 2 GeV. While concepts of perturbative QCD work very well in the asymptotic (Bjorken) limit [21], this so-called shallow-inelastic scattering (SIS) is a much more complicated regime. Here, for example, 2-meson channels, for which usually there are only very few data available, may become important. This problem of missing elementary input then affects all predictions for neutrino-nucleus interactions in this region.

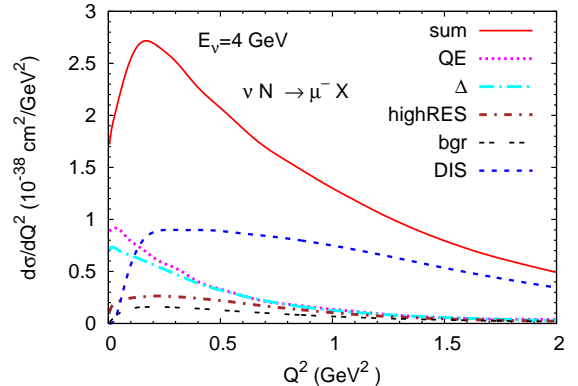


**FIGURE 11.** (Color online) Cross section  $d\sigma/dQ^2$  per nucleon for CC neutrino scattering off an isoscalar target for  $E_\nu = 4$  GeV.

Fig. 11 shows the  $Q^2$  dependence of the various contributions to the cross section for an incoming energy of 4 GeV. One sees that even at this higher energy the  $\Delta$  and QE scattering contribute to the cross section, but they are dominant only at small  $Q^2 < 0.4$  GeV $^2$ . For larger  $Q^2$  DIS clearly dominates. This different behavior may offer a possibility to distinguish between the other reac-

tion mechanisms and DIS if the  $Q^2$  reconstruction can be done reliably.

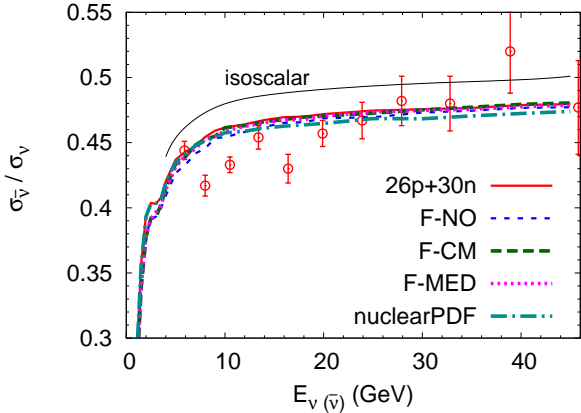


**FIGURE 12.** (Color online) Ratio of the antineutrino to neutrino cross sections in scattering off iron. Also shown is the calculated ratio for an isoscalar target. Experimental data are taken from [22] (MINOS, open circles). Figure taken from [7].

At high energies, in the asymptotic QCD regime, the ratio of antineutrino to neutrino cross sections approach the constant value  $\approx 0.5$  at energies above about 25 GeV [21]. Theory and data show that this is not the case in the SIS region. Fig. 12 shows that this ratio increases steeply as a function of neutrino energy for energies below about 10 GeV. This steep rise is due to the fact that for an antineutrino both the QE and the  $\Delta$  resonance excitation cross sections are significantly lower than for a neutrino, leading to a small ratio. With increasing neutrino energy these components die out and DIS takes over a dominating role. For DIS the ratio then is given (for an isoscalar target) by the asymptotic value of about 0.5. The various curves in the figure illustrate different treatments of in-medium effects; that they all agree with each other shows that this ratio is fairly independent of nuclear effects.

In Ref. [7] we have given detailed predictions for spectra of knock-out nucleons and produced mesons for both the MINOS and the NOvA fluxes. Here, as an example, we just show the distributions for pions and for kaons in Figs. 13 and 14, resp., for the MINOS flux.

The pion spectra resemble those discussed earlier for the MB flux. They all exhibit the suppression around 0.2 GeV due to pion FSI. This just shows that even though these pions have originally been produced by quite a different mechanism as compared to the situation at MB (DIS vs.  $\Delta$  resonance) the final state interactions for pions are so strong that they essentially wipe out any memory of the production process. In this situation the observable spectra are determined only by the FSI. As discussed in [7] very few of the pions finally observed are actually the same as those produced in the primary reaction process. Instead, pion absorption and reemission

takes place and helps again to shadow the elementary production process.

This is even more so for kaons. While there are new calculations of neutrino-induced exclusive kaon production cross sections on the nucleon [23] these elementary processes will be very hard – if not impossible – to observe. Since the neutrino flux always involves broad distributions with tails towards higher energies the observed kaon production rate is always dominated by DIS followed by strong secondary interactions. This is again discussed in some detail in [7]. Here we just show the spectra in Fig. 14. All these spectra show a pile-up at low kinetic energies due to multiple FSI. Note that the results shown here are for  $K^+$  and  $K^0$ . For both, because of strangeness conservation, the absorption on a nucleon in the nuclear target is very small, but they can easily undergo charge transfer processes  $K^+n \rightarrow K^0p$  or inelastic reactions such as  $K^+N \rightarrow K^+\Delta$  which leads to a loss of kaon energy and simultaneous pion production.

## EXTRACTION OF OSCILLATION PARAMETERS

After having observed this rather significant influence of the energy reconstruction on the observed cross sections the question immediately arises how this affects the extraction of neutrino oscillation properties. This is indicated in Fig. 15 which shows the calculated event rate for electron appearance in the T2K experiment which uses QE-like events as signal. Again, it can be seen that the event rate as a function of reconstructed energy has more strength at lower energies and less in the peak region than that as a function of true energy. How this extra strength affects the actual oscillation parameters has not been explored yet, but there are first attempts by D. Meloni et al. [24] to investigate this question. Here it is sufficient to note that the difference between the true-energy and the reconstructed-energy results is similar to that expected from varying the phase  $\delta_{CP}$  that controls the possible  $CP$  violation in electroweak interactions (see Fig. 16). Any experiment aiming for a determination of  $\delta_{CP}$  with neutrinos alone would thus have a hard time to achieve the necessary sensitivity to that phase.

## SUMMARY

Neutrino-nucleus interactions in the energy range of the MiniBooNE, T2K, NOvA, MINERvA and MINOS experiments are sensitive to various elementary interactions. QE scattering, two-body interactions connected with meson exchange currents, pion production through nucleon resonances (including background) and deep in-

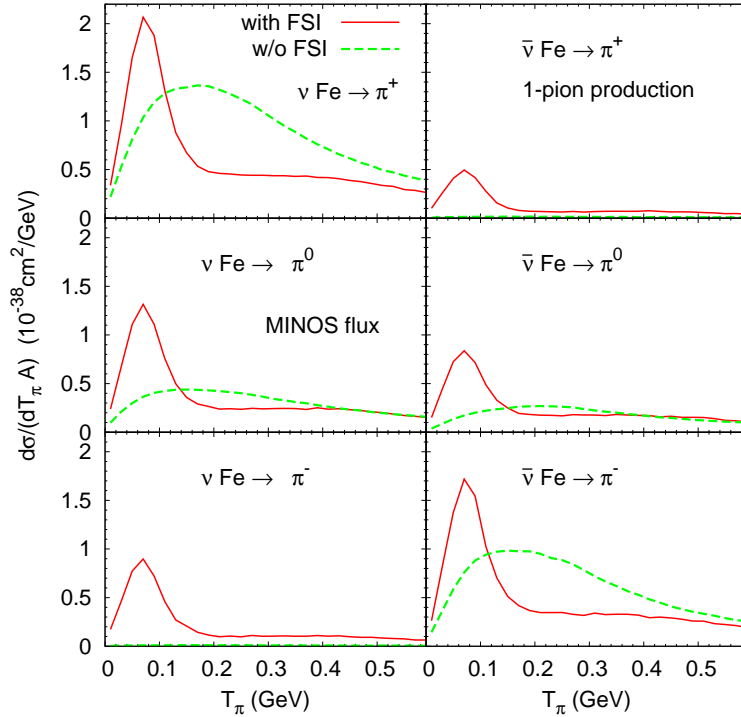


**FIGURE 13.** (Color online) Pion kinetic energy distributions per target nucleon for neutrino and antineutrino scattering off iron for single-pion production (one pion of the indicated charge and no other pions are produced). Figure taken from [7].

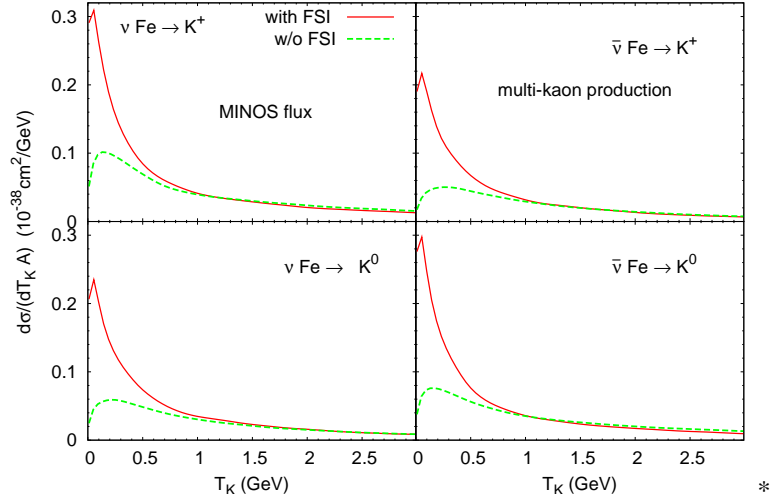


**FIGURE 14.** (Color online) Kinetic energy distributions per target nucleon for multi-kaon (at least one kaon of a given charge and any other hadrons) production in neutrino and antineutrino scattering off iron. Figure taken from [7].

elastic scattering all play a role. A theoretical treatment thus has to be able to deal with all of them with equal accuracy. This is so important because neutrino experiments in the past tended to subtract some of these processes as background from their data. The remaining 'data' were then already influenced by possible shortcomings of the generators.

We are now in a position to deal with the actual data, e.g. directly the QE-like cross sections measured by MiniBooNE, and not just the extracted 'data'. For the MiniBooNE this requires primarily a good treatment of QE scattering *and* pion production, both from resonances, background and (to a minor extent) from DIS. In this talk we have discussed the theoretical results and

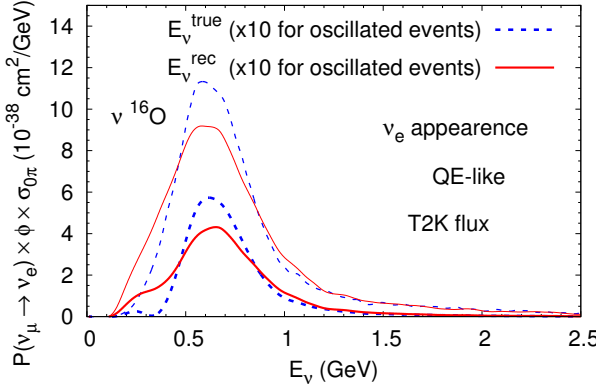


**FIGURE 15.** (Color online) The event rate, i.e. flux times cross section, for electron neutrino appearance measurements. The oscillated event curves have been multiplied by a factor of 10 to enhance the visibility of their difference. Figure taken from [8].

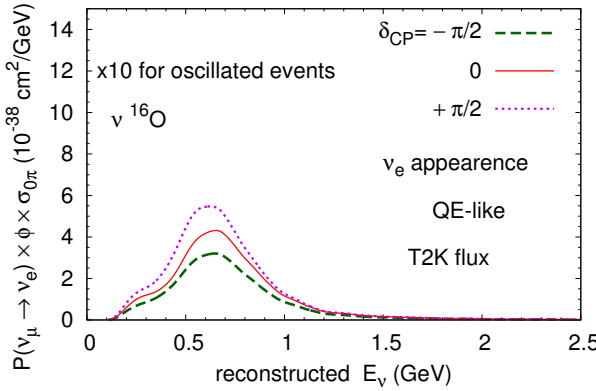


**FIGURE 16.** (Color online) Same as Fig. 15 for various CP violation phases. Figure taken from [8].

compared them with the MB pion data. A significant sensitivity to the elementary input is found. If many-body contributions to pion production are not large then only the old BNL elementary pion production data seem to be compatible with the MB data. An ultimate clarification of this question can, however, come only from new data for neutrino interactions with single nucleons.

At the higher energies so-called shallow inelastic processes, for which very few elementary data are known, complicate the picture. QE-scattering and resonance excitations still contribute even at a few GeV neutrino energy to the total cross section. However, these events are localized at lower momentum transfers whereas at the higher  $Q^2$  DIS takes over. Particle production in this energy regime is sensitive not only to these primary production processes, but also to strong FSI. This is true

not only for the strongly interacting pions, but also for positively charged and neutral kaons which are (erroneously) often believed to suffer very few FSI because of strangeness conservation. As a consequence, one has to conclude that any measurements of pions or kaons in the MINERvA or NOvA experiments do not yield information on the elementary cross section.

Finally we have illustrated how shortcomings in the identification of QE scattering and the energy reconstruction that is built on it can affect the oscillation parameters. These uncertainties clearly affect the extraction of the  $CP$ -violating phase.

This work was supported by DFG and by BMBF.

## REFERENCES

1. T. Leitner, and U. Mosel, *Phys.Rev.C* **81**, 064614 (2010).
2. M. Martini, M. Ericson, G. Chanfray, and J. Marteau, *Phys.Rev.C* **80**, 065501 (2009).
3. L. Kadanoff, and G. Baym, *Quantum statistical mechanics*, Benjamin, New York, 1962.
4. W. Botermans, and R. Malfliet, *Phys.Rept.* **198**, 115–194 (1990).
5. O. Buss, T. Gaitanos, K. Gallmeister, H. van Hees, M. Kaskulov, et al., *Phys.Rept.* **512**, 1–124 (2012).
6. O. Lalakulich, K. Gallmeister, and U. Mosel, *Phys.Rev.C* **86**, 014614 (2012).
7. O. Lalakulich, K. Gallmeister, and U. Mosel, *Phys.Rev.C* **86**, 014607 (2012).
8. O. Lalakulich, and U. Mosel (2012), nucl-th/1208.3678.
9. O. Lalakulich, and U. Mosel (2012), nucl-th/1210.4717.
10. J. Nieves, I. Simo, and M. Vacas, *Phys.Lett.* **B707**, 72–75 (2012).
11. M. Martini, M. Ericson, and G. Chanfray, *Phys.Rev.* **D85**, 093012 (2012).
12. J. Nieves, F. Sanchez, I. Ruiz Simo, and M. Vicente Vacas, *Phys.Rev.* **D85**, 113008 (2012).
13. A. Aguilar-Arevalo, et al., *Phys.Rev.D* **82**, 092005 (2010).
14. J. T. Sobczyk, *Phys.Rev.* **C86**, 015504 (2012).
15. A. Aguilar-Arevalo, et al., *Phys.Rev.D* **83**, 052007 (2011).
16. A. Aguilar-Arevalo, et al., *Phys.Rev.D* **83**, 052009 (2011).
17. O. Lalakulich, K. Gallmeister, T. Leitner, and U. Mosel, *AIP Conf.Proc.* **1405**, 127–133 (2011), 1107.5947.
18. T. Kitagaki, et al., *Phys. Rev.* **D34**, 2554–2565 (1986).
19. G. M. Radecky, et al., *Phys. Rev.* **D25**, 1161–1173 (1982).
20. B. Krusche, J. Lehr, J. Ahrens, J. Annand, R. Beck, et al., *Eur.Phys.J.* **A22**, 277–291 (2004).
21. J. M. Conrad, M. H. Shaevitz, and T. Bolton, *Rev. Mod. Phys.* **70**, 1341–1392 (1998).
22. P. Adamson, et al., *Phys. Rev.* **D81**, 072002 (2010).
23. M. Rafi Alam, I. Ruiz Simo, M. Sajjad Athar, and M. Vicente Vacas, *Phys.Rev.* **D82**, 033001 (2010).
24. D. Meloni, and M. Martini, *Phys.Lett.* **B716**, 186–192 (2012).

# Improved Measurement of Electron Antineutrino Disappearance at Daya Bay

Xin Qian<sup>1</sup>, on behalf of the Daya Bay Collaboration

*Kellogg Radiation Laboratory, California Institute of Technology, Pasadena, CA*

**Abstract.** The Daya Bay experiment was designed to be the largest and the deepest underground among the many current-generation reactor antineutrino experiments. With functionally identical detectors deployed at multiple baselines, the experiment aims to achieve the most precise measurement of  $\sin^2 2\theta_{13}$ . The antineutrino rates measured in the two near experimental halls are used to predict the rate at the far experimental hall (average distance of 1648 m from the reactors), assuming there is no neutrino oscillation. The ratio of the measured over the predicted far-hall antineutrino rate is then used to constrain the  $\sin^2 2\theta_{13}$ . The relative systematic uncertainty on this ratio is expected to be 0.2~0.4%. In this talk, we present an improved measurement of the electron antineutrino disappearance at Daya Bay. With data of 139 days, the deficit of the antineutrino rate in the far experimental hall was measured to be  $0.056 \pm 0.007$  (stat.)  $\pm 0.003$  (sys.). In the standard three-neutrino framework, the  $\sin^2 2\theta_{13}$  was determined to be  $0.089 \pm 0.011$  at the 68% confidence level in a rate-only analysis.

**Keywords:** neutrino oscillation, neutrino mixing, reactor, Daya Bay

**PACS:** 14.60.Pq

## INTRODUCTION

As fundamental particles in the standard model, (anti)neutrinos were initially thought to have zero mass. Such an assumption was supported by the experimental evidence that only left-handed neutrinos (also right-handed antineutrinos) were detected [1]. However, in the past decades, the phenomenon of neutrino flavor oscillation observed by Super-K, SNO, KamLAND, MINOS, and many other experiments successfully established the existence of non-zero neutrino masses and the neutrino mixing. A recent review can be found in Ref. [2]. The neutrino oscillations are commonly described by the Pontecorvo-Maki-Nakagawa-Sakata (PMNS) matrix and two neutrino mass-squared differences ( $\Delta m_{32}^2 := m_3^2 - m_2^2$  and  $\Delta m_{21}^2 := m_2^2 - m_1^2$ ) [3, 4, 5]. The PMNS matrix denotes the mixing between the neutrino flavor and mass eigenstates. It contains three mixing angles  $\theta_{12}$ ,  $\theta_{23}$ , and  $\theta_{13}$ , and an imaginary phase  $\delta$ , referred to as the CP phase in the leptonic sector.

As of two years ago,  $\theta_{13}$  was still the least known among all three neutrino mixing angles in the PMNS matrix. The best constraint was from CHOOZ reactor antineutrino experiment with  $\sin^2 2\theta_{13} < 0.17$  at 90% confidence level (C.L.) [6, 7]. A global analysis [8] in 2008 including both solar and reactor neutrino data suggested a non-zero  $\theta_{13}$ . However, in the past 18 months or so, an explosion of data from multiple experiments greatly enhanced our understanding of  $\theta_{13}$ . In 2011, through mea-

surements of  $\nu_e$  appearance from a  $\nu_\mu$  beam, the long baseline experiments T2K [9] and MINOS [10] reported hints of a non-zero  $\theta_{13}$  at about 2.5 and 1.4 standard deviations<sup>2</sup>, respectively. In January 2012, the reactor antineutrino experiment Double-CHOOZ [11] also reported a hint of a non-zero  $\theta_{13}$  at 1.6 standard deviations with a single detector. The Daya Bay experiment, with six functionally identical detectors at three locations, carried out a measurement of relative ratio of reactor antineutrino rates [12], which significantly improved the sensitivity to the  $\sin^2 2\theta_{13}$ . In March 2012, the Daya Bay collaboration announced a non-zero value of  $\theta_{13}$  at 5.2 standard deviations [13]. About one month later, this finding was confirmed by the RENO reactor antineutrino experiment [14], which reported a consistent result using a ratio between antineutrino rates from two detectors. The Daya Bay experiment has since reported an improved measurement of the electron antineutrino disappearance [15] with 2.5 times of the previously reported statistics [13].

## THE DAYA BAY EXPERIMENT

The Daya Bay experiment, located on the south coast of China (55 km northeast to Hong Kong and 45 km east to Shenzhen), was designed to provide the most precise measurement of  $\theta_{13}$  with a sensitivity of  $\sin^2 2\theta_{13} < 0.01$

---

<sup>1</sup> Email:xqian@caltech.edu

<sup>2</sup> Results from the long baseline experiments actually depend on the assumption of the neutrino mass hierarchy and value of CP phase  $\delta$ .

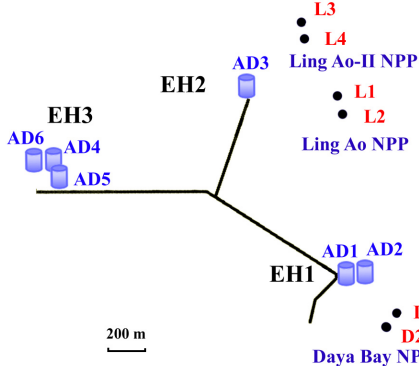


**FIGURE 1.** The layout of the Daya Bay experiment. The dots represent reactor cores, labeled as D1, D2, and L1-4. Six ADs were installed in three experimental halls during the reported analysis period.

at a 90% C.L. [16]. Such a measurement requires high accuracy and precision. The high accuracy is achieved by the combination of powerful reactors (17.6 GW thermal power) and large target mass (80 tons in the far hall). In addition, the location of the far detectors is optimized to obtain the best sensitivity to  $\sin^2 2\theta_{13}$  with the current knowledge of  $\Delta m_{32}^2$ . To achieve high precision, the reactor-related systematic uncertainties are minimized by adapting the ratio method [12] with multiple detectors at multiple baselines. The detector-related systematic uncertainties are minimized by using identical detectors and performing precise detector calibrations. The background-related systematic uncertainties are minimized by placing detectors deep underground in order to reduce cosmic muon related backgrounds. Furthermore, passive shielding (water pools surrounding detectors) and active shielding (resistive-plate chambers above water pools) were implemented to tag the cosmic muons. The water pools also shield detectors from various environmental radioactive backgrounds.

Fig. 1 shows the layout of the Daya Bay experiment during this reported analysis period. There are six reactors grouped into three pairs. Each reactor contains a core with a maximum 2.9 GW thermal power. Three underground experimental halls (EHs) are connected with horizontal tunnels. The effective vertical overburdens are 250, 265, and 860 water-equivalent meters for EH1, EH2, and EH3, respectively. For this improved measurement, two, one, and three antineutrino detectors (ADs) were installed in EH1, EH2, and EH3, respectively. The distance from the six ADs to the six cores were surveyed with the Global Positioning System (GPS) above ground and Total Stations underground. The precision of distance was about 1.8 cm.

The antineutrinos in the Daya Bay experiment are detected through the inverse beta decay (IBD) process

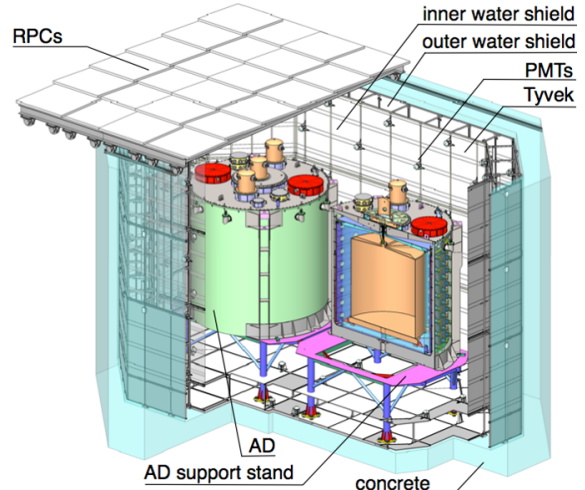


**FIGURE 2.** Layout of Daya Bay detectors in a near site.

$\bar{\nu}_e + p \rightarrow e^+ + n$ . The signature of such process is a prompt signal of the scintillation and subsequent annihilation of the positron in the liquid scintillator (LS), followed shortly by a delayed signal with  $\sim 8$  MeV energy deposition when the neutron is captured by the Gadolinium (Gd) doped inside LS (0.1% in weight). The energy of neutrino can be deduced from the energy deposition of the prompt signal with  $E_{\bar{\nu}} \approx E_{\text{positron}} + 0.8$  MeV. As shown in Fig. 2, the ADs adopt a three-zone cylindrical-shaped design, with the inner, middle, and outer zone containing 20 ton Gd-doped LS (Gd-LS), 20 ton LS, and 40 ton mineral oil, respectively. With load cells and an ISO tank, the target mass uncertainty of the 20 ton GD-LS is controlled to be only about 3 kg.

Each AD contains 192 8-inch photomultiplier tubes (PMTs) installed on the side walls. The photocathode coverage is about 8%, which is further enhanced to about 12% with a pair of optical reflectors at the top and bottom of each detector. The achieved detector energy resolution is parametrized as [17]

$$\frac{\delta E}{E} = \left( \frac{7.5}{\sqrt{E(\text{MeV})}} + 0.9 \right) \%, \quad (1)$$

with respect to the visible energy  $E$ . The detector calibration is performed weekly with three automated calibration units (ACUs) per AD: two located above the center and the edge of the GD-LS region and one placed above the LS region. The ACUs are remotely controlled by a LabVIEW program and operated underwater. Each ACU contains four sources: a light-emitting diode (LED) for the PMT gain/timing calibration, a  $\sim 15$  Hz  $^{68}\text{Ge}$  source for the threshold calibration of the IBD prompt signal, a  $\sim 100$  Hz  $^{60}\text{Co}$  source for the high statistical determination of the overall energy scale, and a  $\sim 0.5$  Hz  $^{241}\text{Am}$

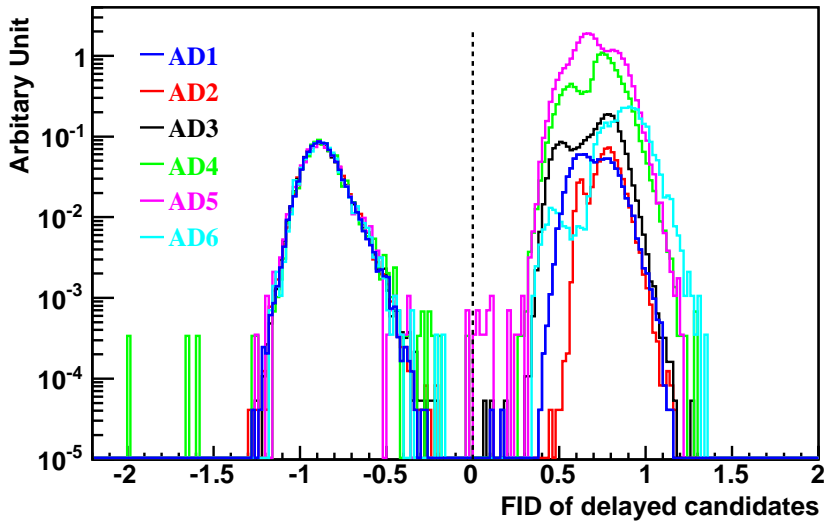


**FIGURE 3.** Discrimination of the flasher events ( $\text{FID} > 0$ ) from the delayed signals of IBD ( $\text{FID} < 0$ ). While the flasher events possess different distributions among different ADs, the delayed signals of IBD share the same distribution.

$^{13}\text{C}$  neutron source to understand neutron captures on Gd and to determine the H/Gd ratio in the target region.

The muon detection system in each experimental hall consists of a high purity water pool surrounding the ADs and a layer of resistive plate chambers (RPC) above the water pool. The water pool is further divided into two optically separated regions, the inner water pool (IWS) and the outer water pool (OWS). Each region operates as an independent water Cerenkov detector, and can be used to cross calibrate each other. The muon detection efficiencies are measured to be 99.7% and 97% for the IWS and OWS [17], respectively. The water pool also plays a crucial role in shielding radioactive backgrounds. The distance between the edge of each AD to the closest wall is at least 2.5 m. The array of RPCs covering the entire water pool is used to provide additional tagging of cosmic muons.

## SELECTION OF INVERSE BETA DECAY EVENTS

About 5% of the PMTs would spontaneously flash and emit light. Such events are called “flashers”. The reconstructed energy of such events covers a wide range, from sub-MeV to 100 MeV. A few features are observed when a PMT flashes: i) the charge fraction of the flashing PMT is high; ii) the surrounding PMTs as well as the ones located on the opposite side of the AD receive large fraction of light from the flashing PMT; and iii) the timing spread of all PMTs’ hits are generally wide. Accordingly, a few flasher identification (FID) variables were

constructed to separate the good physics events from the flashing events. Fig. 3 shows the distribution of an FID variable deduced from the charge pattern for the IBD delay candidates. The good IBD events are well separated from the flasher events. Detailed description of the flasher discrimination can be found in Ref. [17]. The inefficiency of the IBD signals due to FID cuts is only about  $(0.024 \pm 0.006)\%$ , and the contamination of flashing events in the IBD sample is below 0.01%, which is further suppressed by the accidental background subtraction procedure.

After the flashing events are removed, the IBDs are further selected with the following cuts: i) the energy of the prompt signal is between 0.7 and 12 MeV; ii) the energy of the delay signal is between 6 and 12 MeV; and iii) the time difference between the prompt and the delay signal is between 1 and 200  $\mu\text{s}$ . In addition, a multiplicity cut is applied to remove the energy ambiguities in the prompt signal. For example, one choice of the multiplicity cut requires no prompt-like signal 400  $\mu\text{s}$  before the delay signal and no delay-like signal 200  $\mu\text{s}$  after the delay signal<sup>3</sup>. The fixed time cut (relative to the delay signal) leads to simplified calculations of the efficiency and livetime of IBD events and the rate of accidental backgrounds. Correspondingly, three types of muon veto cuts are also applied to the delay signal in order to suppress backgrounds. The first one is for the water pool muon, which is defined as one IWS or OWS event with more

<sup>3</sup> The prompt-like and delay-like signals refer to events with energy 0.7-12 MeV and 6-12 MeV, respectively.

than 12 PMT hits. The veto cut spans from  $2 \mu\text{s}$  before to  $600 \mu\text{s}$  after the water pool signal. The second one is for the AD shower muon, which is defined as one AD signal with more than  $3 \times 10^5$  photoelectrons (PEs). The corresponding energy is about 1.8 GeV. The veto cut spans from  $2 \mu\text{s}$  before to  $0.4 \text{ s}$  after the AD signal. The last one is for the AD non-shower muon, which is defined as one AD signal with its energy between 20 MeV and 1.8 GeV. The veto cut spans from  $2 \mu\text{s}$  before to  $1.4 \text{ ms}$  after the AD signal. The choice of  $2 \mu\text{s}$  before the muon signal in all three cuts is to leave enough room for the potential non-synchronization among different detectors. The AD shower muon veto is applied to suppress the long-lived  $^9\text{Li}/^8\text{He}$  background. The AD non-shower muon veto is applied to suppress the fast neutron background. The overall detection efficiency for the IBD events is about 80%, with the Gd capture ratio (84%) and the efficiency of the 6 MeV delay signal cut (91%) being the two leading contributors.

## SUMMARY OF BACKGROUNDS

The largest contamination in the Daya Bay IBD sample is the accidental background with about 4.6% at the far site and about 1.7% at the near sites. An accidental background event arises when a delay-like signal and an unrelated prompt-like signal (usually radioactive events) accidentally fall within a  $199 \mu\text{s}$  coincidence window. Such background ( $R_{\text{accidental}}$ ) can be accurately calculated through Poisson statistics given the measured rates of single prompt-like events ( $R_p$ ) and single delay-like events ( $R_d$ )<sup>4</sup>:

$$R_{\text{accidental}} = P(0, 200\mu\text{s} \cdot R_p) \cdot P(1, 199\mu\text{s} \cdot R_p) \cdot R_d \cdot P(0, 200\mu\text{s} \cdot R_d). \quad (2)$$

Poisson function  $P(n, \mu) = e^{-\mu} \frac{\mu^n}{n!}$  represents the probability of observing  $n$  events given an expectation value of  $\mu$  events. The above calculation results in negligible systematic uncertainties. This method is cross-checked with an off-window coincidence method and a coincidence vertex method [15].

The second largest contamination at the far site is the correlated backgrounds from the Am-C neutron source. During the data taking, the Am-C neutron sources are parked inside the ACUs on top of the ADs. The energetic neutrons from these sources occasionally undergo an inelastic scattering with an iron nuclei resulting in gamma emissions, followed by a neutron capture on another iron nuclei with additional gamma emissions. When these

<sup>4</sup> The efficiency due to the fixed-time multiplicity cut is then  $P(0, 400\mu\text{s} \cdot R_p) \cdot P(0, 200\mu\text{s} \cdot R_d)$ .

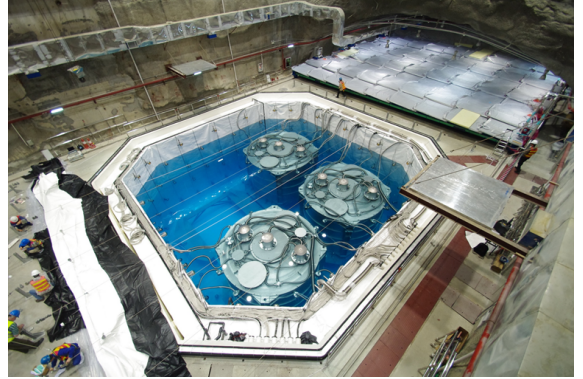
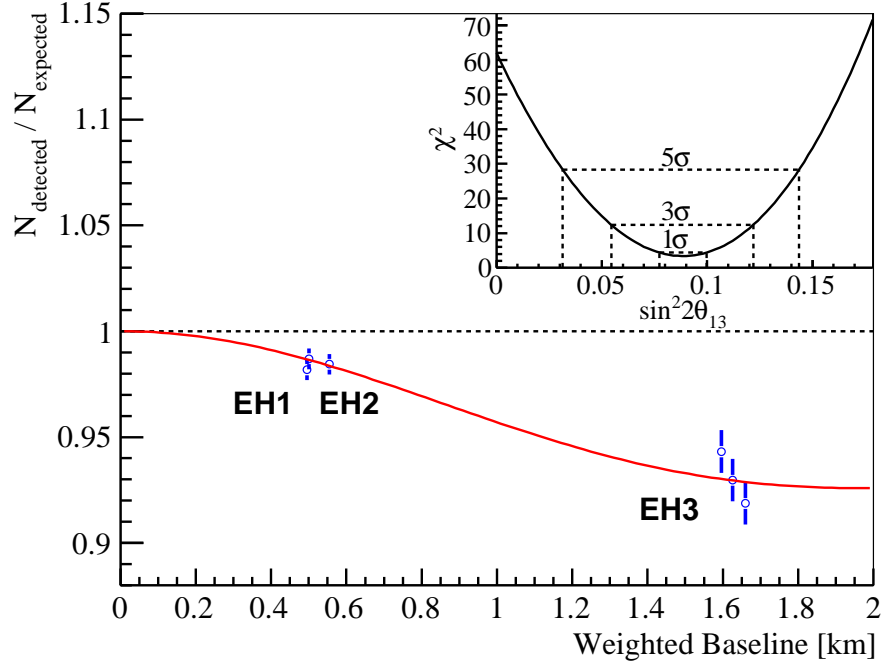


FIGURE 4. Three ADs were deployed in the EH3.

gammas are emitted toward AD, it is possible these correlated events could mimic an IBD signal. The contamination from the Am-C source, which is about 0.3% (0.03%) at the far (near) site, is calculated through a GEANT4-based Monte Carlo simulation, which can reproduce the energy spectrum of single backgrounds from Am-C sources. The systematic uncertainty of this correlated background is assumed to be 100%.

The  $^9\text{Li}/^8\text{He}$  and the fast neutrons are two major IBD contamination caused by cosmic muons. The nucleus of  $^9\text{Li}$  or  $^8\text{He}$  are produced from the carbon nucleus when cosmic muons pass through the liquid scintillator. The  $^9\text{Li}$  and  $^8\text{He}$ , with half lifetime of 257 ms and 172 ms, respectively, are both long lifetime beta emitters. They would undergo a beta decay providing a prompt-like signal. The daughter nuclei could then undergo a spontaneous fission, with a neutron emission in the final state resulting in a delay-like signal. Such a pair of correlated prompt-like and delay-like signal would mimic an IBD event. The contamination of  $^9\text{Li}/^8\text{He}$  can be directly measured by fitting the spectrum of time between the IBD candidate and the last tagged AD muon. The measured  $^9\text{Li}/^8\text{He}$  rates from all three experimental halls are consistent with an empirical formula of  $\alpha E_\mu^{0.74}$  given the average muon energy  $E_\mu$  in each site. Furthermore, the contamination are suppressed by an optimized AD shower muon cut described in the previous section. The remaining contamination is about 0.2% (0.35%) for the far (near) site with a 50% systematic uncertainty due to the fitting procedure.

The fast neutron backgrounds are caused by the energetic neutrons produced inside or outside the muon veto system. These energetic neutrons can undergo an elastic scattering with protons, leaving a prompt-like signal due to the proton recoil, followed by the neutron thermalization and then neutron capture on Gd producing a delay-like signal. The energy of the proton recoil signals ranges from sub MeV to tens of MeV. Therefore, one can extrapolate the measured fast neutron's prompt en-



**FIGURE 5.** The ratio between the measured and the expected signals in each detector vs. the flux-weighted average baseline, which is computed with reactor and survey data. The expected signals have been corrected with the best fit normalization parameter assuming no oscillation. The error bars represent the uncorrelated uncertainties. The oscillation survival probability at the best-fit value is plotted as the smooth curve. For clarity purpose, the AD4/6 data points are shifted by -30 and 30 m, respectively. The  $\chi^2$  value vs. the  $\sin^2 2\theta_{13}$  value is shown in the inner panel.

ergy spectrum above 15 MeV to the energy range of interests (0.7-12 MeV) in order to estimate the contamination in the IBD candidates. A flat background spectrum is assumed, which is confirmed by the spectrum of fast neutron events with muon tagging from water pools and RPC. The systematic uncertainty is constrained to about 30%. The contaminations due to fast neutron are estimated to be about 0.07% (0.12%) for the far (near) site.

The last contamination is the  $^{13}\text{C}(\alpha, n)^{16}\text{O}$  background caused by radioactivity inside ADs. The contamination is determined by Monte Carlo with measured alpha-decay rates. We identified four sources of alpha decays: the  $^{210}\text{Po}$  events and the decay chains from  $^{238}\text{U}$ ,  $^{232}\text{Th}$ , and  $^{227}\text{Ac}$ . The backgrounds are calculated to be about 0.05% (0.01%) for the far (near) site with a 50% systematic uncertainty. Altogether, the total backgrounds in the IBD sample are thus determined to be  $5 \pm 0.4\%$  and  $2 \pm 0.2\%$  for the far site and near sites, respectively.

## OSCILLATION ANALYSIS

The oscillation analysis includes data of 139 days (Dec. 24th 2011 - May 11th, 2012) with six ADs. Fig. 4 shows a picture of the three ADs in the EH3. The analysis pro-

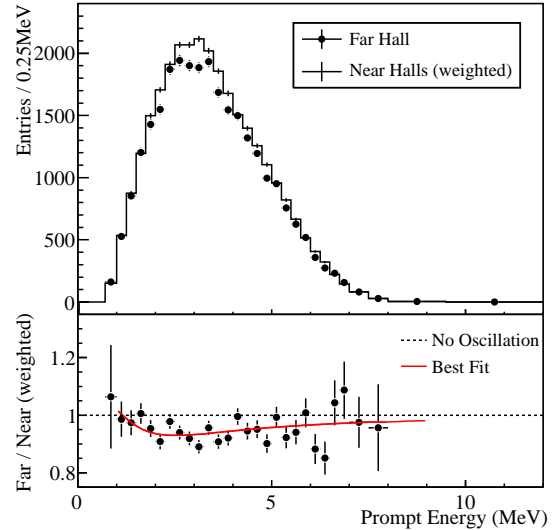


**FIGURE 6.** Top panel: Measured prompt energy spectrum at the far site (sum of three ADs) is compared with the predicted spectrum based on the measurements at the two near sites assuming no oscillation. Backgrounds are subtracted. Only statistical uncertainties are shown. Bottom panel: The ratio of the measured over the expected (no-oscillation) spectrum. The solid curve is the expected ratio vs. the true prompt energy with the neutrino oscillation for  $\sin^2 2\theta_{13} = 0.089$ .

cedure is described in details in Ref. [13, 15]. Since different experimental halls have different mountain overburdens, they also observe different muon rates. The average muon veto efficiency for six ADs in the three experimental halls are 0.8231, 0.8198 (EH1), 0.8576 (EH2), and 0.9813, 0.9813, 0.9810 (EH3). Besides the background-related uncertainties, the largest uncorrelated detector-related uncertainty (0.12%) is due to the 6 MeV energy cut in selecting delay signals. Other sizable uncorrelated detector-related uncertainties include 0.1% from the neutron Gd capture ratio, 0.03% from the number of target protons, and 0.02% from the spill-in effect. (The spill-in effect refers to that the IBD neutrons generated outside but captured inside the target GD-LS region outnumber the IBD neutrons generated inside but captured outside the GD-LS region. The reason for such imbalance is that thermal neutrons have a larger cross section to be captured on the Gd than the proton.) With the ratio method, the correlated detector-related uncertainty (about 1.9% in total) has negligible effects on the oscillation analysis. The same applies to the correlated reactor-related uncertainty. The uncorrelated reactor-related uncertainties include 0.5% from the received thermal power data, 0.6% from the calculated fission fractions, and 0.3% from the antineutrinos produced by the spent fuel. The total uncorrelated reactor-related uncertainty is 0.8%, which is further suppressed by about a factor of 20 in the oscillation analysis due to the multiple core/reactors configuration at Daya Bay.

The final antineutrino rates per day in the six ADs of three experimental halls, after corrections of the live-time, the veto efficiencies, and the background, are  $662.47 \pm 3.00$ ,  $670.87 \pm 3.01$  (EH1),  $613.53 \pm 2.69$  (EH2), and  $77.57 \pm 0.85$ ,  $76.62 \pm 0.85$ ,  $74.97 \pm 0.84$  (EH3). In the same experimental hall, the differences of AD rates stemming from ADs' different locations are consistent with expectation within statistical uncertainties. The deficit of antineutrino rate at the far site is quantified by the ratio of the measured far-hall IBD rate over the expected rate, which is calculated with the measured IBD rates of the near detectors assuming no oscillation. The resulting deficit is  $0.056 \pm 0.007$  (stat.)  $\pm 0.003$  (sys.).

The chi-square method with pull terms is used to extract  $\sin^2 2\theta_{13}$  within the standard 3-flavor oscillation model, in which the disappearance probability of the electron antineutrino is written as:

$$\begin{aligned} P(\bar{\nu}_e \rightarrow \bar{\nu}_e) &= 1 - \sin^2 2\theta_{13} \cos^2 \theta_{12} \sin^2 \Delta_{31} \\ &\quad - \sin^2 2\theta_{13} \sin^2 \theta_{12} \sin^2 \Delta_{32} \\ &\quad - \cos^4 \theta_{13} \sin^2 2\theta_{12} \sin^2 \Delta_{21}, \end{aligned} \quad (3)$$

with  $\Delta_{ij} \equiv |\Delta_{ij}| = 1.27 |\Delta m_{ij}^2| \frac{L(m)}{E(MeV)}$ . In this framework, the uncertainties from the backgrounds, detectors, reactor fluxes, and the oscillation parameters are taken into account properly in a consistent manner. The  $\sin^2 2\theta_{13}$

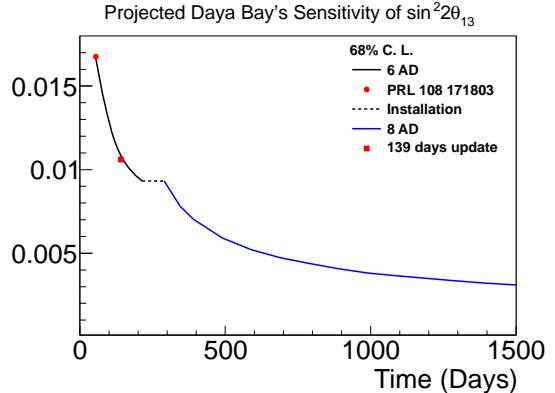


**FIGURE 7.** Projected  $\sin^2 2\theta_{13}$ 's sensitivity in terms of half of the 68% confidence interval of Daya Bay vs. the running time. The published and improved Daya Bay results are shown as red dots. The period of 6-AD data taking (black) is separated from the period of 8-AD data taking (blue) by an installation/calibration period (dashed).

is determined to be  $0.089 \pm 0.011$ . Fig. 5 shows the ratios of measured over expected IBD rates vs. weighted baseline for all ADs. The data are compared with the expected oscillation curve (red-solid line). Our improved measurement disfavors the  $\sin^2 2\theta_{13} = 0$  hypothesis at a 7.7 standard deviations.

## CONCLUSION AND OUTLOOK

In this talk, we reported an improved measurement of electron antineutrino disappearance at Daya Bay. The new results with 2.5 times more data confirms the previously published results [13], and improves the precision of  $\sin^2 2\theta_{13}$ . Currently, the total uncertainty is still dominated by the statistical uncertainty, which is about a factor of 2 larger than the systematic uncertainty. Fig. 7 shows the projected sensitivity of  $\sin^2 2\theta_{13}$  in terms of half of the 68% confidence interval with respect to the running time. With the full 8-AD configuration, we expect to achieve a  $\sim 5\%$  measurement of  $\sin^2 2\theta_{13}$  in about 3 years. Furthermore, the Daya Bay experiment also has the potential to measure the effective squared-mass difference  $\Delta m_{ee}^2$ , which is a combination of  $\Delta m_{31}^2$  and  $\Delta m_{32}^2$ , through the measurement of IBD energy spectrum distortion. Due to the short baseline  $< 2$  km, the measurement of  $\Delta m_{ee}^2$  is not sensitive to the neutrino mass hierarchy (sign of  $\Delta m_{32}^2$ ) [18]. In addition, the high statistics IBD samples from Daya Bay would provide the most precise measurement of the antineutrino energy spectrum, which is essential for the future measurements with reactor antineutrinos.

With the global efforts led by the Daya Bay experiment, the  $\sin^2 2\theta_{13}$  is found to be around 0.09. Such a large value of  $\sin^2 2\theta_{13}$  opens doors to two of the remaining unknown parameters in the neutrino sector, the CP phase  $\delta$  in the leptonic sector and the neutrino Mass Hierarchy<sup>5</sup>. In particular, the long baseline experiments [20, 21, 22, 23] can provide essential information for both parameters through the (anti) $\nu_e$  appearance from a (anti) $\nu_\mu$  beam. Meanwhile, the possibility of utilizing a medium baseline ( $\sim$ 60 km) reactor neutrino experiment to determine the neutrino mass hierarchy is also intensively discussed [24, 25, 26, 27, 18, 28]. We therefore expect a new era of discovery in the next couple of decades.

## ACKNOWLEDGMENTS

We would like to thank the support from Caltech and the National Science Foundation. The Daya Bay experiment is supported in part by the Ministry of Science and Technology of China, the United States Department of Energy, the Chinese Academy of Sciences, the National Natural Science Foundation of China, the Guangdong provincial government, the Shenzhen municipal government, the China Guangdong Nuclear Power Group, Shanghai Laboratory for Particle Physics and Cosmology, the Research Grants Council of the Hong Kong Special Administrative Region of China, University Development Fund of The University of Hong Kong, the MOE program for Research of Excellence at National Taiwan University, National Chiao-Tung University, and NSC fund support from Taiwan, the U.S. National Science Foundation, the Alfred P. Sloan Foundation, the Ministry of Education, Youth and Sports of the Czech Republic, the Czech Science Foundation, and the Joint Institute of Nuclear Research in Dubna, Russia. We thank Yellow River Engineering Consulting Co., Ltd. and China railway 15th Bureau Group Co., Ltd. for building the underground laboratory. We are grateful for the ongoing cooperation from the China Guangdong Nuclear Power Group and China Light & Power Company.

## REFERENCES

1. M. Goldhaber, L. Grodzins, and A. W. Sunyar, Phys. Rev. **109**, 1015 (1958).
2. R. D. McKeown and P. Vogel, Phys. Rep. **394**, 315 (2004).
3. B. Pontecorvo, Sov. Phys. JETP **6**, 429 (1957).
4. B. Pontecorvo, Sov. Phys. JETP **26**, 984 (1968).
5. Z. Maki, M. Nakagawa, and S. Sakata, Prog. Theor. Phys. **28**, 870 (1962).
6. M. Apollonio *et al.* [CHOOZ Collaboration], Phys. Lett. **B466**, 415 (1999).
7. M. Apollonio *et al.* [CHOOZ Collaboration], Eur. Phys. J. **C27**, 331 (2003).
8. G. Fogli *et al.*, Phys. Rev. Lett. **101**, 141801 (2008).
9. K. Abe *et al.* [T2K Collaboration], Phys. Rev. Lett. **107**, 041801 (2011).
10. P. Adamson *et al.* [MINOS Collaboration], Phys. Rev. Lett. **107**, 181802 (2011).
11. Y. Abe *et al.* [Double Chooz Collaboration], Phys. Rev. Lett. **108**, 131801 (2012).
12. L. A. Mikaelyan and V. V. Sinev, Phys. Atom. Nucl. **63**, 1002 (2000).
13. F. P. An *et al.* [Daya Bay Collaboration], Phys. Rev. Lett. **108**, 171803 (2012).
14. J. K. Ahn *et al.* [RENO Collaboration], Phys. Rev. Lett. **108**, 191802 (2012).
15. F. P. An *et al.* [Daya Bay Collaboration], arXiv:1210.6327 (2012), submitted to Chinese Physics C.
16. Daya Bay Collaboration, arXiv:hep-ex/0701029 (2006).
17. F. P. An *et al.* [Daya Bay Collaboration], Nucl. Inst. Method **A685**, 78 (2012).
18. X. Qian *et al.*, arXiv:1208.1551 (2012), submitted to Phys. Rev. D.
19. X. Qian *et al.*, arXiv:1210.3651 (2012), submitted to Phys. Rev. D.
20. K. Abe *et al.* [T2K Collaboration] Nucl. Inst. Method **A659**, 106 (2011).
21. D. Ayres *et al.* [NOvA Collaboration] The NOvA Technical Design Report. FERMILAB-DESIGN-2007-01 (2007).
22. T. Akiri *et al.* [LBNE Collaboration], arXiv:1110.6249 (2011).
23. K. Abe *et al.* [Hyper-K Collaboration], arXiv:1109.3262 (2011).
24. S. Choubey, S. T. Petcov, and M. Piai, Phys. Rev. **D68**, 113006 (2003).
25. J. G. Learned *et al.* Phys. Rev. **D78**, 071302R (2008).
26. L. Zhan *et al.* Phys. Rev. **D78**, 111103R (2008).
27. L. Zhan *et al.* Phys. Rev. **D79**, 073007 (2009).
28. E. Ciuffoli, J. Evaslin, and X. M. Zhang, arXiv:1209.2227 (2012).

<sup>5</sup> A Bayesian approach in presenting results/sensitivities of the neutrino mass hierarchy has been proposed in Ref. [19].

# Progress in the Construction of the MICE Cooling Channel

Tianhuan Luo, on behalf of the MICE collaboration

*Department of Physics and Astronomy, University of Mississippi, University, MS, 38677*

**Abstract.** The international Muon Ionization Cooling Experiment (MICE) aims to build and test one section of an ionization cooling channel. It is sited at the Rutherford Appleton Laboratory in the UK, utilizing the pulsed muon beam from the ISIS rapid cycling synchrotron. The major parts of MICE include two Spectrometer Solenoid (SS) modules, three Absorber-Focus-Coil (AFC) modules and two RF Coupling-Coil (RFCC) modules. The compact integration of large superconducting magnets, high gradient normal conducting RF system, strong magnetic field and a safe liquid hydrogen system makes this experiment technically challenging. In this paper we will introduce the recent construction progress on various components and the latest schedule for MICE.

*Contribution to NUFACt 12, 14th International Workshop on Neutrino Factories, Super beams and beta beams, July 23-28, 2012, JLAB and the College of William and Mary.*

**Keywords:** muon ionization cooling, accelerator instrumentation

**PACS:** 29.20.-c

## INTRODUCTION

The international Muon Ionization Cooling Experiment (MICE) at Rutherford Appleton Laboratory (RAL) [1, 2], shown in Figure 1, aims to build and test one cell of an ionization cooling lattice and is designed to achieve a 10% transverse emittance reduction. It mainly consists of three kinds of modules: two Spectrometer Solenoid (SS) modules to track the incoming and outgoing muon beams, three Absorber Focus Coil (AFC) modules to reduce the beam momentum in both longitudinal and transverse directions, and two RF Coupling Coil (RFCC) modules to compensate the longitudinal momentum loss. Both learning through engineering experience and benchmarking the ionization simulation code from MICE will be beneficial for building a future neutrino factory and muon collider.

The latest plan of MICE construction is divided into three steps, as shown in Figure 2, with data taken at each step. In Step I, the incoming muon beam is measured directly without any solenoid focusing, cooling or re-accelerating. The emittance measurement results and detailed discussions are presented in [3]. In Step IV, with the upstream and downstream SS module, and one AFC module in between, one can measure the beam emittance before and after the absorber and evaluate the ionization process. In Step VI, the full system is set up by adding two more AFC modules for more ionizing effect and two RFCC modules to compensate the longitudinal momentum loss in the AFC modules. The designed transverse emittance reduction is  $\approx 10\%$ , depending on the initial emittance. As of June 2012, Step I has been completed and Step IV and Step VI are now under construction.

## MICE STEP IV

The goal of Step IV is to measure the ratio of emittances before and after the absorber. The major instruments needed for this step are one AFC module and two SS modules. With two fiber trackers and liquid absorbers ready, solid absorbers and Electron Muon Ranger (EMR) installation almost ready, the construction work is focused on the AFC focus coil, liquid hydrogen ( $LH_2$ ) system and two spectrometer solenoids.

The AFC focus coil, as shown in Figure 3, provides the guiding magnetic field in the liquid hydrogen absorber. It consists of two superconducting coils which can be operated with the same (“solenoid mode”) or opposite (“flip mode”) polarities. As of June 2012, the radiation shields have been fitted and the cold mass has been installed and aligned. The first AFC focus coil is scheduled to arrive at RAL in July and the absorber integration will take another 3 months.

The liquid hydrogen ( $LH_2$ ) system provides the hydrogen for the absorber. The system layout is shown in Figure 4. As of June 2012, all the hardware has been completed, as well as the vacuum check, helium check and heater-chiller check. Before being connected to the absorber, the  $LH_2$  system will be connected to a test cryostat for a system test. The preparation of the system test is in progress.

The spectrometer solenoid provides a guiding magnetic field in the fiber tracker, which bends the muons to allow measurement of their momenta. Learning from the previous magnet training experience [4], modifications have been done to reduce the heat leak to the cold mass, increase the available cooling power and stabi-

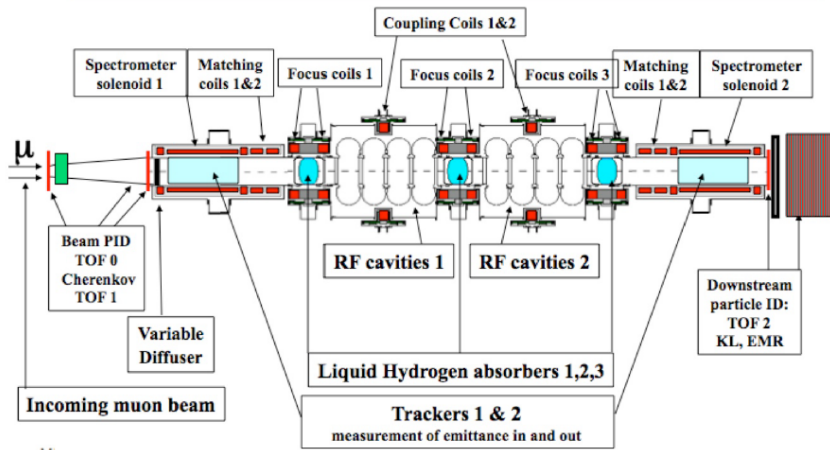


**FIGURE 1.** MICE layout.

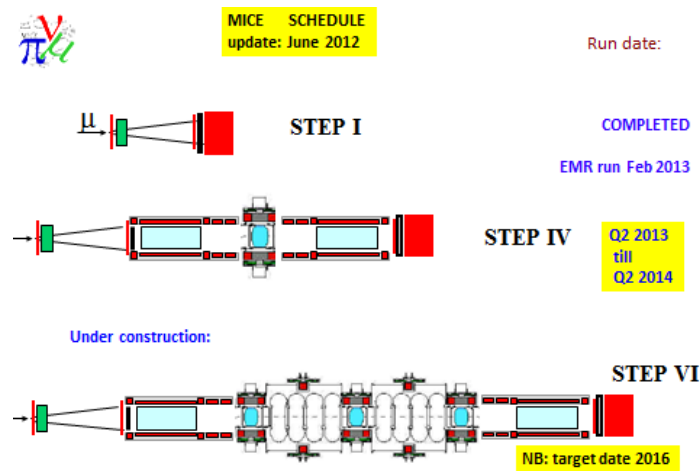


**FIGURE 2.** MICE schedule, updated in June 2012.



**FIGURE 3.** Absorber focus coil.

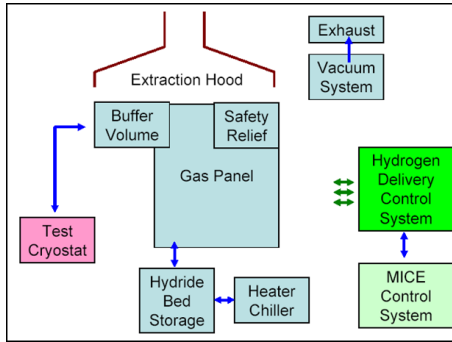


**FIGURE 4.** LH<sub>2</sub> system layout.

lize the LTS (low temperature superconducting) leads. For the first SS, the LTS and HTS (high temperature superconducting) leads which were burnt in the previous training have been replaced. After assembling the SS and cooling down the cold mass, the magnet training has resumed at the vendor, Wang NMR, in Livermore, California, as shown in Figures 5, 6 and 7. A DAQ quench protection system has been implemented by Fermilab, which can detect the quench initiation and propagation in the solenoids by measuring the voltage drop across each coil. It also monitors all the LTS and HTS leads for any possible lead failure. As of June 2012, the quench current of magnet training is going up steadily and on schedule.

The second SS is under assembly at Wang NMR. Its training will start after the training of the first SS is done.

## MICE STEP IV

From Step IV to Step VI, two RFCC modules are implemented to compensate the longitudinal momentum loss, and two more AFC modules are installed for more ion-



**FIGURE 5.** Spectrometer Solenoid training at Wang NMR.



**FIGURE 6.** Quench protection DAQ, instrumentation and power supply control.

ization effect with the total transverse emittance reduction estimated to be about 10%. The emittance measurement accuracy is required to be within 0.1%.

Each RFCC module [5] consists of four 201 MHz normal conducting RF cavities and one coupling coil. To improve the acceleration efficiency and suppress RF breakdown, beryllium windows are installed on the irises of the cavity. Ten cavities, eleven beryllium windows and ten RF windows have been manufactured and shipped to Lawrence Berkeley National Lab (LBNL). RF break-



**FIGURE 7.** Magnet quench.

down in the strong magnetic field is associated with the field emission electrons [6]. To suppress field emission, electropolishing (EP) has been carried out on one cavity, shown in Figure 8, to reduce the number of surface emitters. This cavity will be shipped to Fermilab, installed in a single cavity vacuum vessel, and tested in a strong magnetic field. EP of the rest cavities is planned to start at the end of 2012 at LBNL.



**FIGURE 8.** Setup of Electropolishing for the 201 MHz cavity.

The coupling coil (CC) provides the guiding magnetic field in the RF cavity. It is the largest superconducting coil in MICE. An external review of the CC design was held at LBNL in March 2012 and the detailed design was finished by June 2012. The first cold mass manufactured by Harbin Institute of Technology (HIT) has arrived at LBNL, shown in Figure 9. LBNL and Fermilab are now preparing the full current test of the cold mass. At LBNL, work on the cooling tube, quench protection circuit, vacuum potting and interface with the Fermilab test facility are underway. A cryostat, shown in Figure 10, has been shipped from the National High Magnetic Field Laboratory (NHMFL) to Fermilab. It will be modified and installed for the CC cold mass full current test. Fabrication of the CC cryostat has been planned and will be carried out at LBNL.



**FIGURE 9.** Coupling Coil cold mass at LBNL.



**FIGURE 10.** Cryostat from NHMFL for Coupling Coil cold mass test.

## CONCLUSIONS

The construction of the MICE cooling channel is making good progress. An updated schedule stages the construction process into three steps, with physics carried out in each step. We aim to complete the construction of Step IV in Q2 2013 and run the experiment from Q2 2013 to Q3 2014. The target date for Step VI is 2016, when we will fully demonstrate the muon ionization cooling.

## ACKNOWLEDGMENTS

The author would like to acknowledge the inputs and support from the MICE collaboration, especially from Prof. Gail Hanson, Prof. Daniel Kaplan and Prof. Don Summers, and the hospitality of LBNL Center of Beam Physics. The work is supported by NSF award 0959000.

## REFERENCES

1. G. Gregoire *et al.*, 2003, proposal to the Rutherford Appleton Laboratory, MICE-NOTE-GEN-0021, <http://mice.iit.edu/mnp/MICE0021.pdf>
2. M. Bogomilov *et al.*, JINST **7** (2012) P05009.
3. V. Blackmore, 2012, MICE Step I: First Measurement of Emittance with particle physics detector, this proceeding.
4. S. Virostek *et al.*, IEEE Trans. Appl. Supercond. **20** (2010) 377.
5. D. Li *et al.*, Progress on the MICE RFCC Module, IPAC-2012-THPPP093.
6. R. B. Palmer *et al.*, Phys. Rev. ST Accel. Beams **12** (2009) 031002.

# MICE Step I: First Measurement of Emittance with Particle Physics Detectors

V. Blackmore, on behalf of the MICE collaboration

*Department of Physics, University of Oxford, OX1 3RH*

**Abstract.** A novel single-particle technique to measure emittance has been developed and applied to seventeen different muon beams for the Muon Ionisation Cooling Experiment. The mean momenta of these beams varies from 173 to 271 MeV/c, with emittances on the order of 2 to 4 mm.rad horizontally and 0.8 to 1.2 mm.rad vertically. The measured parameters of the beams and the results of simulations are in agreement.

**Keywords:** muon ionisation cooling, accelerator instrumentation

**PACS:** 29.27.Fh

## INTRODUCTION

The Muon Ionisation Cooling Experiment (MICE) [1] will demonstrate the practicality of ionisation cooling, an essential technique for a future Neutrino Factory or Muon Collider. Muons are produced occupying a large volume of phase space that must be reduced for efficient acceleration. Ionisation cooling is the only technique that can reduce the emittance of these beams.

A beam of muons passing through low-Z material loses energy by ionisation. This reduces the beam divergence and the volume of occupied phase space. Longitudinal momentum is restored in accelerating cavities, maintaining the overall momentum of the beam, but its transverse emittance is reduced. A Neutrino Factory requires its large transverse emittance of  $\epsilon_N \approx 12 - 20$  mm.rad to be reduced to 2 – 5 mm.rad. These beams also possess a large momentum spread  $\approx 20$  MeV/c about a central momentum of 200 MeV/c. A Muon Collider would require more cooling.

MICE will measure the efficiency of one "SFOFO" lattice cell (Figure 1) based on the cooling channel design of the Neutrino Factory Feasibility Study [2], a superconducting lattice with a large momentum acceptance about 200 MeV/c. The lattice cell consists of two "focus" coil pairs that focus the beam onto low-Z absorbers, and two "coupling" coils surrounding two sets of four 200 MHz cavities. Single-particle measurements are necessary to explore the performance of the cooling channel as the expected reduction in emittance is  $\approx 10\%$ . Therefore, measurements of the beam before and after the cooling channel will be made with two scintillating fibre trackers contained in two superconducting solenoids known as the "spectrometer solenoids". Particle identification is provided by Cherenkov and time-of-flight (TOF) detectors, which also allow the muons to be timed with respect to the RF phase.

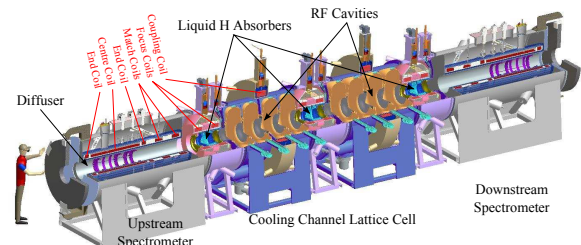


**FIGURE 1.** The MICE cooling channel lattice and detectors.

A realistic demonstration of cooling requires beams that closely resemble those expected at the front-end of a Neutrino Factory. These beams should cover a wide range of emittance so that ionisation cooling can be fully explored and understood. In MICE, the emittance range is obtained via a "diffuser", a variable thickness of high-Z material that can be inserted into the beam path upstream of the cooling channel. As cooling is a momentum-dependent process, it must be demonstrated over a range of beam momenta. MICE will demonstrate the cooling of 140 – 240 MeV/c beams with large momentum spreads using a selection of low-Z absorbers, including liquid hydrogen.

## THE MICE BEAM LINE

Figure 2 shows the MICE beam line [3]. Muons are created and transported through a quadrupole triplet, Q4–6, and are incident on a TOF station (TOF0) and two Cherenkov detectors. The final quadrupole triplet, Q7–9, transports the beam to another TOF station (TOF1). In later steps of MICE the diffuser and cooling channel will immediately follow TOF1.

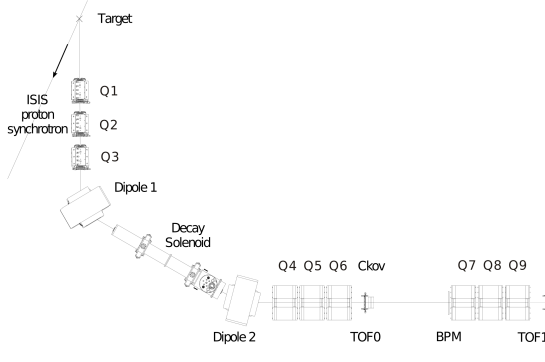


**FIGURE 2.** The MICE muon beam line.

The TOFs [4] consist of two perpendicular planes of 1 inch thick scintillating slabs coupled to photomultiplier tubes. Their timing resolutions are  $\sigma_{t0} = 51$  ps and  $\sigma_{t1} = 59.5$  ps for TOF0 and TOF1 respectively. The difference in arrival times of light at the end of each slab are used to obtain transverse position measurements with resolutions of  $\sigma_{x0} = 9.8$  mm at TOF0 and  $\sigma_{x1} = 11.4$  mm at TOF1 [5].

The initial beam line design used TURTLE [6], assuming a 1 cm thick lead diffuser. Further beam line settings were obtained by scaling the magnet currents of the baseline case. These settings will transport muons of correct momenta to the cooling channel, but are not necessarily well-matched since the diffuser introduces large amounts of scattering into the beam and changes its optical parameters. As the  $\beta$ -function decreases by the same ratio as emittance increases, the final optics and diffuser thickness require knowledge of the inherent emittance of the input beams.

Data were taken during Step I of MICE to verify simulations and determine the characteristics of the muon beam, particularly its momentum distribution and emittance. Only the TOF stations, TOF0 and TOF1, were used for the measurement at this stage.

## CHARACTERISATION OF THE MICE BEAMS

The beam line produces beams with large momentum spreads, and there is no single transfer matrix that applies to the entire beam. A new emittance measurement technique was developed to characterise each beam using single-particle measurements in the two TOF stations and tracking through the Q7–9 quadrupole triplet [5].

An initial estimate of  $p_z$  is made, assuming the muon travels on-axis between TOF0 and TOF1. The transfer matrix for the momentum estimate is calculated, and the trace-space vectors at each station can be determined

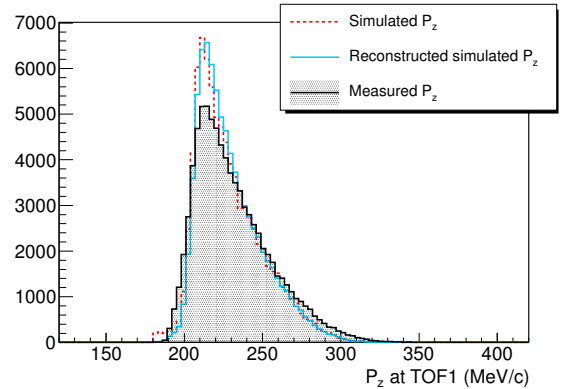


**FIGURE 3.** Longitudinal momentum,  $p_z$ , in simulation (red), reconstructed simulation (blue), and data (black) for a  $\mu^-$  beam.

from the position measurements by rearrangement of the transport equations:

$$\begin{pmatrix} x_1 \\ x'_1 \end{pmatrix} = \begin{pmatrix} M_{11} & M_{12} \\ M_{21} & M_{22} \end{pmatrix} \begin{pmatrix} x_0 \\ x'_0 \end{pmatrix},$$

i.e. in the horizontal plane,

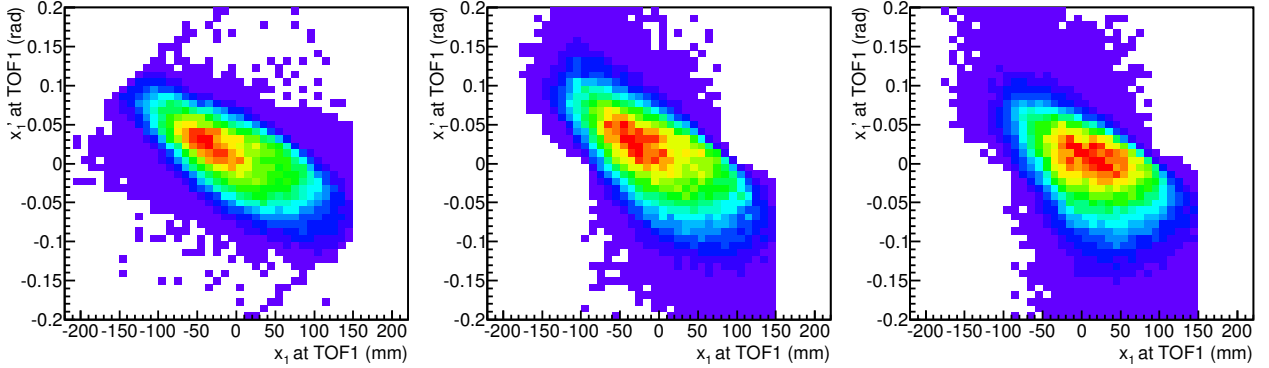
$$\begin{pmatrix} x'_0 \\ x'_1 \end{pmatrix} = \frac{1}{M_{12}} \begin{pmatrix} -M_{11} & 1 \\ -1 & M_{22} \end{pmatrix} \begin{pmatrix} x_0 \\ x_1 \end{pmatrix}, \quad (1)$$

where  $(x_0, x'_0)$  and  $(x_1, x'_1)$  are the trace-space vectors at TOF0 and TOF1 respectively. A new estimate of the muon momentum can be made along with corrections to its path through Q7–9, producing a further improved estimate of the trace-space vectors. This process is repeated several times, leading to measurement of the momentum distributions and trace-space covariance matrices,  $\Sigma_{x,y}$  at the upstream side of TOF1 for each muon beam.

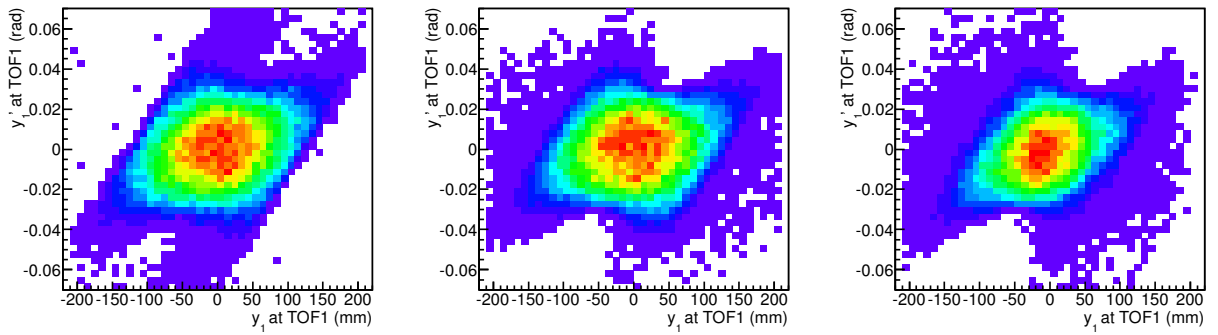
The efficiency of the reconstruction algorithm was determined by a Monte Carlo simulation. G4Beamline [7] tracked particles from the target to TOF0, then G4MICE [5] was used to track muons between TOF0 and TOF1. All simulations contained descriptions of beam line elements and materials, and the reconstruction smeared the simulated times and positions according to detector resolutions.

Figure 3 shows the agreement between measured and simulated momenta. The measured momentum distribution is shown in black (shaded). All distributions agree well in both shape and width, although the  $\mu^+$  distributions have a broader momentum spread due to the additional proton absorber in the beam path.

Figures 4 and 5 compare the trace-space distributions between simulation (left), reconstructed simulation (middle), and measured data (right). The effect of smearing is apparent in reconstructed trace-space, however, the



**FIGURE 4.** Horizontal trace space as measured at TOF1: (left) Simulation, (middle) reconstructed simulation, (right) data.



**FIGURE 5.** Vertical trace space as measured at TOF1: (left) Simulation, (middle) reconstructed simulation, (right) data.

simulations reproduce many of the characteristics of the measured beam. The boundaries of the distributions represent the quadrupole apertures translated to TOF1.

The amplitude of a muon can be expressed in terms of  $\chi^2$ , where

$$\chi^2 = \begin{pmatrix} x - \bar{x} \\ x' - \bar{x}' \end{pmatrix} \Sigma_x^{-1} (x - \bar{x}, x' - \bar{x}') = \frac{A_x}{\varepsilon_x},$$

$A_x$  is the amplitude of the muon and  $\varepsilon_x = \det \Sigma_x$  is the emittance of the beam. The  $\chi^2$  distribution is demonstrated in Figure 6, where the values for data (black, shaded) and reconstructed simulation (blue) are compared. The beam has a quasi-Gaussian core and non-Gaussian tail. High amplitude muons are outside the acceptance of the cooling channel; these were removed from further analysis by applying a cut at  $\chi^2 = 10$ .

Optical functions and emittances were determined from the covariance matrices as

$$\begin{aligned} \varepsilon_x &= \det \Sigma_x \\ \beta_x &= \frac{\Sigma_{x,11}}{\varepsilon_x} \end{aligned}$$

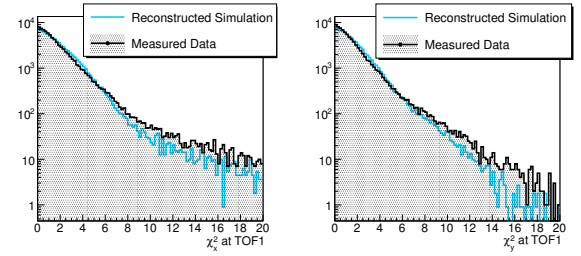


**FIGURE 6.**  $\chi^2$  distributions in  $x$  (left) and  $y$  (right). Measured data in black (shaded), reconstructed simulation in blue.

$$\alpha_x = -\frac{\Sigma_{x,12}}{\varepsilon_x}$$

and similarly for  $y$ . However, the beams have a large momentum spread and simulations show that  $\alpha$  and  $\beta$  vary with momentum across the whole beam. The measured optical parameters are, therefore, effective parameters that describe the distributions in trace-space. Figures 7 and 8 compare the measured rms-emittance, in  $x$  and  $y$  respectively, to the available simulations. The agreement is good in the horizontal plane, but the measured verti-

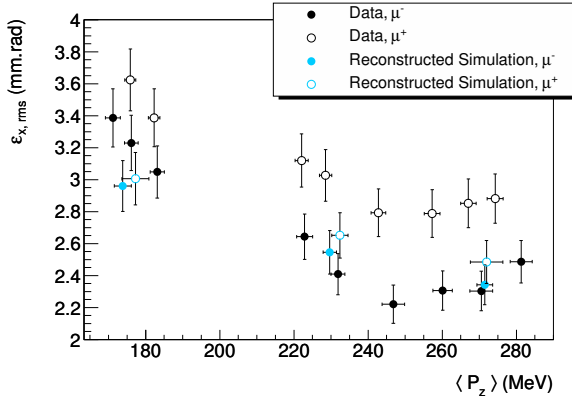


**FIGURE 7.** Emittance versus  $p_z$  at TOF1 for (black) data and (blue) reconstructed simulation in the horizontal plane.

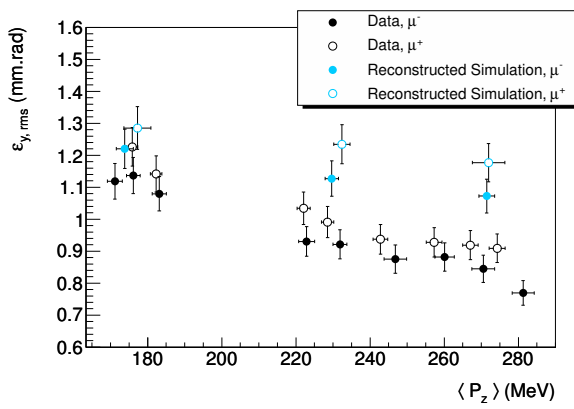


**FIGURE 8.** Emittance versus  $p_z$  at TOF1 for (black) data and (blue) reconstructed simulation in the vertical plane.

cal emittance is consistently smaller at higher momenta, possibly due to scraping in the final quadrupole triplet.

## SUMMARY

A single-particle method using two TOF detectors has been demonstrated to measure the properties of the MICE muon beams. Momentum measurements using this technique will be complementary to measurements using the spectrometer solenoids. Trace-space distributions at the entrance to MICE were also determined, and emittances of  $\approx 2$  to  $4$  mm.rad horizontally and  $0.8$  to  $1.2$  mm.rad vertically were measured.

## ACKNOWLEDGEMENTS

The input and support of the MICE Collaboration is gratefully acknowledged. This work was supported by

STFC and is generously hosted at the Rutherford Appleton Laboratory, UK.

## REFERENCES

1. 'Proposal to the Rutherford Appleton Laboratory: an international muon ionisation cooling experiment (MICE)', A. Blondel *et. al.*, MICE-NOTE-21 (2003)
2. 'Feasibility Study-II of a Muon-Based Neutrino Source', ed., S. Ozaki, R. Palmer, M. Zisman, and J. Gallardo, BNL-52623 (2001)
3. 'The MICE muon beam on ISIS and the beam-line instrumentation of the Muon Ionisation Cooling Experiment', M. Bogomilov *et. al.*, JINST 7 P05009 (2012)
4. 'The design and commissioning of the MICE upstream time-of-flight system', R. Bertoni *et. al.*, Nucl.Instrum.Meth. A615 (2010) 14–26, hep-ph/001.4426
5. M. A. Rayner, Oxford University DPhil Thesis, Oxford, England (2011)
6. 'Design and expected performance of the muon beamline for the Muon Ionisation Cooling Experiment', K. Tilley *et. al.*, Proc. 10th European Particle Accelerator Conference (EPAC 06)
7. 'A Swiss army knife for Geant4, optimized for simulating beam lines', T. J. Roberts  
<http://www.muonsinc.com/tiki-index.php>

# Imaging of internal density structure of volcanoes with cosmic muon : past and recent works

Seigo Miyamoto\*, Hiroyuki Tanaka\*, and V. Tioukov\*\*

\*Earthquake Research Institute, the university of Tokyo 1-1-1, Yayoi, Bunkyo, Tokyo 113-0032, Japan

\*\*Sezione di Napoli, Istituto Nazionale di Fisica Nucleare (INFN), via Cintia, I-80126, Naples, Italy

**Abstract.** The original idea of radiography by using cosmic-ray muons is very old. The researchers have been tried to find something hidden in various structure. Unfortunately they couldn't find anything new at that time. Meanwhile the muon detection technology has been highly developed till today. The first successful work was done by Tanaka et al (2007). They also succeeded to detect the internal structure of the shallow conduit in an active volcano, Mt. Asama. They have been succeeded to make the internal image of several volcanoes in Japan. The most recent innovative work was the observation of the seismic fault zones in Itoigawa-Shizuoka Tectonic Line by Tanaka et al in 2010. The plastic scintillator bar and photo multiplier array detected another hidden fault. The decreases of muon flux and time delay in a certain part of the fault outcrop in many days were also observed. I will give a review of the past and recent works of muon radiography.

**Keywords:** muon, radiography, volcanology, cosmic-ray, scintillation detector, nuclear emulsion

**PACS:** 96.50.S-, 29.40.Rg 91.40.-k, 14.60.Ef, 29.40.Mc

## INTRODUCTION

The cosmic-ray muons are produced by the interactions of primary high energy protons and the molecules in the sky. The energy peak is 1 GeV at the zenith angle = 0 degree and the flux decrease with  $E^{-2.7}$ . The high energy cosmic-ray muon can penetrate the rock which has the thickness more than 1 km. So it is possible to make the internal structure of big material by detecting the attenuation of cosmic-ray muons and the researchers have been tried to find something hidden in a big material[1]. Meanwhile, the muon detection technologies have been developed in high energy physics. That makes the recent innovative works especially for imaging the internal structure of volcanoes.

## THE PRINCIPLE OF MUON RADIOGRAPHY

One of the easy solutions to understand the basic principle of muon radiography is to see the analogy with X-ray examination. X-ray generator is corresponding to cosmic-ray muons, the human body is corresponding to the target material to be clarified the internal structure of it, and the X-ray film is corresponding to the muon detector.

The following is the procedures to make a projected average density map of the target material:

- i) Make the muon path length map in the target material in various azimuth and zenith angle

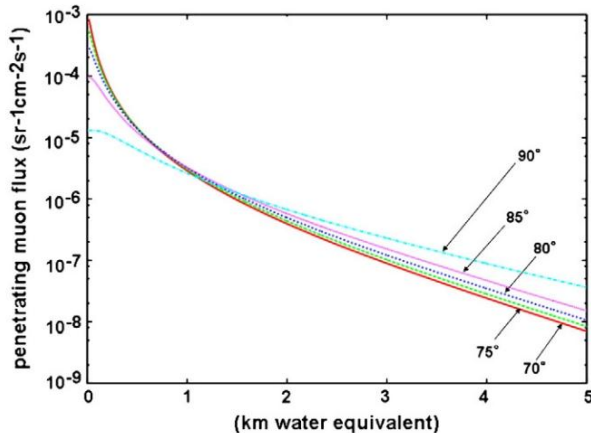
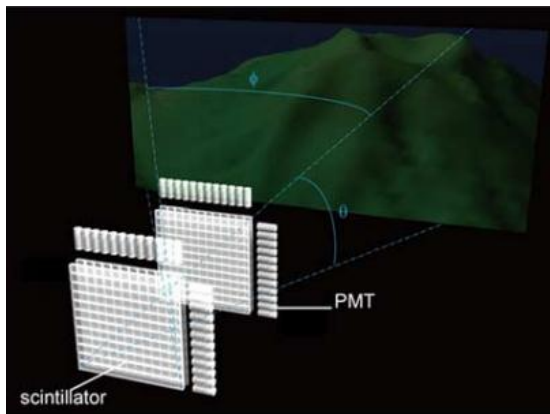
- ii) direction. The detector position, direction measured by GPS or the gyro and the digital elevation map is typically used for calculate the muon path in the case of volcano imaging. Measure the number of the penetrating muon and calculate the muon attenuation ratio in each direction.
- iii) The muon energy spectrum and the energy deposit in each energy and the material are well known. So we can calculate the range, which is density times muon path length( FIGURE 1 ).
- iv) The projected average density is determined by (range)/(muon path length).

## The features of muon detectors

There are two types of detectors roughly, which is sensitive for the minimum ionization particles. The first is electronic detectors, for example scintillator + PMT array(FIGURE 2.), gas detector, silicon detectors, so on. The second is photo graphic detector, which is called nuclear emulsion([2], FIGURE 3.) and high speed muon track readout systems[3]. The features of these two detectors are tabulated in TABLE 1. The main differences are the necessity for electricity and the real-time monitoring is available or not. The nuclear emulsion film detector doesn't need electricity, while real-time monitoring is not available. The time information can be added to nuclear emulsion film detector [4].

**TABLE 1.** The advantages and dis-advantages of Electronic detectors and photographic detectors for muon radiography.

Column Header Goes Here	Electronic detector	Photographic film detector
Power supply	Need electricity	No electricity
Portability	need large space	compact
Stability for environment	Need protection for water and shock	Stable for shock, water and low temperature, but unstable in more than 25 C
DAQ	Real time monitoring	Need development and analysis by readout system
Spread of the technology	High	Low

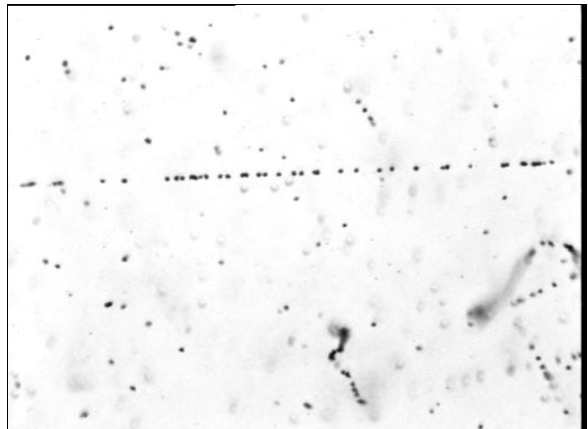
**FIGURE 1.** Integrated flux of cosmic-ray muons at various zenith angles penetrating through a given thickness of rock. The thickness is given in km-water-equivalent.**FIGURE 2.** The conceptual diagram of detecting muon by scintillator array + PMT.

## RECENT WORKS

### The first successful result of muon radiography

The first successful work was done by Tanaka et al., they succeeded to observe the shallow conduit in an

active volcano, Mt. Asama(2007)[5,6,7]. They placed the 0.2m<sup>2</sup> nuclear emulsion detector in the small room one km far from the creator for 2 months. The image of the dense rock in the cap of the conduit and lower density below the cap, which is thought as drain back phenomenon was observed.

**FIGURE 3.** The microscopic view of the nuclear emulsion film. The field of view is about 150 micron horizontally and 100 micron vertically. The aligned grains passes through the center of picture horizontally is the trajectory of muon. The curved trajectory is several hundreds keV of electron.

### The imaging of volcanoes by muon radiography

They also succeeded to observe the internal structure of lava dome in Showa-shinzan(2007)[8]. There were some lava dome growth model theories [9] before this observation.

Satsuma-Iwojima is an active volcano located in the south part of Japan. One of the main features volcanologists were interested in is the continuous gas emission during more than 10,000 years. Some of them made the magma convection model in the conduit. The water-rich magma is less dense than water-poor magma. That makes the magma convection in the conduit and when the pressure decreases, they start bubbling and emit volcanic gas. Tanaka et al. observed the lower density region in this volcano, which is the magma bubbling part[10].

The stereo graphic observation is possible also in muon radiography. The unknown parameters exist-

when we see the 3D object by just two directions projections, so there should be some assumption for the numerical model to solve the 3D density structure map. Taira et al succeeded to make 3D density map for Mt Asama[11].

The gravity measurement is one of probe to see the density structure in the ground. The common point for muon radiography and gravity measurement is sensitivity for the density. So the joint 3D density map inversion is possible by using muon radiography data and gravity measurement data. Nishiyama et al achieved to apply this method for Mt. Showa-Shinzan in 2012.

### The hidden fault search and rainfall water monitoring

The observation of the fault along Itoigawa-Shizuoka Techtonic Line(ISTL) was one of most innovative recent works[12]. ISTL is a one of largest fault in Japan. There is a known fault outcrop in Itoigawa and we can see the fault directly, however it's not parallel to ISTL. The main purposes of this observation are (1) to measure the detail information about fault already known. For example, the width of crushed zone, the porosity, and the permeability and whether they change with depth and (2) to discover another fault hidden around this region.

The 0.4m<sup>2</sup> scintillator array was located 6 m from the fault outcrop for two weeks. The results were the following:

- i) The width of crushed zone in the fault is about 20m and the porosity is about 20%.
- ii) The time dependence of the density in the fault was observed(FIGURE 4.). This data clarify the permeability of this fault.
- iii) Another hidden fault parallel to ISTL was found. The width and the permeability are similar with pre-existed fault.

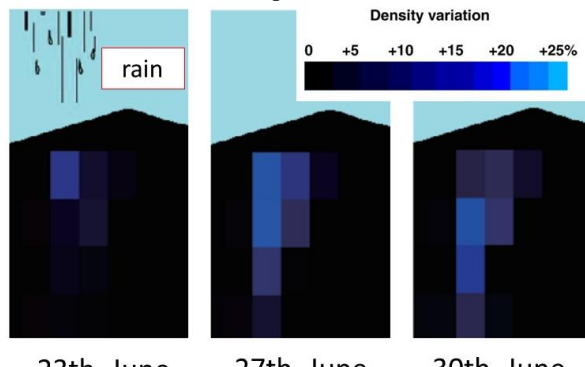


**FIGURE 4.** The time dependence of density variation in the fault before and after rainfall. The brighter blue represents the more dense part, which is due to rainfall water immersion.

## GOING-ON PROJECTS

### Imaging of latest lava dome in Mt. Unzen, Japan

The lava dome in Mt. Unzen was formed in the eruption from January 1991 to early 1995 and the activity calmed down in 1995. The researchers kept to observe the eruption in this period precisely[13,14,15]. Some of them proposed the lava dome growth model, another person proposed different model from their data[16,17]. It is significant for the growth model of lava dome which has viscous magma to investigate the density structure in it. The observation of the lava dome density 2D map was performed by using cosmic-ray muon and muon detector in Unzen. The muon detector, nuclear emulsion films which has high position resolution and 0.8m<sup>2</sup> effective area, was installed in a natural cave from early December 2010 to the end of March. The developed nuclear emulsion films have been scanned by automated muon readout system[18]. The muon detection efficiency is estimated from muon detector it precisely. The systematic analysis of efficiency and random noise ratio are performed by taking a pattern match and making a connection of muon tracks between three films. After estimation and removing unwanted low energy electron tracks, the density map of Unzen lava dome we got as a preliminary result(FIGURE. 5).

### The imaging internal density structure of shallow conduit in Stromboli, Italy

Stromboli is one of the Aeolian Islands, which is located at a volcanic arc north of Sicily Island Italy. 1m<sup>2</sup> nuclear emulsion films were installed at the site which is 500m far from active volcanic conduit and was exposed for about 5 months. The shape of volcanic conduit is critical information to the study of the dynamics of eruption. The films were developed and we started to analyze them in the beginning of May 2012. Scanning and analysis of about 10% of data demonstrated that the data are of a good quality and the mountain profile is clearly visible as very preliminary result( FIGURE 6.).

The full data set is expected to be scanned and analyzed to the end of the year. More realistic MC and precise positioning information can be necessary for the data interpretation.

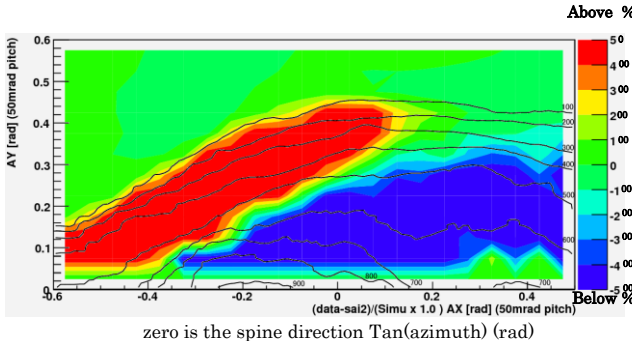


**FIGURE 5.** Preliminary muon excess anomaly ratio from the expected number of muons when we assume the density  $2.5\text{g}/\text{cm}^3$  uniform are represented as color variation in each direction by using 16% of effective area data. The red color region means more muons and the blue color region means less muons than expected. The blue color region doesn't have enough statistics.

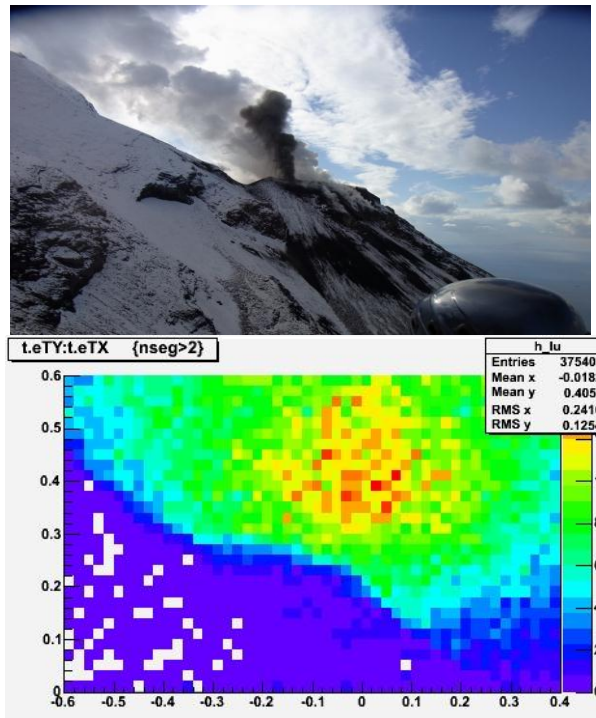


**FIGURE 6.** The photograph from detector place to the Stromboli vent is shown in the upper row and the number of detected muons is plotted in the lower row as very preliminary result.

## ACKNOWLEDGMENTS

The authors are deeply indebted to N. Nakamura and N. Naganawa of Nagoya University and H. Shimizu and T. Matsushima of Kyushu University for their valuable contributions. The Unzen lava dome and the Stromboli conduit observation was not done without P. Strolin, G. De Lellis, and V. Tioukov of the University of Napoli and C. Bozza of the University of

Salerno, Italy. Special funding arrangements by S. Okubo and related people of ERI are acknowledged.

## REFERENCES

1. L.W. Alvarez, et al., Science 167 (1970) 832.
2. T. Nakamura et al., Nuclear Instruments and Methods in Physics Research A, 556, (2006) 80.
3. K. Morishima and T. Nakano, JINST Volume: 5 Article Number: P04011, 2010.
4. S. Aoki et al., ADVANCES IN SPACE RESEARCH, Vol 37, (2006)2120.
5. H. Tanaka et al., Earth and Planetary Science Letters 263 (2007) 104–113.
6. H. Tanaka et al., Nuclear Instruments and Methods in Physics Research A 575 (2007) 489–497.
7. H. Tanaka et al., American Journal of Science, Vol.308, P.843–850, September, 2008.
8. H. Tanaka et al., GEOPHYSICAL RESEARCH LETTERS, VOL. 34, L22311, (2007).
9. I. Yokoyama , Proc. Japan Acad., 78, Sec B Vol. 78(B), (2002)
10. H. Tanaka et al., GEOPHYSICAL RESEARCH LETTERS, VOL. 36, L01304, (2009).
11. H. Taira et al., JOURNAL OF GEOPHYSICAL RESEARCH, VOL. 115, B12332, (2010).
12. H. Tanaka et al., Earth and Planetary Science Letters 306 (2011) 156–162
13. T. Umakoshi et al., Journal of Volcanology and Geothermal Research 175 (2008) 91–99
14. H. Sato et al., Nature 360, 664 - 666 (17 December 1992).
15. S. Nakada et al., Journal of Volcanology and Geothermal Research Vol. 54, Issues 3–4, January 1993, Pages 319–333
16. S. Nakada et al., Geology; February 1995; v. 23; no. 2; p. 157–160
17. K. Ohta, Chinetsu, vol.33 No.4 1996
18. C. Bozza et al., Nuclear Instruments and Methods in Physics Research A 568 (2006) 578–587

# Mu2e: A search for Charged Lepton Flavor Violation at FNAL

Ed V. Hungerford<sup>\*†</sup>

<sup>\*</sup>Department of Physics, University of Houston, Houston, TX 77204

**Abstract.** High intensity particle beams coupled with modern electronics allow precision studies of rare events with unprecedented precision. Rare muon decays are particularly interesting since copious muons can be produced and these have relatively long lifetimes. Although studies of muon decay have a long history, new experiments can attain sensitivities at levels which challenge many extensions to the standard model. Indeed, most extensions predict charged lepton flavor violation(cLFV) at rates within reach of present experimental technology. This paper describes the present status of the Mu2e experiment which is a search for the direct neutrino-less conversion of a muon into an electron at a sensitivity in the branching ratio of  $10^{-16}$ .

## INTRODUCTION

One of the most significant physics achievements in the past 15 years has been the confirmation that neutrino favors mix, and therefore violate lepton flavor(LFV) [1]. However, flavor violation due to small neutrino masses can be inserted into the Standard Model(SM) without defining new physical processes as they introduce cLFV rates too small(on the order of  $10^{-54}$ ) to be experimentally observed [2]. Thus an observation of cLFV implies new physics. Because of this, rare muon decays and interactions are of particular interest since they are sensitive to many Beyond the Standard Model physics (BSM) at a level which could be observed in high-precision experiments. Indeed, most BSM extensions predict cLFV at rates higher than the present experimental limits, so some suppression mechanism, (e.g. the GIM mechanism [3] or R parity [4] ) are required to reduce the rate below the present limits of observation. The Mu2e experiments is motivated by new experimental technologies, particularly new facilities producing intense muon beams, which allow cLFV limits to be lowered by several orders of magnitude. Mu2e would either lower the present limit of cLFV processes by at least 2 orders of magnitude, and thus severely constraining many BSM, or verify cLFV, quantifying the parameter space of a model.

---

<sup>1)</sup> <sup>†</sup>For the Mu2E collaboration - <http://mu2e-docdb.fnal.gov>

## I DESCRIPTION OF THE EXPERIMENT

There are three important cLFV muon decays;  $\mu \rightarrow e\gamma$  with an experimental upper limit of  $2.4 \times 10^{-12}$  [5];  $\mu^+ \rightarrow e^+e^-e^+$  with an experimental upper limit of  $1.0 \times 10^{-12}$  [6]; and  $\mu e$  with an experimental upper limit of  $6.1 \times 10^{-13}$  [7]. Mu2e is the direct muon to electron conversion without neutrino emission. In comparison to the LHC, it can reach physics processes at higher mass scales, and even if cLFV is discovered, the various rare muon decays can characterize the physics. This is illustrated in Figure 1 which is a semi-model-independent representation of sensitivity differences between  $\mu \rightarrow e$  and  $\mu \rightarrow e\gamma$ . It indicates a typical new physics scale,  $\Lambda$ , where the new physics contribution either couples electromagnetically ( $\kappa < 1$ ) or by some other mechanism which is treated as a point contact interaction ( $\kappa > 1$ ). Obviously, a  $\mu \rightarrow e$  experiment at a sensitivity of  $10^{-16}$  probes effective mass scales of at least several thousand TeV, and the ratio of  $\mu \rightarrow e$  to  $\mu \rightarrow e\gamma$  indicates the BSM interaction. The excluded regions result from references [5] and [7].

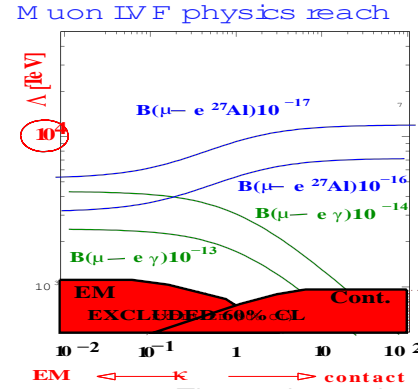


FIGURE 1. The reach on the mass scale,  $\Lambda$  in TeV and sensitivity of  $\mu \rightarrow e\gamma$  vs  $\mu \rightarrow e$

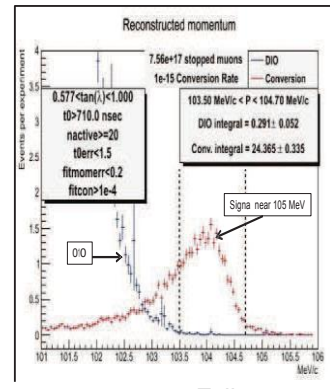


FIGURE 2. Fully reconstructed signal with backgrounds

Mu2e uses an intense, pulsed muon beam of negative muons which is brought to rest in an Aluminum target. These stopped muons are then captured in atomic orbits forming muonic atoms, which either decay in orbit(DIO) or interact with the nucleus via the weak interaction emitting nucleons, photons, electrons, and neutrinos. In free, unbound muon decay,  $\mu^- \rightarrow e^- \nu_e \bar{\nu}_e$ , the electron recoils against neutrinos resulting in a distribution of electron energies with a maximum of approximately one-half the muon mass. On the other hand, when the muon is bound to a nucleus, the recoiling nucleus can take away momentum but little energy, so the end point energy of the electron spectrum is approximately equal to the muon mass. However, the DIO spectrum falls rapidly as  $E_e$  approaches the end point as

approximately  $(E - E_{\text{max}})^5$  [8]. These processes are background to cLFV coherent decay, where the electron recoils against the nucleus without neutrino emission. In this case the only final state particles are an electron and the nucleus, so that the recoil energy is uniquely determined, producing a peak in the electron energy spectrum approximately equal to the muon mass.

Figure 2 shows the results of a simulation of the  $\mu \rightarrow e$ . experiment. The simulation has all backgrounds including “exact” DIO and full fluctuations in particle tracks such as scattering and energy loss with pattern recognition, and reconstruction also included. A simulated signal with spectrum cuts for a 3 year run (single event sensitivity of  $\approx 10^{-17}$ ) is also shown. The peak in energy of the electron is down-shifted from the muon mass of 105 MeV by kinematics, atomic muon binding energy, and energy loss in the detector. Thus the crucial issue in a  $\mu \rightarrow e$  experiment is the ability to resolve a mono-energetic electron peak in the presence of DIO background, and this is primarily a function of energy resolution and all suppression of background.

Figure 3 shows the  $\mu \rightarrow e$  apparatus. A pulsed, 8 GeV proton beam from the Fermi Laboratory, FNAL, accelerator complex is transported to a 16 cm long W production target inside a solenoidal magnetic field. The field from the production target to the stopping target is graded from 5 down to 1 T. This pushes the helical trajectories down stream, preventing magnetic traps at joints between the solenoids, and increasing the efficiency by reflecting particles originally emitted outside the transport and detection solid angles. The field is constant in the region of the detection package. The primary beam produces pions, which with their decay muons are captured in the magnetic field, and transported to the detector solenoid where the muons are brought to rest in a set of 17 Al foils. The lifetime of the muonic atom formed in the stopping target, sets the repetition rate of the proton beam. This allows the beam components which do not stop to pass unseen through a 78cm central hole in the detectors, as they are only activated between beam spills, reducing beam dependent backgrounds.

The approximately 3m long electron tracker in the detector package is designed to measure the parameters of the helical trajectory of electrons emitted from the stopping target. The solenoidal field and the size of the central hole in the detec-

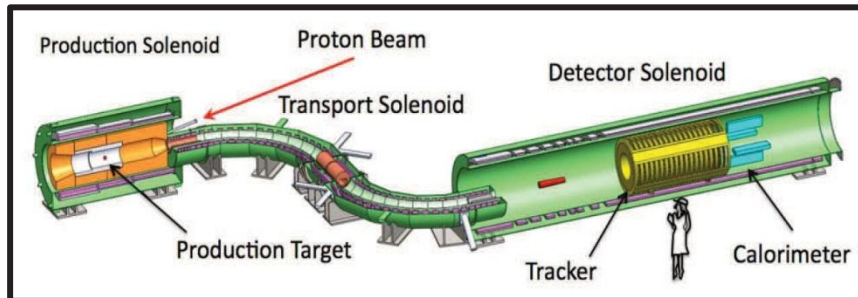


FIGURE 3. The  $\mu \rightarrow e$  apparatus

tor package only allows particles with momenta  $> 60 \text{ MeV}/c$  to hit the detector. The reconstructed helix gives the momentum of the electrons with a resolution of approximately  $\sigma = 150 \text{ keV}/c$ . The tracker is constructed of planes composed of straw tube panels of 5 mm diameter straw tubes. The curved transport solenoid, causes particles to drift perpendicular to the bend plane, and allows the beam to be selectively cut in momentum, charge, and thus particle ID. Located at the center of the transport solenoid is an anti-proton absorber.

Both timing and pulse height information are recorded from each end of a straw anode wire. Pulse height is used to discriminate against low-energy, heavily ionizing tracks (e.g. protons), and to improve timing resolution by removing threshold “walk”. The calorimeter is composed of approximately 1000 LYSO crystals. It is read by avalanche photo-diodes(APD), and placed behind the electron tracker. The calorimeter provides a coincident, redundant although poorer, energy measurement of the electron. It also gives redundant timing for the event, particle ID, and an independent, spatial measure of a position on the track trajectory. Redundant measurements of important parameters are always essential in precision measurements.

Detector rates are high and front-end electronics are placed within the vacuum of the solenoidal vacuum on the detector frames. The readout is trigger-less with optical coupling through the vacuum walls to an event builder in the DAQ. The trigger-less DAQ has a total data rate of 30 GBytes/sec.

Tracker inefficiencies and background hits must be properly handled in trajectory reconstructions, and cosmic muons may enter, or decay in (or near), the tracking detector inducing, a background which must also be identified and removed. An active cosmic ray shield is placed to veto by software, events that are coincident with a detector track. All backgrounds including event reconstruction, as shown in Figure 2, are less than one-half an event at the proposed single event sensitivity in a 3-year run of  $3 \times 10^{-17}$ . Data acquisition is anticipated starting in 2019.

As always, there is always the caveat that in rare decays unanticipated backgrounds limit any experiment. Thus continued detailed study using realistic detector design and performance is required, and is ongoing.

## REFERENCES

1. Y. Ashie, et al, Phys. Rev. Lett.93(2004)200, and references therein.
2. Cheng T. P., and Li L., Phys. Rev. D16(1977) 1425; B. Lee, Robert Shrock, , Phys. Rev.D 16(1977)1444
3. S. L. Glashow, J. Iliopoulos, and L. Maiani, Phys. Rev.D 2 (1970)1285
4. R. Barbier, et al.,Phys. Rept.420(2005)1-195
5. J. Adam, et al., Phys. Rev. Lett.107(2011) 171801
6. U. Bellgardt, et al., Nucl. Phys.B 229(1988)
7. W. Burtl, et al.Eur. Phys. J.C47 (2006)337
8. A.Czarnecki,W.J.Marciano, and Xavier Gracial Tormo, Phys. Rev.D84(2011)013A.

# Toward a Higgs Factory Muon Collider

Roland P. Johnson<sup>1</sup>, Charles Ankenbrandt<sup>1</sup>, Yaroslav Derbenev<sup>2</sup>,  
 Fanglei Lin<sup>2</sup>, James Maloney<sup>3</sup>, David Neuffer<sup>4</sup>, Vasiliy Morozov<sup>2</sup>,  
 Katsuya Yonehara<sup>4</sup>, Cary Yoshikawa<sup>1</sup>

<sup>1</sup>*MuPlus, Inc. 45 Jonquil Lane, Newport News VA, 23606*

<sup>2</sup>*Thomas Jefferson National Accelerator Facility, 12000 Jefferson Ave., Newport News, VA, 23606*

<sup>3</sup>*Northern Illinois University, 1425 West Lincoln Highway, DeKalb, IL 60115*

<sup>4</sup>*Fermi National Accelerator Laboratory, Batavia, IL 60510*

**Abstract.** Precise measurements of the parameters of the newly discovered Higgs boson candidate are needed to distinguish alternative theories. A muon collider operating near 126 GeV can create the Higgs boson by the s-channel resonance with a cross-section enhanced by a factor of 42,700 compared to an e+e- collider. By using beams with energy spread comparable to the predicted 4 MeV width of the Higgs boson, a muon collider can directly measure the width of the boson independent of theoretical models. This small energy spread centered on the boson mass implies that the event rate will be maximized. New muon beam cooling concepts and devices to achieve 4 MeV energy spread are being developed using analytical calculations, numerical simulations, and experiments, including the construction of a prototype cooling channel segment. A conceptual design of a Higgs Factory Muon Collider is the next step toward the realization of a new kind of machine that can do precision measurements as a lepton machine and has the potential to push the energy frontier beyond the LHC. Parameters for a compelling Higgs Factory are presented along with comments on their technical challenges. The fast track of the CERN proton-antiproton collider started over 30 years ago, that brought us the Z boson, W boson, and then the Top Quark at Fermilab, is a model to be emulated.

**Keywords:** muon collider, Higgs boson, ionization cooling, s-channel resonance,

**PACS:** 13.66.-a, 13.66.Fg, 13.66.Lm

## INTRODUCTION

As a colliding beam particle, the muon offers many advantages to make up for its relatively short 2.2  $\mu$ s lifetime. It is an elementary particle, so that all of its energy is available to create new states of matter such that a muon collider storage-ring can be ten times more effective than that of a hadron collider with the same diameter. It is 206.7 times more massive than an electron and therefore suffers little from electromagnetic radiation effects, which give an advantage over electron-positron colliders in the strength of bending magnets that can be used because of synchrotron radiation or in the initial-state energy resolution because of beamstrahlung.

The muon does not interact by the strong interaction, and its high mass relative to the electron means that it can pass through matter without hadronic or electromagnetic showers. Thus, it is the perfect candidate for ionization cooling [1], in which muons lose energy by passing through a low-Z material and only the longitudinal component is replaced by an RF cavity. This technique allows the angular spread of a beam of muons to be reduced in a very short time close to the limit determined by multiple scattering.

However, this will only work for transverse phase space and the longitudinal dimension requires emittance exchange. Effective longitudinal beam cooling in order to have a small beam energy spread can be the key to making a Higgs factory muon collider.

Precise measurements of the parameters of the newly discovered Higgs boson candidate are needed to distinguish alternative theories [2]. A muon collider operating near 126 GeV can create the candidate Higgs boson by the s-channel resonance with a cross-section enhanced by a factor of 42,700 compared to an e+e- collider. By using beams with energy spread comparable to the predicted 4 MeV width of the Higgs boson, a muon collider can directly measure the width of the boson, independent of theoretical models.

This small energy spread centered on the boson mass is needed to maximize the event rate. Muon beam cooling devices, inspired by analytical calculations and numerical simulations, are being developed, and a prototype of a cooling channel segment is being constructed that will achieve the required 4 MeV energy spread. A conceptual design of a Higgs Factory Muon Collider is the next step toward the realization of a new kind of machine that can do precision measurements as a lepton machine

and has the potential to push the energy frontier beyond the LHC. The fast track of the proton-antiproton collider started at CERN over 30 years ago, that brought us the Z and W bosons, and later the top quark at Fermilab, is a model to be emulated.

## MUON COLLIDER STRATEGIES

Muon beam cooling requirements for an energy-frontier muon collider are different from those of an s-channel Higgs factory muon collider. For the high-energy collider, the best approach is to cool the beams in all dimensions, which allows high-frequency RF acceleration. Then, using emittance exchange as the beams are accelerated, cause the transverse emittance to shrink and the longitudinal emittance to grow up to the point that the RF bunch length at the collision energy is comparable to the  $\beta^*$  of the interaction point, where the luminosity is only slightly affected by the “hour-glass” effect at the IP.

For the s-channel resonance Higgs factory, the essential goal is to concentrate all the total energy of the muon beams at the mass of the Higgs. Well-controlled energy and small energy spread are needed both to maximize the event rate and to allow the Higgs boson mass and width to be measured precisely. The measurement and control of the beam energy can be accomplished by monitoring the precession frequency of the muons in the collider ring [3].

With hydrogen energy absorber using the scheme described below, ionization cooling will leave a 100 MeV/c beam with 2.6% energy spread. This scales to about 4 MeV at 63 GeV, almost the same as the width of the Higgs boson in the simplest model.

Thus, the key to a Higgs-boson Factory muon collider is first to use emittance exchange to cool the longitudinal emittance of each beam to its theoretical minimum and then to preserve that emittance through all transfers and acceleration stages. This preservation is the object of a proposed STTR project.

## HELICAL COOLING CHANNEL (HCC)

In a Helical Cooling Channel (HCC) [4,5,6], a solenoid field is combined with a transverse helical dipole field that provides a constant dispersion along the channel as necessary for the emittance exchange that allows longitudinal cooling. The Hamiltonian that describes motion in this magnetic configuration is easily solved by a transform into the frame of the rotating helical magnet, where it is seen that the addition of a helical quadrupole field provides beam stability over a very large acceptance.

The helical dipole magnet creates an outward radial force due to the longitudinal momentum of the particle

while the solenoid magnet creates an inward radial force due to the transverse momentum of the particle, according to

$$F_{h\text{-dipole}} \approx p_z \times b; \quad b \equiv B_{\perp}; \quad F_{\text{solenoid}} \approx -p_{\perp} \times B; \quad B \equiv B_z$$

In these expressions, B is the field of the solenoid, the axis of which defines the z axis, and b is the field of the transverse helical dipole. By moving to the rotating frame of the helical fields, a time- and z-independent Hamiltonian is used to derive the beam stability and cooling behavior [4]. The motion of particles around the equilibrium orbit is shown schematically in Fig. 1.

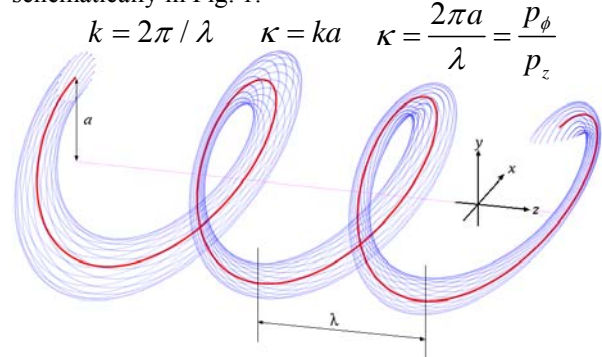


**FIGURE 1:** Schematic of beam motion in a helical cooling channel.

The equilibrium orbit shown in red follows the equation that is the Hamiltonian solution:

$$p(a) = \frac{\sqrt{1+\kappa^2}}{k} \left[ B - \frac{1+\kappa^2}{\kappa} b \right]$$

The dispersion factor  $\hat{D}$  can be expressed in terms of the field components B, b, and the transverse magnetic field radial gradient  $\partial b / \partial a$  on the particle’s orbit:

$$\hat{D} = \frac{p}{a} \frac{da}{dp} = \left( \frac{a}{p} \frac{dp}{da} \right)^{-1}; \quad \hat{D}^{-1} = \frac{\kappa^2 + (1-\kappa^2)q}{1+\kappa^2} + g; \\ g \equiv \frac{-(1+\kappa^2)^{3/2}}{pk^2} \frac{\partial b}{\partial a}$$

where g is the effective field index at the periodic orbit.

The magnetic field ratio on the equilibrium trajectory satisfies the condition

$$\frac{b}{B} = \frac{\kappa}{1+\kappa^2} \left( 1 - \frac{k}{k_c} \right) = \frac{\kappa}{1+\kappa^2} \left( \frac{q}{q+1} \right),$$

$$\text{with } q \equiv \frac{k_c}{k} - 1 \text{ and } k_c = B\sqrt{1+\kappa^2}/p.$$

For stability, the following condition has to be satisfied

$$0 < G \equiv (q-g)\hat{D}^{-1} < R^2 \equiv \frac{1}{4} \left( 1 + \frac{q^2}{1+\kappa^2} \right)^2.$$

Use of a continuous homogeneous absorber (e.g. H<sub>2</sub> gas) takes advantage of the positive dispersion along the entire cooling path, a condition that has been shown to exist for an appropriately designed helical dipole channel. We have also shown that this condition is compatible with stable periodic orbits.

#### G4beamline HCC Simulations

The analytic relationships derived from this analysis were used to guide simulations using a code based on the GEANT4 [7] toolkit called G4beamline [8] and using ICOOL [9], developed at BNL. Simulation results [10] show a 6-D cooling factor of 190,000, where the reference orbit radius is decreased and fields are increased as the beam cools. Results of more recent studies using analytical field expressions [11] show the cooling of longitudinal and transverse emittances at the end of 8 HCC segments that are plotted as red dots in Figure 2. The peak RF field is 27 MV/m, and 60 μm Be windows make the cavities true pillboxes. The gas pressure is 160 atm at 300 K.

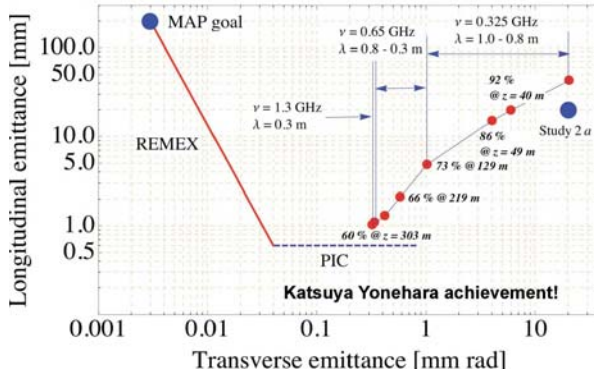


**FIGURE 2:** G4beamline simulation of the emittance evolution along a HCC with three sets of RF frequencies, showing a MAP goal for a high-energy muon collider.

The less effective 1.3 GHz segment in Figure 2 is a limitation for the Higgs Factory Muon Collider since analytic calculations imply that 100 μm should be possible. Smaller, dielectric-loaded 800 MHz cavities may be the solution to this problem.

#### HCC Hardware Component Developments

**Pressurized RF** cavities filled with hydrogen gas have been tested with beam and in magnetic fields in the Mucool Test Area (MTA) at Fermilab. Recent results indicate that ionization electrons can be neutralized fast enough to prevent significant degradation of accelerating gradient by the addition of a small amount of oxygen dopant [12].

**Dielectric loaded RF** cavities allow their smaller diameter to fit inside high field superconducting magnets and their cryostats [13]. Tests in the MTA

will be to demonstrate that breakdown of the dielectric will be suppressed by the pressurized gas.

**Superconducting Helical Solenoid segments** have been made using NbTi and YBCO. A new design based on Nb3Sn conductor is being designed and a four-coil segment is funded to be built next year [5].

An **Engineering design of a prototype 1-m segment** is underway, based on the concept shown in figure 3. Smaller diameter cavities will allow the coaxial waveguides to run parallel to the axis of the segment so they can exit between 1-m long magnet cryostats rather than have to penetrate them as implied by the figure.

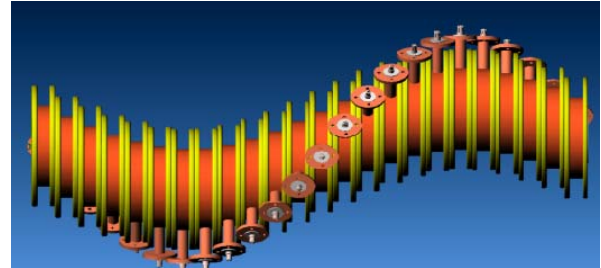


**FIGURE 3:** An STTR project is underway (Muons, Inc. and Fermilab) to design a 1-m long Helical Cooling Channel Segment – complete with a 10 T Superconducting Helical Solenoid magnet (coils in yellow), twenty 805 MHz RF Cavities (copper colored), each dielectric-loaded, pressurized with doped hydrogen gas, and powered by a phase and frequency locked magnetron power source.

## HIGGS FACTORY MUON COLLIDER

**TABLE I – Ultimate Performance Parameters**

Cross section cm <sup>2</sup>	40.0E-36
Higgs/10 <sup>7</sup> s (two detectors)	500,000
<b>Collider Ring</b>	
E (GeV COM)	126
Average dipole field (T)	10
Length of Straight Sections (m)	50
Circumference (m)	232
Revolution frequency (MHz)	1.2934
Number of IPs	2
Number of mu+ bunches	1
bunch intensity	2.5E+12
tune shift parameter	0.016
beta star (cm)	1.0
bunch length (cm)	0.65
Beam energy spread (MeV)	4.12
Norm trans emittance (μm)	200
Norm long emittance (μm) (=0.89eV-s)	100
Peak Luminosity	1.89E+34
mu lifetime (s)	1.30E-03
rep rate (Hz)	60
Average Luminosity	1.26E+33
<b>Proton Driver</b>	
Proton Energy (GeV)	8
mu+ or mu-/sec at 63 GeV	1.5E+14
p/sec	3.17E+15
proton power (MW)	4

Table I shows a set of parameters for a muon collider Higgs factory that could produce over a million Higgs bosons in a real year using two intense bunches of muons cooled to the limits implied by hydrogen energy absorbers. In the table, we assume that each proton produces 0.15 positive and 0.15 negative muons that are captured by a transverse precooling system. Of these captured muons, we estimate 31% survive cooling in the HCC and acceleration to 63 GeV.

Technical challenges to this set of parameters include overcoming limitations to the brightness of the beam due to space charge effects and the effects of RF cavity beam loading. One idea under consideration is that the hydrogen-pressurized HCC will allow compensation of space charge effects.

Another technical challenge is to reduce the costs of the proton driver, cooling channels, and muon accelerators and storage rings. We are addressing these by developing less expensive magnetron power sources, power couplers, and cryostats as well as new concepts for multiturn magnetic return arcs and aberration corrected low beta insertions.

## PBAR-P MOTIVATIONAL EXAMPLE

The CERN pbar-p project [14] started with van der Meer's 1972 stochastic cooling concept [15], confirmed in a 1977 experiment [16]. Nobel prizes were awarded to Rubbia and van der Meer in 1984.

Although the 7-year interval from proof of principle experiment to Nobel Prize is amazing, the analogy between that feat and what could be done to realize a Higgs Factory Muon Collider is worth considering. In the 4 years following the demonstration experiment, CERN turned the Super Proton Synchrotron into a 340 GeV colliding beam storage ring with low beta insertions and new transfer lines. They also designed, built, and commissioned a sophisticated antiproton accumulator ring with several state of the art high frequency RF cooling devices.

Assuming that the project-X proton driver has been built, the Higgs Factory Muon Collider has technological problems to solve that are similar to those that CERN had for the pbar-p collider.

Instead of retrofitting the CERN SPS accelerator to be a 240 GeV storage ring, Fermilab will need to build a relatively small collider ring, which because of superconductivity needs less than a 30 m radius of curvature. Instead of CERN's pbar target, collection system, and accumulator/cooling ring, Fermilab needs a pion/muon production target, collection system and two muon cooling-channels. The acceleration can be much like that developed for a neutrino factory [17].

Most important of all, the s-channel Higgs Factory is on a direct path to an energy-frontier muon collider that would fit on the Fermilab site.

## ACKNOWLEDGMENTS

This work was supported in part by DOE STTR grant DE-SC0007634.

## REFERENCES

1. [benasque.org/2008nufact/talks\\_contr/202Neuffer\\_lecture2.pdf](http://benasque.org/2008nufact/talks_contr/202Neuffer_lecture2.pdf)
2. V. Barger, M.S.Berger, J.F.Gunion, T. Han, s-Channel Higgs Boson Production at a Muon Collider. Phys Rev Lett. 1995 Aug 21;75(8):1462-1465.
3. Calibrating the energy of a 50×50 GeV muon collider using spin precession. Raja, Rajendran; Tollestrup , Alvin. Physical Review D vol. 58 issue 1 July 1, 1998. p. 013005-013005-11
4. Y. Derbenev and R. Johnson, Phys. Rev. ST – Accelerators and Beams 8 (2005) 041002, <http://www.muonsinc.com/reports/PRSTAB-HCCtheory.pdf>
5. V. Kashikhin et al., “Magnets for the MANX Cooling Demonstration Experiment”, MOPAS012, PAC07, Proc. PAC07, Albuquerque, NM, pp. 461-463(2007).
6. S.A. Kahn et al., “Magnet Systems for Helical Muon Cooling Channels”, Proc. PAC07, Albuquerque, NM, pp. 443-445(2007).
7. <http://wwwasd.web.cern.ch/wwwasd/geant4/geant4>
8. T.J. Roberts et al., "G4BL Simulation Program for Matter-dominated Beamlines", Proc. PAC07, Albuquerque, NM, pp. 3468-3470 (2007).
9. R. Fornow, ICOOL, <http://pubweb.bnl.gov/users/fornow/www/icoool/readme.html>
10. K. Yonehara et al., “Simulations of a Gas-Filled Helical Muon Beam Cooling Channel” Proc. PAC2005, Knoxville, TN, pp.3215-3217 (2005).
11. K. Yonehara, R. P. Johnson, M. Neubauer, Y. S. Derbenev, “A helical cooling channel system for muon colliders”, IPAC10, MOPD076 <http://epaper.kek.jp/IPAC10/papers/mopd076.pdf>
12. K. Yonehara et al., BEAM TESTS OF A HIGH PRESSURE GAS-FILLED CAVITY FOR A MUON COLLIDER IPAC12, WEOBA03
13. Milorad Popovic et al., DIELECTRIC LOADED RF CAVITIES FOR MUON FACILITIES, IPAC10.
14. [indico.cern.ch/materialDisplay.py?contribId=3&materialId](http://indico.cern.ch/materialDisplay.py?contribId=3&materialId).
15. S. van der Meer, CERN/ISR/-PO/72-31
16. P. Bramham, L. Thorndahl et al., et al., Stochastic cooling of a stored proton beam, NIM 125, 201 (1975)
17. Bogacz et al. <http://iopscience.iop.org/0954-3899/29/8/338/>

# The CERN to Frejus project: from neutrino beams to MEMPHYS

D. Duchesneau <sup>1</sup>

*LAPP, Université de Savoie, CNRS/IN2P3, F-74941 Annecy-le-Vieux, France*

**Abstract.** MEMPHYS is a proposed 0.5 Mton Water Cherenkov underground experiment to be located under the Fréjus mountain in the Alps. The project is part of the LAGUNA-LBNO european design study which aims at defining future large multipurpose experiments for grand unification, neutrino astrophysics and longbaseline neutrino oscillation studies. The recent measurement of a large theta<sub>13</sub> angle is directly impacting the physics reach of those future projects. Now the priorities can be given to the measurement of the CP violating phase and the mass hierarchy in a large theta<sub>13</sub> scenario. To address efficiently those issues, the MEMPHYS detector is looking at neutrinos from a Super-Beam or a Beta-Beam produced at CERN, at a distance of 130 km. The physics reach and performances of this detector setup with the various neutrino beam options are summarized in this paper.

**Keywords:** neutrino physics, neutrino oscillation, water cherenkov detector, Superbeam, Betabeam

**PACS:** 14.60.Pq, 29.40.Ka, 29.85.Fj

## INTRODUCTION

For the last two decades, neutrino physics has been producing major discoveries including neutrino oscillations. The recent measurements of large theta<sub>13</sub> angle [1] clarify the possible next steps in the exploration of the PMNS neutrino flavour oscillation matrix. It will allow a clear determination of the neutrino mass hierarchy and opens the exciting possibility to measure the CP violation phase. These studies will require accelerator-based intense neutrino beams. Several approaches with various beam and detector technologies are considered in the world through specific design study programs. One of those studies is the CERN to Fréjus project in which a huge water Cherenkov detector called MEMPHYS (MEgaton MAss PHYSics) located in an underground laboratory under the Fréjus mountain in the Alps is able to study low energy neutrinos from two types of beams (Superbeam and Betabeam) produced at CERN, with a baseline of 130 km. In addition to oscillation physics and the study of neutrino properties the MEMPHYS detector will also address astrophysics with solar, atmospheric and supernova neutrino detections and will be able to push limits on nucleon decay search by more than one order of magnitude if not observed. This paper reviews the part concerning the CERN neutrino beam project and the physics performance of the detector based on the latest beam configurations and improved simulations. The potential of the project with the beams was first investigated in [4]. Several changes occurred (detector geom-

etry, oscillation physics knowledge) which require new studies to be performed.

## THE CERN NEUTRINO BEAM OPTIONS

### Superbeam

The CERN Super Beam is a low-energy high-intensity conventional muon neutrino beam (Super-Beam) based on a High Power Super Conducting Linac (HP-SPL) providing a proton beam power of 4 MW with an energy of 4.5 GeV at a repetition rate of 50 Hz.

The neutrino produced by the decays of mesons after the magnetic horn collector have an average energy of 300 MeV after optimisation. This energy allows to be on the first maximum of the atmospheric oscillation at 130 km distance providing an excellent reach for leptonic CP violation with a large water Cherenkov detector.

Beams of neutrinos or anti-neutrinos can be obtained by inverting the horn polarity from positive to negative. This defines the two main oscillation channels which will be studied for the CP phase:  $\nu_\mu \rightarrow \nu_e$  and  $\bar{\nu}_\mu \rightarrow \bar{\nu}_e$ . Figure 1 shows the energy distributions of the various neutrino (left) and antineutrino species produced in the Superbeam using the design optimised in [2].

The current design for the CERN to Frejus neutrino beam based on the SPL has been studied in the framework of the EUROnu design study,

---

<sup>1</sup> on behalf of the MEMPHYS collaboration

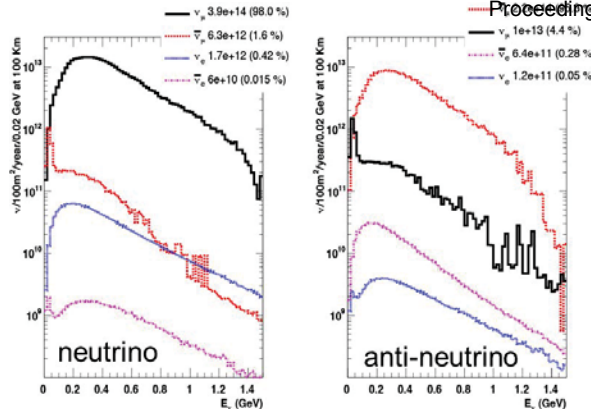


**FIGURE 1.** Neutrino fluxes obtained with the optimized horn and decay tunnel in positive (left) and negative (right) focusing mode.

## Betabeam

The Betabeam concept has been introduced in 2002 [3]. The idea is to produce collimated pure electron neutrinos and anti-neutrinos by accelerating to high energies radioactive isotopes which subsequently decay in a storage ring. The neutrino energy depends on the Q-value of the beta decay and of the relativistic  $\gamma$  boost of the stored isotopes. The CERN Beta Beam facility is based on CERN infrastructure and machines (PS and SPS) and on existing technologies. Two isotope pairs have been selected and studied for  $\bar{\nu}_e \nu_e$  production: one with a low-Q at around 3.3 MeV with  ${}^6\text{He}$  and  ${}^{18}\text{Ne}$  and the other one with high-Q at around 13 MeV with  ${}^8\text{Li}$  and  ${}^8\text{B}$ . The low-Q option with  ${}^6\text{He}$  and  ${}^{18}\text{Ne}$  isotopes is well adapted for neutrino energy (300 MeV) and baseline (130 km) required for the CERN-Fréjus Betabeam. The SPS allows a maximum gamma of 150 for  ${}^6\text{He}$  or 250 for  ${}^{18}\text{Ne}$ . A relativistic  $\gamma$  of 100 has been chosen for both ions after physics optimisation. The estimations have been done assuming rates of  $2.9 \times 10^{18}$  anti-neutrinos/year from  ${}^6\text{He}$  and  $1.1 \times 10^{18}$  neutrinos/year from  ${}^{18}\text{Ne}$  and 5 years run per isotope.

The main parts of the facilities needed for the Betabeam at CERN are shown in Figure 2. The main characteristics of the decay ring are a magnetic field of the main magnet in the ring of 6 T, a circumference of 6900 m and two straight sections with length equals to 2500 m.

The neutrino oscillation appearance channels accessible with the Betabeam are  $\nu_e \rightarrow \nu_\mu$  and  $\bar{\nu}_e \rightarrow \bar{\nu}_\mu$ . The combination of the Super Beam appearance channels with the Beta-Beam ones allow to perform tests of both CP and T symmetries.

In addition the unoscillated neutrinos of one facility can be used to study well the efficiencies of the other one

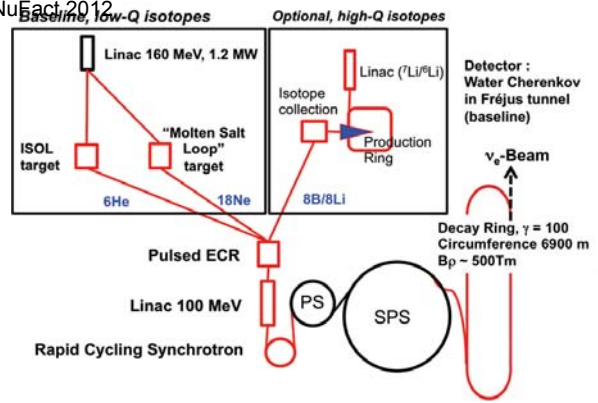


**FIGURE 2.** Layout of the CERN Beta Beam, where the PS and the SPS are existing machines. The baseline scenario is to use  ${}^6\text{He}/{}^{18}\text{Ne}$  (low-Q) with neutrinos to Fréjus

since the neutrino energy distributions of both machines match well.

## THE MEMPHYS DETECTOR

MEMPHYS is a proposed 0.5 Mton Water Cherenkov underground experiment to be located under the Fréjus mountain in the Alps, in the tunnel connecting France to Italy near the existing Modane underground laboratory (LSM) in France. The rock overburden amounts to about 4800 m.w.e. The potential for neutrino physics with specific Super- Beams and Beta-Beams was initially investigated in detail in [4]. The authors assumed the same performance as the Super-Kamiokande (SK) detector [5] in terms of detection efficiency, particle identification capabilities and background rejection. The detector setup was based on 3 cylindrical modules of 65 m in diameter and 60 m in height. However, at the Fréjus site, the quality and the characteristics of the rock allow for a larger excavation in the vertical direction up to 103 m. The new reference design presently envisaged consists of 2 modules of 103 m height and 6.5 m diameter. Taking into account a 1.5 m thick veto volume surrounding the main tank and a cut at 2 m from the inner tank wall for the definition of the fiducial volume, as done in Super-Kamiokande to allow for Cherenkov cone development, the total fiducial mass should correspond to 500 kilotons. Each module is equipped with  $\sim 120\,000$  8" or 10" photomultipliers (PMTs) providing 30% optical coverage (equivalent, in terms of number of collected photoelectrons, to the 40% coverage with 20" PMTs of SK). A schematic view of the detector and of a possible layout for installation at the Fréjus site are shown in Figure 3.

The behaviour of a larger scale detector will, however, be different because of the larger distance travelled

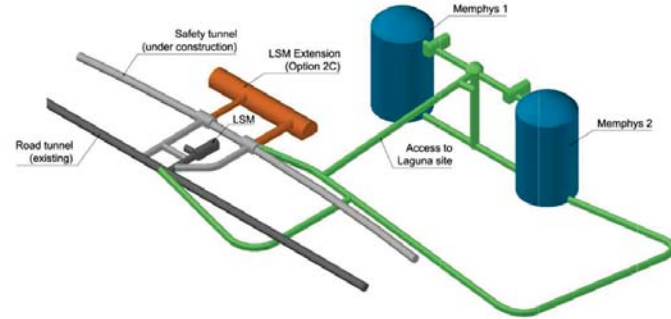
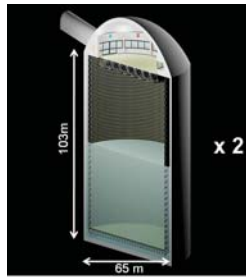


**FIGURE 3.** Schematic view of one MEMPHYS module (left) and design for installation and infrastructure at a possible extension of the LSM underground laboratory at the Fréjus site (right, courtesy of Lombardi). Each tank is 65 m in diameter and 103 m in height.

by light to reach the photomultipliers. New studies have been recently done to reestimate the MEMPHYS detector performance. They use a full detailed Geant-4 simulation developed from a code originally written for the T2K-2km detector project. It allows a detailed detector description, easy to modify, and implements the new layout with two 65x103 m tanks. The neutrino interactions in water are simulated with GENIE [6].

A complete analysis chain has been built, based on what is done in Super-Kamiokande. Some of the algorithms are a simplified version of the SK ones. Their performance was also evaluated by running the full simulation with the SK parameters (size, PMT coverage etc...) to ensure that no significant degradation of efficiencies and background rejection are introduced by the algorithms. The aim of the procedure is the reconstruction of the incoming neutrino energy and the identification of its flavour to perform appearance or disappearance analyses with the different types of beams. This is only relevant for Charged Current (CC) neutrino interactions. Neutral Current (NC) interactions where a final-state pion can mimic an electron or muon are considered separately. The analysis proceeds through five main steps: reconstruction of the interaction vertex from the timing of the hits in the different PMTs; determination of the outgoing lepton direction from the pattern of the Cherenkov ring; lepton identification ( $\mu$  vs  $e$ ), from the "fuzziness" of the Cherenkov ring; rejection of NC interaction with a  $\pi^0$  in the final state from ring counting and reconstruction of the lepton momentum from the charge collected on the PMTs. The incident neutrino energy is then deduced from the measured lepton momentum and direction. Figure 4 shows the reconstructed neutrino momentum for 360 MeV  $\nu_\mu$  and Figure 5 shows the electron momentum resolution as a function of momentum obtained for fully contained (FC) single ring electron produced in  $\nu_e$  interactions. A detailed description of those different algorithms and results are given in Ref [7].

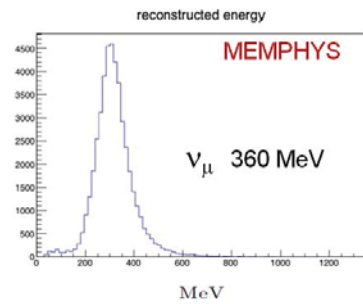


**FIGURE 4.** Reconstructed energy for 360 MeV muons

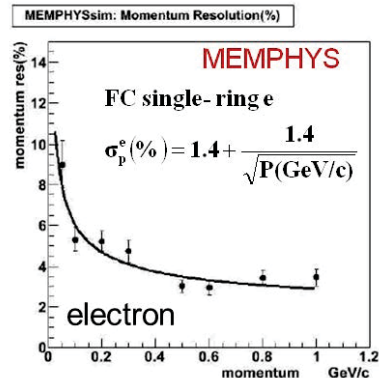


**FIGURE 5.** Momentum resolution for fully contained single ring electron.

In order to take into account the effects of reconstruction in the efficiency evaluation the correlations between reconstructed and true neutrino energy have to be determined. The corresponding Migration Matrices have been computed for the 6 different detection channels used in the  $\nu_\mu$  and  $\nu_e$  selections.

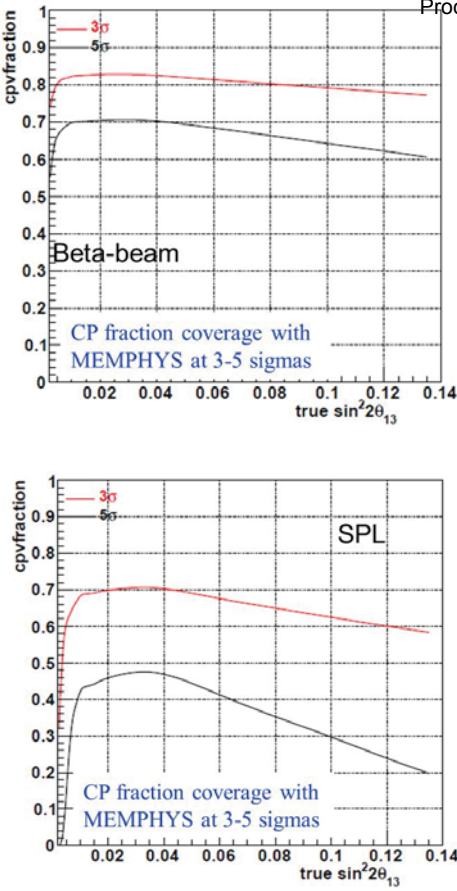


**FIGURE 6.** 3 and  $5\sigma$  sensitivity of the MEMPHYS experiment to the CP phase, assuming normal mass hierarchy with the Betabeam (top) and the Superbeam based on SPL (bottom).

## PHYSICS PERFORMANCE

Applying those migration matrices on the selected and reconstructed neutrinos in MEMPHYS, the study of the sensitivity to the leptonic CP violation has been done.

However the systematic uncertainty knowledge is essential in the large  $\theta_{13}$  scenario where they play an important role in the sensitivity assessment. The systematics assumption made in this study are: 2% on the energy scale calibration (cosmics and  $\pi^0$ ), an additional 10 MeV is accounted for the Superbeam due to the wide band spectrum; 5% on neutrino flux and residual background applying a far/near detector ratio. For  $\nu_e$  appearance, a 5% for each background contribution ( $\pi^0$  1ring, intrinsic  $\nu_e$ , misid. muon) is taken into account. Figure 6 shows the sensitivity to the leptonic CP violation phase,  $\delta_{CP}$ , using the GLOBES package [8] at 3 and  $5\sigma$ , as a function of  $\theta_{13}$  for each beam option. For the Beta-Beam, a running time of 5 years with neutrinos and 5 years with antineutrinos is considered, with a systematic

uncertainty of 2% on both signal and background. For the Super-Beam, a running time of 2 years with neutrinos and 8 years with antineutrinos is considered, with a systematic uncertainty of 5% on signal and 10% on background. Normal mass hierarchy is assumed.

## CONCLUSIONS

The new value of  $\theta_{13}$  motivated to reexamine carefully physics performance for the future neutrino beam projects tuned at first atmospheric oscillation maximum. A detailed study of the performance of the MEMPHYS large scale water Cherenkov detector with a Superbeam and a Betabeam from CERN using a full simulation and realistic analysis algorithms has been recently developed. First potential results using new migration matrices confirm previous expectations. The sensitivity to the the CP violation obtained with the Superbeam to Frejus alone reaches 60% of the CP phases at  $3\sigma$ . When adding the Betabeam, the phase coverage increases to 80%. When adding to these neutrino beam results the potential for detailed neutrino astrophysics and nucleon decay not covered in this paper, the MEMPHYS detector offers an outstanding research program.

## ACKNOWLEDGMENTS

We are grateful to the European Commission for part of the financial support of the presented work through the FP7 Design Studies LAGUNA (Project Number 212343), LAGUNA-LBNO (Project Number 284518) and EUROnu (Project Number 212372).

## REFERENCES

1. T2K collaboration, K. Abe et al., *Phys. Rev. Lett.* **107** (2011) 041801,  
Double Chooz collaboration, Y. Abe et al., *Phys. Rev. Lett.* **108** (2012) 131801,  
Daya Bay collaboration, F.P. An et al., *Phys. Rev. Lett.* **108** (2012) 171803,  
RENO collaboration, J.K. Ahn et al., *Phys. Rev. Lett.* **108** (2012) 191802.
2. A. Longhin, *Eur. Phys. J.* **C71** (2011) 1745.
3. P. Zucchelli, *Phys. Lett.* **B532** (2002) 166.
4. J.E. Campagne et al., *JHEP* **0704** (2007) 003.
5. Super-Kamiokande Collaboration, S. Fukuda, *Nucl. Instrum. Meth.* **A501** (2003) 418.
6. C. Andreopoulos et al., *Nucl. Instrum. Meth.* **A614** (2010) 87.
7. L. Agostino et al., arXiv:1206.6665v2 [hep-ex] (2012).
8. P. Huber, M. Lindner, and W. Winter, *Comput. Phys. Commun.* **167** (2005) 195.

# Status of Target and Magnetic Horn Studies for the CERN to Fréjus Super Beam

N. Vassilopoulos, E. Baussan, E. Bouquerel, M. Dracos, G. Gaudiot, B. Lepers,  
F. Osswald, P. Poussot, J. Wurtz, and V. Zeter  
on behalf of EURONu WP2 group

*IPHC, Université de Strasbourg, CNRS/IN2P3 F-67037, Strasbourg, France*

### **Abstract.**

In the framework of the EUROnu design study, a new design for the CERN to Fréjus neutrino beam based on the SPL is under development by the WP2 group. The main challenge of this project lies with the design of a multi-MW neutrino beam facility. The horn and the decay tunnel parameters have been optimized to maximize any potential discovery. The target design, thermo-mechanical analysis, and power supply design of the horn system as well as any safety issues are being studied to meet the MW power requirements for the proton-beam.

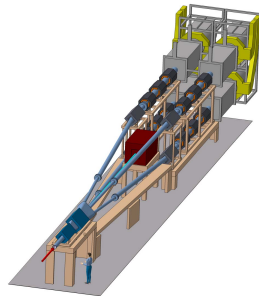


**FIGURE 1.** 4 MW beam into  $4 \times 1$  MW splitting apparatus

## INTRODUCTION

The summary of the recent horn studies for the CERN to Fréjus neutrino beam is presented in this paper. Emphasis is given to the multi-physics simulation to investigate heat transfer, cooling and mechanical stress for the horn, and furthermore for the support module of the four horns. Also, a target design able to withstand a multi-MW proton-beam power, the optimization procedure for the horn shape and layout-geometry to achieve optimum physics, and safety aspects are discussed. The design and the physics reach of the Super Beam project are described in [1].

## THE PROTON-BEAM AND FOUR-HORN/TARGET STATION

A 4-MW proton-beam from CERN's SPL is foreseen to be separated by a series of kicker magnets into four beam

lines. Then each beam will be focused by a series of quadruples and correctors to a four horn/target assembly as shown in Figure 1 [2, 3]. In that way each horn/target assembly is able to accommodate better the multi-MW power and thus increasing its lifetime, the target in particular. The four-horn target system will be placed within a single large helium vessel. The downstream of the neutrino beam-line consists of several collimators, the steal decay tunnel for the mesons to decay and the graphite beam-absorber at the end.

A 0.25 mm thick beryllium beam window has been studied as the interface between each 1 MW proton-beam line and each horn/target assembly in the vessel [1]. Maximum temperatures as high as 180 °C and (109 °C) and Von Mises stresses as high as 50 MPa and (39 MPa) are developed respectively for water and helium cooling: these are well below the beryllium strength limit.

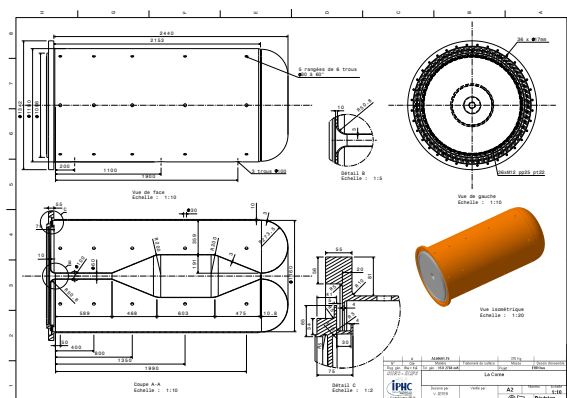


**FIGURE 2.** Horn detailed design

## TARGET STUDIES

A packed-bed target with Ti6Al4V-spheres and helium transverse cooling has been chosen as the baseline target option [1]. It is placed inside the upstream part of horn's inner conductor. The advantages of the packed-bed target are among others a large surface area for heat transfer with coolant able to access areas with highest energy deposition, minimal thermo-mechanical and inertial stresses, and potential heat removal rates at the hundreds kilowatt level with high helium flow rate. Advantages of the helium transverse cooling are an almost beam neutral, no generation of stress wave in coolant and low activation of coolant with no corrosion problems. Because of the small 3-4 mm diameter of each sphere, the gradient of its temperature field is very small resulting in minimal thermal, and inertial dynamic stress.

Alternatively, a pencil-like geometry of solid beryllium has been studied [4]. This pencil-like geometry gives steady-state thermal stress within acceptable range for beryllium. Pressurized helium cooling appears feasible but center proton-beam effects could be problematic because of the stress induced: this point needs further thermo-mechanical studies.

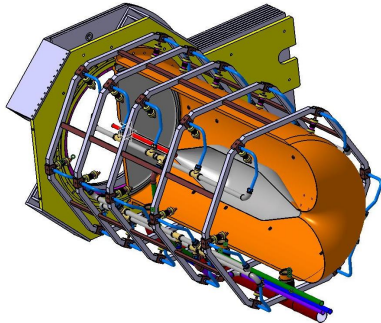


**FIGURE 3.** Horn drawing with cooling system. The target and the inner conductor's shape are shown as well

## HORN STUDIES

### Horn shape and layout-geometry optimization

The end-design consists of an inner conductor with a cylindrically shaped upstream part to decrease the transverse momentum of the low-energy charged mesons, followed by a trapezoidal shaped middle part to select a special particle energy spectrum (for optimum physics) and finally a convex downstream plate to de-focus wrong-sign mesons that contribute to the background neutrino spectra. This configuration has been selected as the best compromise between physics performance and reliabil-

ity under 1 to 1.3 MW proton-beam power [1]. The detailed design and drawing for the horn are shown in Figures 2 and 3.

The horn and the geometrical parameters of the decay tunnel (length and radii) are optimized for the best achievable sensitivity limit on  $\sin^2 2\theta_{13}$ . The beam parameters are initially scanned broadly and then restrictively in three iterations in order to minimize the CP-violation averaged 99% C.L. sensitivity limit on  $\sin^2 2\theta_{13}$  [5, 6].

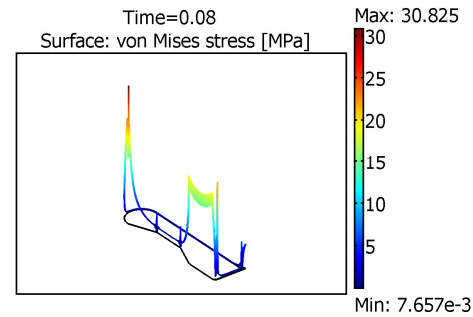


**FIGURE 4.** Horn stress  $s_{max} = 30$  MPa

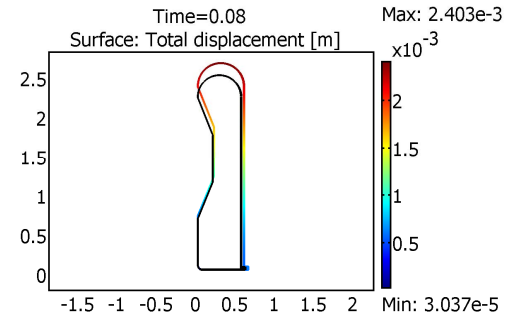


**FIGURE 5.** Horn deformation  $u_{max} = 2.4$  mm

### Horn thermo-mechanical and dynamical stress studies

The Al-6061T6 alloy is the chosen material for the horn because it represents a good trade off between mechanical strength, resistance to corrosion, electrical conductivity and cost. Each horn is subject to a peak 350 kA current at 12.5 Hz frequency. As a result, the aluminum alloy is subjected to cyclic deformation due to a pulsed magnetic pressure load. In addition, the temperature field creates a thermal static stress due to joule effect and secondary particle crossing the conductors. The maximal static thermal stress is calculated about 60 MPa for a non uniform cooling with maximal temperature of 60 °C and is located in the upstream corner and downstream top part of the horn [7]. If a uniform temperature

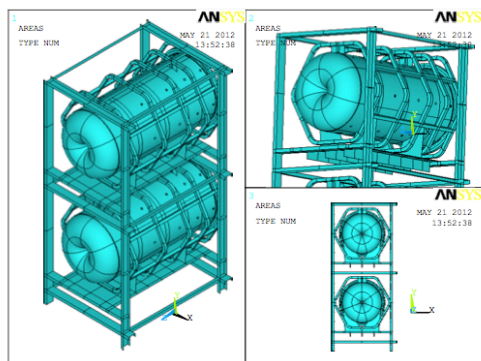
is achieved everywhere, the horn is expanding, and the maximum thermal static stress is 6 MPa. The stress in the upstream part of the inner conductor due to magnetic pulses and thermal expansion is around 20 MPa for a uniform achieved temperature of 60 °C. The stress and the deformation of the horn are shown in Figures 4 and 5, and the detailed studies are written in [7].

## Fatigue

There is no fatigue limit available for Aluminum alloy so the fatigue data can only give a probability of failure for a determined level of stress and number of cycles. According to [8], the fatigue strength limit is 20 MPa for  $10^9$  pulses with a mean static stress due to thermal dilatation. For the weld junction a limit of 10 MPa should be respected to maximize horn lifetime. For the inner conductor horn, the magnetic pressure pulse creates a peak on the von Mises stress value of about 16 MPa. This value is below the 20 MPa limit strength for  $10^8$  cycles and with mean stress due to thermal dilatation [7, 9].

## Cooling system

To remove a total power of about 60 kW and maintain a temperature of about 60 °C a water-jet cooling system is being studied. This system will be made of 5 rows of 6 nozzles (Figure 3) and to spray water toward the inner conductor of the horn. The estimated water flow rate is calculated between 60 to 120 l/min per horn depending on the design. To minimize the thermal static stress, the nozzle size and disposition should be properly located in order to achieve the most uniform temperature everywhere inside the horn [10].



Source: [1]

**FIGURE 6.** Horn support half-frame design

## Four-horn system support

The horns and collimators will be held in place by support modules which can be lowered vertically into the helium vessel by crane. One support module will hold the four horns and the strip-lines, and a second will hold the four collimators. The support modules rest on kinematic mounts at the top of the helium vessel. Removable shield blocks will fit inside the support modules, and rest on the sides of the vessel. The sides of the shield blocks will be stepped to create a labyrinth, preventing direct shine of radiation to the top of the vessel. The support for the four horns (Figure 6) has been designed and a complete static and dynamic analyses have been performed [1].

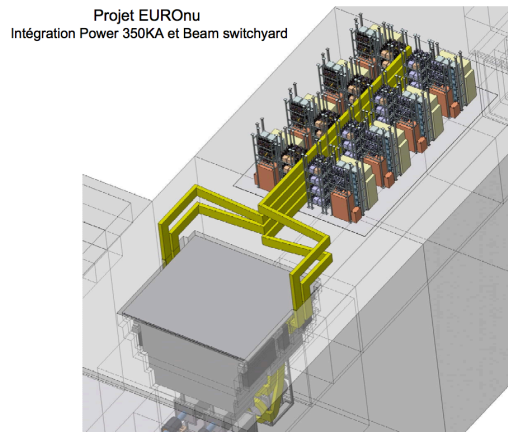


**FIGURE 7.** Power supply modules with strip-lines

## Power supply

A one-half sinusoid current waveform with a 350 kA maximum current and pulse-length of 100  $\mu$ s at 12.5 Hz frequency is needed for each horn. A capacitor charged at +12 kV reference voltage will be discharged through a large switch in a horn via a direct coupled design. A recovery stage allows to invert rapidly the negative voltage of capacitor after the discharge, and to limit the charge capacitor current. In order for the system to be feasible, a modular architecture has been adopted with 8 units: 2 modules are interconnected on a same transmission line based on 2 strip-lines. The recovery energy efficiency of that system is very high at 97 % [11]. Schematics of the power supply apparatus and details of one module are show in Figures 7 and 8 respectively.

## SAFETY

The future design of Multi-Mega Watt sources facility has to take to account the significant amount of radi-

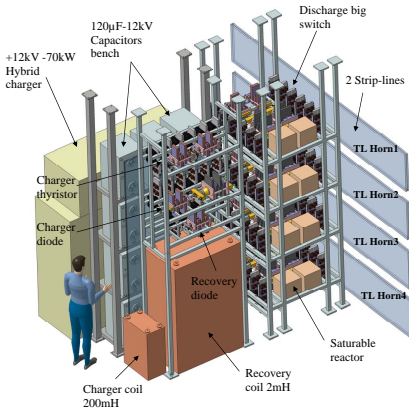


**FIGURE 8.** Schematics of one power supply module

ation produced during beam operation and the radioactivation of the surrounding environment. The design of the shielding should reduce the dose equivalent rate to a minimal level. In order to reach these dosimetry objectives the ALARA (As Low As Reasonably Achievable) approach will be used in the design of the facility. ALARA consists of an iterative process between three phases: a) Preparation, design of the facility, dose equivalent rate map, study the intervention procedures for workers b) execution, engineering phase check/improve the dosimetry objectives and c) analyse and feedback on safety from previous experiments.

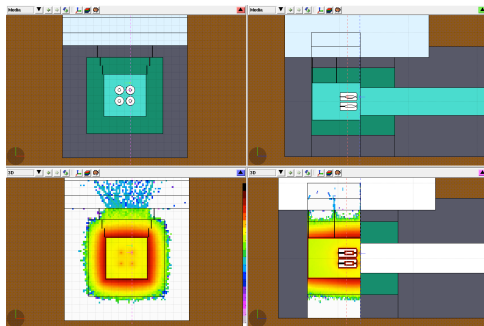


**FIGURE 9.** Power density distribution on the target/horn station (green for iron, grey for concrete, and brown for molasse rock at CERN)

The Super Beam infrastructure consists of: a) Proton Driver line, b) Experimental Hall (Target Station, Decay Tunnel, Beam Dump), c) Spare Area Room, d) Hot Cell, e) Service Galleries (Power supply, Cooling system) f) Air-Ventilation system and g) Waste Area. Energy deposition (Figure 9 for the horn/target station) and activation studies have been performed for that apparatus in order to design the cooling systems and appropriate shielding taking into account ALARA [1, 12].

## CONCLUSION

Monte-Carlo, thermo-mechanical and dynamical stress finite-elements analysis studies show that the four-horn/Target system can be feasible under the extreme 4 MW proton-beam power conditions. Furthermore, R&D is needed for the target and the horn in order to study the fatigue, cooling, power supply designs and radiation degradation.

## ACKNOWLEDGMENTS

We acknowledge the financial support of the European Community under the European Commission Framework Programme 7 Design Study: EURONu, Project Number 212372. The EC is not liable for any use that may be made of the information contained herein.

## REFERENCES

1. E. Baussan et al., *The SPL-based Neutrino Super Beam*, ed M. Zito, 2012, EURONu Design Report, <http://www.euronu.org>, to be submitted to Elsevier
2. E. Bouquerel et al., *Feasibility Study of the Distribution of 4×1 MW Beam Power onto the Horn System*, EURONu Note 17, 2012, <http://www.euronu.org>
3. C. Bobeth et al., *The Proton Driver for the Neutrino Super Beam: Status and Issues*, EURONu-WP2-09-11 Note, 2009, <http://www.euronu.org>
4. C. Densham et al., 3rd EURONu Annual Meeting, 2011, <http://indico.cern.ch/categoryDisplay.py?categId=2493>
5. A. Longin, *A new Design for the CERN-Fréjus Super Beam*, EURONu-WP2-10-04 note, 2010, <http://www.euronu.org>
6. C. Bobeth and A. Longhin, *Optimization of hadron focusing*, EURONu-WP2-10-02, 2010, <http://www.euronu.org>
7. B. Lepers et al., *Horn Studies*, EURONu WP2 Note 13, 2012, <http://www.euronu.org>
8. G. Yahr, *Proc. Conf. on Codes and Standards in a Global Environment (Colorado)*, ed J. Staffiera, 1993, American Society of Mechanical Engineers, pp. 43
9. P. Cupial and M. .S. Koziem, 3rd and 4th EURONu Annual Meetings, 2011 and 2012, <http://indico.cern.ch/categoryDisplay.py?categId=2493>
10. B. Lepers, *Water Jet Cooling System for an Electromagnetic Horn*, EURONu-WP2-10-06 note, 2010, <http://www.euronu.org>
11. P. Poussot, J. Wurtz, and V. Zeter, *Study of 4 Horns 350kA Peak Current, 100 μs large 50 Hz Electric Power Supply Unit with Coupled Direct Devices*, EURONu WP2 Note 15, 2012, <http://www.euronu.org>
12. N. Vassilopoulos et al., *Energy Deposition Studies*, EURONu Note 12, 2012, <http://www.euronu.org>

# Optimizing the neutrino factory capture section

Ole Martin Hansen\* and Ilias Efthymiopoulos†

\*University of Oslo, Oslo, Norway & CERN, Genéve, Switzerland

†CERN, Genéve, Switzerland

**Abstract.** The *capture section* is studied using the simulation tools FLUKA and G4beamline. Protons hit a Hg-target producing charged secondary particles in a region with a high magnetic field. The pions and muons are focused by a tapered magnetic field produced by a series of solenoids. The goal of the study is to improve the capture efficiency, by using alternative magnetic field tapering, solenoid geometry and solenoid shielding.

**Keywords:** Neutrino factory, capture section, solenoid, magnetic field, taper

**PACS:** 41.85.Lc, 13.25.-k

## INTRODUCTION

The Neutrino Factory (NF) will provide intense, high energy neutrino beams from the decay of muons [1]. The majority of the muons will be created from the decay of pions, produced by a proton beam impinging on a Hg-target. It will be important to capture a large fraction of the produced pions, then let them decay to muons and transport them through the NF *front-end* to maximize the particle flux into the accelerator. The NF front-end consists of the target and capture section, a longitudinal drift, a buncher, a rotator and finally a muon cooling section.

In the baseline design the capture section consists of a series of high magnetic field solenoids (see figure 1), making a magnetic field tapered from 20 T to 1.75 T over a distance of 12 m [2]. Charged particles from the target are captured in the 20 T magnetic field to form a beam. The beam's divergence is then gradually decreased by the tapered magnetic field, before it enters the constant 1.75 T field in the drift section. Here pions decay and the particles develop a position and energy correlation. The longitudinal phase space is then manipulated in the buncher and phase rotation section to reduce the beam momentum spread. Finally the transverse phase space is reduced in the cooling section.

The number of pions captured depends on the magnetic field strength, the shape of the tapering and the geometry of the shielding. To maximize the muons flux into the accelerator an optimization study is performed for these key concepts and the results are presented here.

## OPTIMIZATION METHOD

The results presented are produced using G4beamline, a particle tracking program based on Geant4 [3]. A Hg-target is used with length  $l = 30$  cm and radius  $r = 0.5$

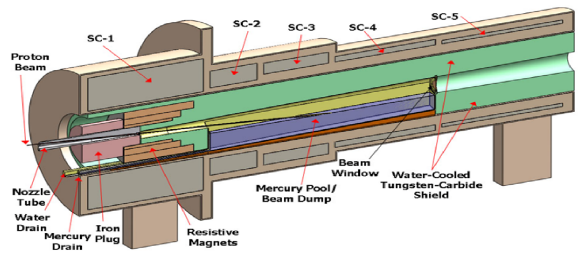


**FIGURE 1.** Baseline layout of the target and capture section of the NF. The proton beam is focused on the Hg-target to produce pions in a 20 T magnetic field made by superconducting solenoid magnets. The pions are then transported downstream towards the front-end [2].

cm. The target center is placed at  $z = -37.5$  cm and tilted an angle  $\theta_T = 96.68$  mrad with respect to the z-axis. The impinging 8 GeV kinetic energy proton beam has an angle  $\theta_{BT} = 30$  mrad with respect to the target axis at the center of the target ( $z = -37.5$  cm). All these parameters are held constant for each setup.

The accelerator can only accelerate a fraction of the muons arriving from the front-end. To find this fraction a setup of the full front-end for G4beamline is used. The muon flux is counted at  $z = 50$  m and at the end of the front-end (at  $z = 271.1$  m). Then the emittance calculation tool *ecalc9f* [4] is applied at the end of the front-end to find the muons accepted for the accelerator, defined as *good muons*. G4beamline labels each of the particles in such a way that the momentum, position and time distribution can be traced back and found at 50 m for these good muons within the *acceptance cuts*. See table 1. This makes it possible to compare different capture systems by the particle flux at 50 m while being confident that the particles within the cuts have a high probability of being good muons. The results are compared with the capture section from Study 2A (ST2a) [2].

**TABLE 1.** Acceptance cuts at 50 m and the input parameter for the ecalc9f routine at 271.1 m. The acceptance cuts were found by using the survivors from the ecalc9f routine and finding their momentum, time and position distributions at 50 m.

Position (m)	$p_z$ (MeV/c)	$p_T$ (MeV/c)	$t$ (ns)	$r$ (mm)
50	100-300	< 50	160-240	< 200
Position (m)	$p_z$ (MeV/c)	$A_T$ (m rad)	$A_L$ (m rad)	Input for ecalc9f
271.1	100-300	< 0.030	< 0.150	

## Optimization without magnet shielding

First the magnetic field tapering for 5 different setups is studied, all without any magnet shielding. There is one variant of *13sol*, three variants of the *3sol* setup that is compared with the *ST2a* setup. The *3sol* layout, figure 2, has 3 superconducting (SC)solenoid magnets. The large SC1 magnet will generate the high 20 T field with help from the normal resistive inner solenoids and SC3 generates a 1.5 T field. The SC2 generate fields that can be read from figure 3. The *13sol* setup has 13 SC

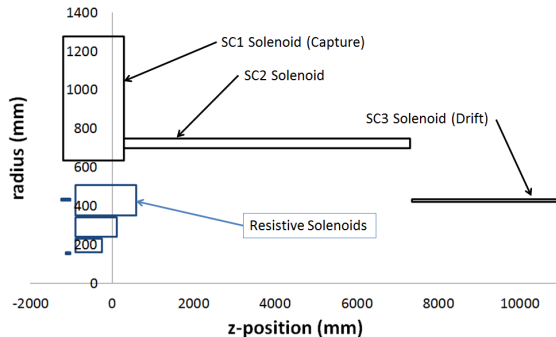


**FIGURE 2.** The *3sol* solenoid magnet setup. The picture shows the upper half of a vertical cut of the solenoids. The black boxes are the superconducting solenoids and the blue boxes are the resistive solenoids. Here we have no magnet shielding.

solenoids and a long field tapering. The magnetic fields on axis can be seen in figure 3. The simulation stoped tracking any particle that hits the solenoids.

The results can be seen in figure 4. The *3sol\_1* setup ( $28513 \mu^\pm$ ) has the highest muon flux, an increase of 9% compared with the *ST2a* ( $26262 \mu^\pm$ ).

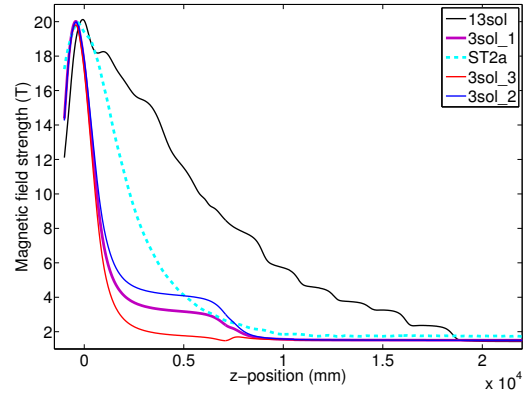


**FIGURE 3.** Magnetic field tapering for all the setups. The *3sol\_1* setup is the thick purple line and the *ST2a* setup is the thick cyan dashed line.

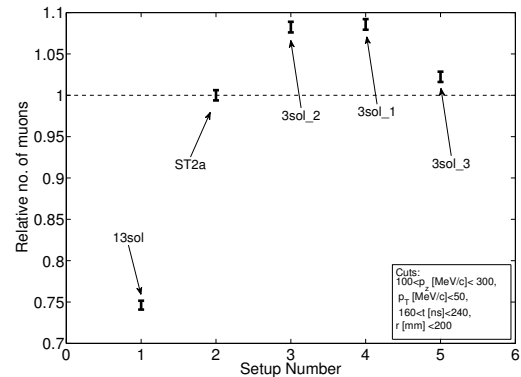


**FIGURE 4.** Relatice muon flux at 50 m, see figure 3. The *3sol\_1* setup give the highest muon flux.

## Optimization with magnet shielding

Shielding is needed to protect the magnets from radiation, the radius of the shielding is found as follows. The inner radius of the magnet shielding is calculated assuming an adiabatic tapering and conservation of magnetic flux  $\Phi = \pi B R^2$ . Where  $B$  and  $R$  are the magnetic field strength and the inner shielding radius, respectively. From flux conservation

$$\pi B_1 R_1^2 = \pi B_2 R_2^2, \quad (1)$$

where the subscripts refer to different points along the tapering where the flux is conserved. This helps to calculate the inner shielding radius as a function of position along the z-axis, taking account of the field taper. The inner shielding radius in the 20 T field region around the target. Using equation 1, with  $B_1 = 20T$ ,  $R_1 = 7.5\text{ cm}$ ,  $B_2^{ST2a} = 1.75\text{ T}$  and

$B_2^{3sol} = 1.5$  T, the radii are found to be  $R_2^{ST2a} = 25.4$  cm and  $R_2^{3sol} = 27.4$  cm. In figure 5 there is the two different

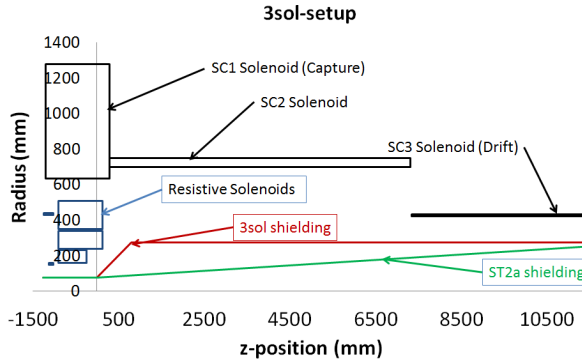


**FIGURE 5.** The 3sol solenoid magnet setup. The picture shows the upper half of a vertical cut of the solenoids. The black boxes are the superconducting solenoids and the blue boxes are the resistive solenoids. The shielding used in the ST2a is showed in green and the 3sol shielding is in red.

magnet shieldings, naming the new shielding made for the 3sol setup for *shielding3*. The shielding for SC1 is not changed, but for SC2 a quickly expanding shielding cone is preferred since the field tapering is shorter. With less shielding the magnet will be more exposed to radiation. Assuming that a low field SC2 magnet can have an increased inner radius the radiation exposure can be decreased.

#### Varying the SC1 magnet strength

The optimisation of the SC1 magnet strength was studied by varying the strength of the SC1 magnet from 10 T to 40 T while observing the muon flux. During this study the SC2 and SC3 magnetic field strengths are held constant at 1.5 T and the 3sol setup and shielding are used. The ST2a muon flux is used as normalization and the relative number of muons is shown in figure 6. Errorbars are statistical only, calculated as the square-root of the muon flux.

The muon flux graph flattens out around 25 T. We choose to set a maximum for SC1 at 20 T, taking into account the technical challenges of making a magnet producing a field higher than 20 T and the increased cost. The relative difference in muon flux between 20 and 25 T is 13%.

#### Varying the SC3 magnet strength

The magnet strength of SC2 is set equal to SC3, the magnet strength of SC3 (and therefore SC2) is then varied from 1 to 2.5 T. SC1 is at 20 T. Again we use

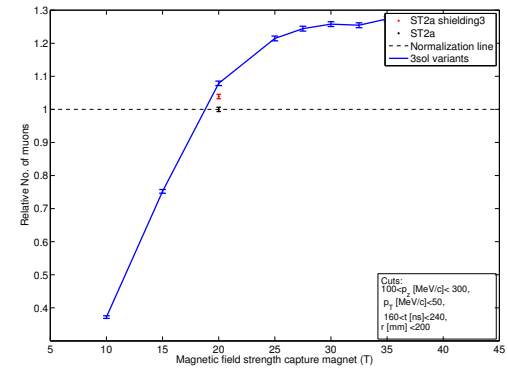


**FIGURE 6.** Relative muon flux at 50 m when varying the SC1 magnet strength from 10 to 40 T are shown in blue, normalized with the muon flux from the ST2a (shown in black). The red point is the ST2a setup with the 3sol shielding. All points include errorbars.

the ST2a muon flux as the normalization(see figure 7). The SC3 magnet should create a field of 1.5 T.

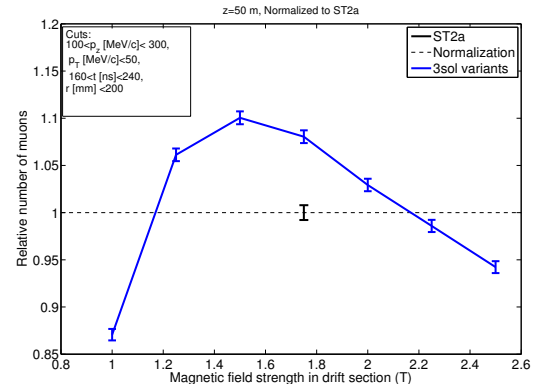


**FIGURE 7.** Relative muon fluxes when varying the SC3 magnet strength from 1 to 2.5 T are shown in blue, normalized with the muon flux from the ST2a (shown in black). Errorbars are statistical.

#### Varying the SC2 magnet strength

SC1 is set to 20 T and SC3 to 1.5 T and the magnet strength of SC2 is varied from 1.75 to 9 T. In figure 8, the results are normalized with the ST2a muon flux. The maximum is found when SC2 is at 4.8 T with an increase in particle flux of about 10 %. Going down to an even lower field is possible without a huge particle loss.

The momentum distributions for the ST2a and the 3sol, both with shielding3, are compared in figure 9. They are similar, with the 3sol having a slight advantage over the ST2a.

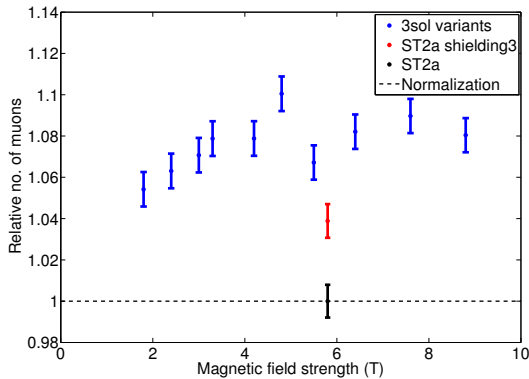


**FIGURE 8.** Relative muon flux when varying the SC2 magnet strength from 1.75-9 T are shown in blue, normalized with the muon flux from the ST2a (shown in black). The ST2a with shielding3 shown in red. Errorbars are statistical only.

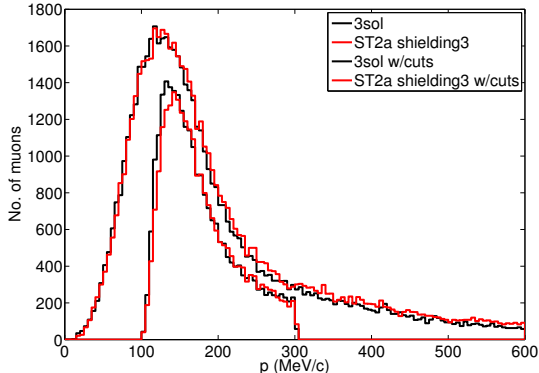


**FIGURE 9.** Muon momentum distribution for the ST2a and the 3sol setups shown in red and black, respectively. We can see that the distributions are similar and the 3sol captures a higher number of muons. The two upper lines show the momentum distribution without any cuts applied while the two lower lines show the distribution with the acceptance cuts.

A study with FLUKA is done in order to compare the results with G4beamline. Table 2 shows some comparisons between the two monte-carlo simulation tools.

**TABLE 2.** Relative no. of total muons and the relative no. of muons within the acceptance cuts for the ST2a and the 3sol. Both have shielding3.

Setup	No cuts		w/cuts	
	G4BL	FLUKA	G4BL	FLUKA
ST2a shielding3	1.09	1.57	1.04	1.24
3sol	1.05	1.38	1.10	1.14

According to the G4beamline simulations, the 3sol setup is better than both the ST2a and the ST2a-shielding3. The results from FLUKA suggests that the

3sol is better than the ST2a and the ST2a-shielding3 is even better than the 3sol. However, reducing the shielding thinkness for the ST2a magnet layout may cause an increase in the radiation exposure to the magnets. For the 3sol the increased inner magnet radius means there can be more shielding between the beampipe and the magnets. FLUKA seems to be more sensitive to a change in shielding layout than G4beamline, increasing the muon flux with 24 % for the ST2a-shielding3.

## Summary and outlook

The magnetic field tapering and the shielding layout for the Neutrino factory was studied. The study of the magnetic field tapering without any shielding, showed that a faster magnetic field tapering is a good alternative to the longer adiabatic tapering. The lower current in SC2 may allow this solenoid, expected to receive the peak of the radiation from the target, to have a larger radius thereby exposing it to less radiation.

When the magnetic field in SC3 is decreased, an increased shielding radius is needed to conserve the magnetic flux. A shortening of the magnetic field tapering, an increase of the shielding inner radius and a shortening of the cone length was done. Then the field strength was optimized in each of the three SC magnets, but varying the field in 1 magnet at a time. This altenative 3sol setup gives a higher yield compared to the ST2a setup, for both FLUKA and G4beamline.

A study of the energy deposition in the magnets to check if the magnets are properly shielded with the new shielding3 is needed. A study with the 30 cm mercury target replaced by, the baseline, full liquid mercury jet target included is needed.

## ACKNOWLEDGMENTS

We would like to thank all the people working with us in the EN/MEF-LE group at CERN, and to send a big thank you to Pavel Snopok for providing us with the G4beamline files of the Neutrino Factory front-end.

## REFERENCES

1. S. Choubey, et al. (2011), bNL-96453-2011, CERN-ATS-2011-216, FERMILAB-PUB-11-581-APC, RAL-TR-2011-018.
2. R. Fernow, et al. (2004), mUC-NOTE-COOL THEORY-296.
3. G4beamline, G4beamline web site (2012), URL <http://www.muonsinc.com/muons3/G4beamline>.
4. R. Fernow (2003), mUC-NOTE-COOL THEORY-280.

# Opportunities for Leptonic CP Violation and Neutrino Mass Hierarchy at Medium Baselines<sup>1</sup>

S. Dusini\*, A. Longhin<sup>†</sup>, M. Mezzetto\*, L. Patrizii\*\*, M. Sioli<sup>‡, \*\*</sup>, G. Sirri\*\* and F. Terranova<sup>§, ¶</sup>

\*Istituto Nazionale di Fisica Nucleare, Sez. di Padova, Padova, Italy

<sup>†</sup>Laboratori Nazionali di Frascati dell'INFN, Frascati (Rome), Italy

\*\*Istituto Nazionale di Fisica Nucleare, Sez. di Bologna, Bologna, Italy

<sup>‡</sup>Dep. of Physics, Univ. di Bologna, Bologna, Italy

<sup>§</sup>Dep. of Physics, Univ. di Milano-Bicocca, Milano, Italy

<sup>¶</sup>Istituto Nazionale di Fisica Nucleare, Sez. di Milano-Bicocca, Milano, Italy

**Abstract.** A large value of  $\theta_{13}$ , as recently observed by reactor and accelerator experiments, is a major opportunity for precision neutrino physics. In this paper we discuss implications for Superbeams at medium baselines. In particular, we emphasize the impact on the determination of mass hierarchy for experiments that exploit matter effects. We demonstrate that unlike mass hierarchy, the measurement of the CP phase remains a major experimental challenge: the study of CP violation in the leptonic sector will require MW class proton drivers even with massive far detectors in the  $\mathcal{O}(1000 \text{ km})$  baseline range.

**Keywords:** Superbeams, leptonic CP violation

**PACS:** 14.60.Pq; 14.60.Lm

## SUPERBEAMS AT LARGE $\theta_{13}$

In 2012 we finally achieved precise information on the size of the mixing angle between the first and third neutrino family ( $\theta_{13}$ ) [1, 2, 3, 4]. The  $\theta_{13}$  value is definitely large - indeed, very close to previous limits set by CHOOZ and Palo Verde. This discovery is going to reshape the experimental strategy to perform precision physics in the neutrino sector and encourage the development of a novel generation of Superbeam experiments to study CP violation and determine the neutrino mass pattern (“mass hierarchy”). The experimental proposals will take advantage of the large  $\nu_\mu \rightarrow \nu_e$  oscillation probability due to  $\theta_{13} = 8.9^\circ \pm 0.4^\circ$  [5], likely relieving the constraints on the detector mass and accelerator power.

Still, a few key issues need to be properly investigated:

- is it true that a large value of  $\theta_{13}$  ease substantially both the determination of the mass pattern and the search for CP violation in neutrino oscillations?
- in the framework of the Superbeams, do we still need MW-class proton drivers or present facilities can be adapted to reach the above-mentioned physics goals?
- should R&D and funding efforts be focused on the increase of the power for proton drivers or the sensitivities will be dominated by the detector system?

atics and feasible fiducial masses?

- is an “all-in-one” Superbeam facility conceivable both for mass hierarchy and for CP violation?

In order to address these issues, we reconsidered a general Superbeam configuration as a function of the baseline. Unlike other studies performed in the past, the beam-line was optimized employing as figure of merit the sensitivity to  $\theta_{13}$  for each source-to-detector distance in the 730-2300 km range; we hence avoided the use of intermediate observables as, for instance, the rate of unoscillated neutrinos. The most important beam-line parameters are the distances among the target, the upstream focusing horn and the downstream focusing horn (i.e. the “reflector”), the target length and the length and width of the decay tunnel. Similarly, we considered the possibility of re-optimizing existing facilities: we used as benchmark the SPS accelerator, which is currently operated as a sub-MW proton driver for the CNGS beam.

The far detector technology considered in this study is the Liquid Argon TPC. In  $\nu_e$  appearance this technology exhibits very high efficiencies both for quasi-elastic (80%) and deep-inelastic (90%) interactions combined with high NC rejection power. In the study presented at NuFact 2012 and deepened in [6] a contamination of NC due to  $\pi \rightarrow e$  misidentification not exceeding 0.1% of the  $\nu_\mu$  CC rate was considered. For quasi-elastic interaction, the neutrino energy can be fully reconstructed by the lepton energy and direction, since the direction of the incoming neutrino is known in advance. Liquid

---

<sup>1</sup> Presented by F. Terranova

Argon detectors are able to reconstruct  $E_\nu$  with a resolution mostly dominated by the electron energy resolution:  $\sigma_{E_\nu}/E_\nu \simeq 0.05/\sqrt{E_\nu}$ ,  $E_\nu$  being expressed in GeV. On the other hand, the energy resolution for deep inelastic  $\nu_e$  interactions is driven by the resolution on the hadronic system. In liquid argon TPC's, it amounts to  $\sigma_{E_h}/E_h \simeq 0.2/\sqrt{E_h(\text{GeV})}$ . In this study, the energy resolution and efficiency for  $\nu_e$  and  $\bar{\nu}_e$  were implemented smearing the final state momenta of the electrons and hadrons. Interactions were simulated using the GENIE Monte Carlo generator [7] and the corresponding migration matrices were implemented in the detector description of GLoBES. The smearing matrices were calculated for  $\nu_e$  and  $\bar{\nu}_e$  separately.

## RESULTS

The analysis described above have shown that a clear determination of the mass hierarchy can be easily achieved by long-baseline Superbeams ( $L > 1500$  km), where the  $\nu_\mu \rightarrow \nu_e$  transition probability is matter dominated. This enhancement of sensitivity directly results from the perturbative expansion of

$$P(\nu_\mu \rightarrow \nu_e) \simeq O_1 + O_2(\delta) + O_3(\delta) + O_4$$

where the large size of  $\theta_{13}$  enhances the CP-blind  $O_1$  term (for a definition of the  $O_i$  terms see [8]).  $O_1$  contains information on the mass pattern through the sign of  $\hat{A} \equiv 2\sqrt{2}G_F n_e E / \Delta m_{31}^2$ ,  $G_F$  being the Fermi coupling constant and  $n_e$  the electron density in matter. The change in  $O_1$  due to the mass pattern is therefore clearly visible even at moderate exposures. This is not the case for facilities at  $L=730$  km (CERN to LNGS), where a unique determination of mass hierarchy for any value of  $\delta$  can be achieved only with exposures  $\sim 1 \text{ MW} \times \text{Mton} \times 10^7 \text{ s}$  (see Fig. 1).

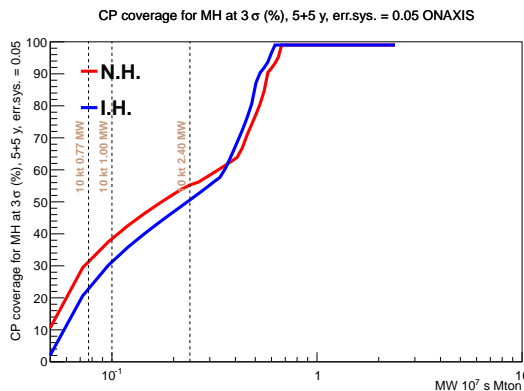


**FIGURE 1.** Mass hierarchy coverage for a 50 GeV on-axis facility at  $L=730$  km as a function of exposure.

The situation is quite different for CP violation, where the  $O_1$  term is in fact a nuisance parameter. Here, a major deterioration of sensitivity is expected if the mass pattern is unknown (“sign ambiguity”) and any realistic configuration that exploits existing facilities (in Europe, the SPS and/or the underground halls of LNGS) cannot exceed CP coverages of  $\simeq 50\%$  (see the vertical bands of Fig. 2). In addition, there is no advantage in working in off-axis mode since a wide spectral band is rewarding to extract  $\delta$  and disentangle the size of  $O_2$  against  $O_1$ . A high power on-axis detector with  $L>700$  km is appropriate to address CP violation provided that its integral exposure is greater than  $2 \text{ MW} \times \text{Mton} \times y_{eff}$ , where  $y_{eff} \simeq 10^7$  s is the running time corrected for the typical duty cycle of the machine. For larger exposure, the CP coverage is systematics limited and it amounts to 70% for a 5% overall systematic error. Fig. 3 shows the CP coverage for an on-axis (ONA) facility based on a MW-class proton driver with a far detector located at 730 and 2290 km (CERN to LNGS and CERN to Phyasalmi, respectively) as a function of the exposure. “NH known” versus “NH unknown” signals the loss of sensitivity due to the missing knowledge of the mass hierarchy. Here we assumed normal hierarchy (NH) as the true one. Very similar results are obtained considering the inverted hierarchy (IH) as the true mass pattern.

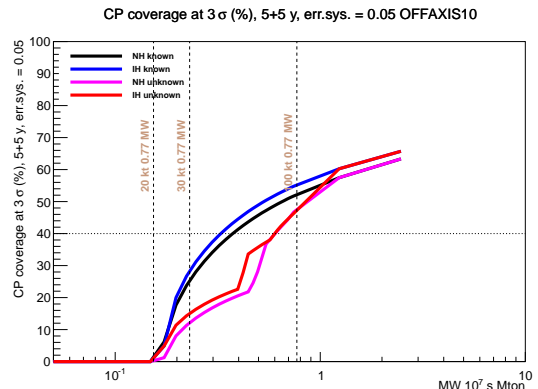


**FIGURE 2.** CP coverage at  $3\sigma$  level for 5 years of  $\nu$  and 5 years of  $\bar{\nu}$  running with the off-axis 10 km configuration at  $L=730$  km, a 400 GeV proton driver and a systematic error on flux normalization of 5%. We consider normal and inverted hierarchy assuming this information to be available or not (color codes).

## CONCLUSIONS

The study performed above suggests a few guidelines that should be considered when designing a new generation of Superbeams, given the unexpected large size

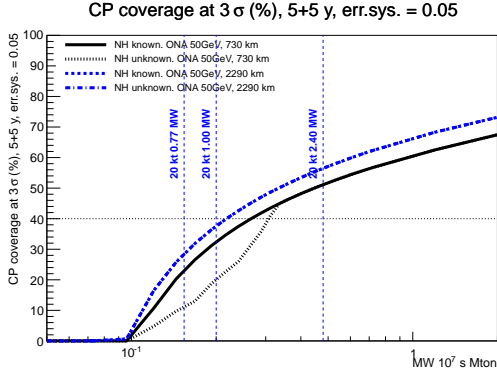


**FIGURE 3.** CP coverage at  $3\sigma$  level for 5 years of  $\nu$  and 5 years of  $\bar{\nu}$  running with the on-axis configuration (ONA), a 50 GeV proton driver, a far detector at  $L=730$ , 2290 km and a systematic error on flux normalization of 5%. We consider normal and inverted hierarchy assuming this information to be available or not (color codes).

of  $\theta_{13}$ . These guidelines answer most of the questions raised in the Introduction.

- A large value of  $\theta_{13}$  eases substantially the determination of the mass hierarchy. Even existing facilities (NOvA) have reasonable chances to establish the sign of  $\Delta m_{31}^2$  and a new facility at long baseline can achieve  $> 5\sigma$  discovery reach for any value of  $\delta$  [9]. Due to the dominance of the  $O_1$  term, however, the study of CP violation will require major upgrades of the Superbeams.
- No existing facility can be adapted to establish CP violation in the leptonic sector with a coverage larger than  $\simeq 50\%$ . Superbeams, however, are the technology of choice for coverages in the 70% ballpark provided a MW-class proton driver becomes available.
- Superbeams are statistically limited for exposures smaller than  $2 \text{ MW} \times \text{Mton} \times y_{eff}$ . Beyond this value, in order to exceed the 70% coverage limit an R&D effort should be carried out to lower systematics below 5% (in a way similar to what has been done in the last decade for reactor experiments).
- Superbeam configurations that tackle simultaneously both the mass hierarchy and the determination of the CP phase can be envisaged even at baselines  $\simeq 730$  km. The exposure, however, must significantly exceed  $O(1) \text{ MW} \times \text{Mton} \times y_{eff}$ .

## REFERENCES

- F. P. An *et al.* [DAYA-BAY Collaboration], Phys. Rev. Lett. **108** (2012) 171803
- J. K. Ahn *et al.* [RENO Collaboration], Phys. Rev. Lett. **108** (2012) 191802
- M. Ishitsuka for the Double Chooz Collaboration, Talk at Neutrino 2012, Kyoto, 6-9 June 2012, available at <http://neu2012.kek.jp>.
- K. Abe *et al.* [T2K Collaboration], Phys. Rev. Lett. **107** (2011) 041801; K. Sakashita for the T2K Collaboration, Talk at ICHEP 2012, Melbourne, 4-11 July 2012, available at [www.ichep2012.com.au](http://www.ichep2012.com.au)
- G. L. Fogli, E. Lisi, A. Marrone, D. Montanino, A. Palazzo and A. M. Rotunno, Phys. Rev. D **86** (2012) 013012
- S. Dusini, A. Longhin, M. Mezzetto, L. Patrizii, M. Sioli, G. Sirri and F. Terranova, arXiv:1209.5010 [hep-ph].
- C. Andreopoulos, A. Bell, D. Bhattacharya, F. Cavanna, J. Dobson, S. Dytman, H. Gallagher and P. Guzowski *et al.*, Nucl. Instrum. Meth. A **614** (2010) 87
- A. Cervera *et al.*, Nucl. Phys. **B579** (2000) 17, erratum *ibid.* Nucl. Phys. **B593** (2001) 731; M. Freund, Phys. Rev. **D64** (2001) 053003.
- A. Rubbia, Talk at Neutrino 2012, Kyoto, 6-9 June 2012, available at <http://neu2012.kek.jp>.

# Design of an efficient cooling lattice for a Neutrino Factory

Diktys Stratakis

*Brookhaven National Laboratory, Upton, NY 11973, USA*

**Abstract.** A Neutrino Factory employs muons which are produced, collected, accelerated and then stored so that their eventual decay produces an intense neutrino beam. A key challenge is that the initial muon beam occupies a region in phase space that vastly exceeds the acceptance of the downstream accelerators. We show that a set of properly tuned rf cavities can reduce the emittance by a factor of three by first forming the muon beams into strings of bunches and then align them to nearly equal central energies. The sensitivity in performance of our proposed channel against key parameters such the number of cavities, accelerating gradient and magnetic field is analyzed. Finally, the lattice tolerance to positioning errors of various lattice components is systematically examined.

**Keywords:** muon accelerators, beam transport, Neutrino Factory, ionization cooling  
**PACS:** 41.75.Fr, 41.85.Ja, 29.27.-a, 41.75.Lx

## INTRODUCTION

Over the past years there have been numerous developments on concepts and technologies for producing, capturing and accelerating a muon beam. Such progress has opened the gates for the construction of a Neutrino Factory in which high-energy muons decay within the straight sections of a storage ring to produce a beam of neutrinos and antineutrinos. Such Neutrino Factory would deliver unparalleled performance in studying neutrino mixing and would provide tremendous sensitivity to new physics in the neutrino sector.

A number of detailed Neutrino Factory designs have been completed [1, 2]. In those designs, 5-15 GeV bunches of protons are focused onto a target to produce pions that decay into muons, which are then accelerated to energies up to a few tens of GeV. The muons are subsequently stored in a racetrack-shaped storage ring, where their decays provide intense beams of neutrinos. A key requirement in maximizing the final flux of neutrinos is that the phase space-volume of the new “born” muon beam must match the acceptance of the downstream accelerators. This demands a front-end channel for manipulating the beam in transverse and longitudinal phase-space before it enters the accelerator channel.

It is important to emphasize that the previously designed front-end lattices use a constant magnetic field over the 70 m long buncher and rotator section. Furthermore, they assume a continuously decreasing frequency where each cavity is different. Finally, a systematic study of the choice and thickness of the absorber in order to achieve successful cooling is far from complete. Therefore, although the existing scheme is suitable for either Neutrino Factory or a

Muon collider, in order to assess its performance and cost it must be studied under more realistic assumptions that correspond to a practical implementation.

Main aim of this work is to develop a realistic baseline design and optimize it for an engineering, performance and cost study. There are several steps needed for this and this work attempts to address the above issues. We first replace the continuous magnetic fields with a more realistic coil geometry. Next, we use groups of discrete rf cavity frequencies rather a continuously decreasing frequency. Then, we examine the sensitivity on cooling by systematically varying the thickness of the absorber. Finally, we suggest key optimizations on the rf gradient and phase in order to maximize the accepted muons.

## NEUTRINO FACTORY BASELINE

In the remainder of this paper we describe the Neutrino Factory front-end and discuss its expected performance. Detailed studies on a Neutrino Factory front-end design have been ongoing for the past few years. Recently, the International Design Study for a Neutrino Factory (IDS-NF) proposed a baseline machine configuration. Using this baseline, the parameters of the Neutrino Factory are being developed to deliver  $\sim 10^{21}$  muons decays per operational year of  $10^7$  secs with which to precisely measure neutrino oscillations. Based on the IDS-NF recommendations, the channel will lower the rms transverse emittance by a factor of  $\sim 3$ . The accepted muons per proton, will rise by a factor of  $\sim 9$  within a transverse normalized acceptance,  $A_T$  less than 0.03 m and a longitudinal acceptance, less than 0.15 m. The chosen acceptance criteria approximate the expected

acceptance of the downstream acceleration and storage rings.

In this configuration, a 4 MW proton driver produces bunches with length in the range of 1-3 ns and 8 GeV in energy. The beam is directed onto a Hg jet target enclosed in a 20 T solenoid. The pions created are captured as they transverse a ~15 m long, tapered superconducting solenoidal magnet system, where the field profile drops adiabatically from 20 T to 1.5 T. Simultaneously, the radius of the beam pipe increases from 7.5 cm at the target up to ~30 cm at the end of the taper. This is followed by a 70 m drift section with a constant 1.5 T field, where the pions decay into muons, and the beam develops a time-energy correlation with a high-energy “head” and a low-energy “tail”.

The decay channel is followed by a 33 m buncher section in which the gradient of the rf system gradually increases and the beam is captured into a string of bunches with different energies. The rf frequency decreases along the length of the buncher, with the constraint that the phase difference between two reference particle momenta,  $p_1$  and  $p_2$ , remains a fixed number  $N_B$  of wavelengths as the beam propagates through it, i.e.,

$$N_B \lambda_{rf}(z) = z \left( \frac{1}{\beta_2} - \frac{1}{\beta_1} \right), \quad (1)$$

where  $\beta_1$  and  $\beta_2$  are the velocities of the reference particles at momentum  $p_1$  and  $p_2$ . Following this procedure, the reference particles and all intermediate bunch centers remain at zero crossings of the rf wave throughout the buncher. For the present IDS-NF baseline design [3], the two reference momenta are 233 MeV/c and 154 MeV/c while the bunch number is equal to 10. With these parameters, the rf frequency at the beginning of the buncher section is 319.6 MHz and at the end falls to 233.6 MHz. In the bunching system, 44 normal-conducting rf cavities are employed, each having a different frequency and the rf gradient increases linearly by up to 9 MV/m.

In the baseline configuration, the pillbox shaped rf cavities have nominal lengths of 0.5 m and are separated by a 0.25 m spacing. To keep the muon beam focused, a constant 1.5 T solenoidal field is maintained through the buncher. The irises of the pillbox cavities are closed with 200  $\mu$ m thick beryllium (Be) windows. The Be windows roughly double the cavity shunt impedance, and give a higher field on-axis for a given amount of rf power. Once the beam leaves the buncher, it consists of a train of bunches with different energies. The beam then is phase-rotated with a second string of 56 cavities with decreasing frequencies, but with constant accelerating gradient. The frequencies are chosen so that the

centers of the low-energy bunches increase in energy, while those of the high-energy bunches decrease. The algorithm [3] used for setting this condition is to keep the first reference particle at fixed momentum while uniformly accelerating the second reference particle through the rotator section, so that it attains the first particle’s energy at the end of the channel. This is accomplished by increasing slightly the phase shift between the reference particles by  $N_R = N_B + 0.05$ . With this condition, the bunches are aligned into nearly equal energies over the 42 m length of the rotator. The rf gradient is kept fixed at 13 MV/m while the rf frequency drops from 232 to 202 MHz. Similar to the buncher, the cavities occupy 0.5 m over a 0.75 m long cell and a 1.5 T solenoidal field continues throughout the section.

Upon exiting the rotator, the muons enter a ~100 m long cooling channel consisting of rf cavities, LiH absorbers for ionization cooling, and alternating 2.8 T solenoids for focusing. The cooling section has 0.75 m long cells and is identical to the cooling scenario used for the International Scoping Study [2]. Each cell has a 0.5 m long, 201.25 MHz rf pillbox cavity with a gradient of 16 MV/m. The 1.1 cm thick lithium hydride (LiH) absorbers are part of the cavity windows. LiH was chosen as the absorber material since it is a low-Z material, and hence has low multiple scattering per unit energy loss and gives good cooling performance. The side of the absorber facing the rf cavity is covered by a thin 300  $\mu$ m Be layer.

The performance of the front-end channel is evaluated by counting the number of simulated particles that fall within a reference acceptance, which approximates the expected acceptance of the downstream accelerator. Based on tracking simulations with the ICOOL code [4], at the end of the cooling channel we expect that the system accepts ~0.09 muons per 8 GeV incident proton, while the transverse rms normalized emittance falls by a factor ~3 to ~6 mm. The accepted rms longitudinal emittance is ~60 mm.

## OPTIMIZATION STUDIES

*Choice of magnets:* So far the baseline design assumes a constant 1.5 T magnetic field along the buncher and rotator. In a more realistic lattice, solenoidal coils at a certain periodicity,  $q$ , must be placed along those sections. The geometry of such a lattice is shown in Fig. 1 (a). The chief disadvantage of the periodic arrays is the presence of momentum stop bands, which restrict the usable operating range. This is shown in Fig. 1 where we plot the value of the transverse beta function as a function of the muon beam momentum for different periodicities. Note that in all cases the

coil axial length is 80% of the total periodicity of the cell. The presence of pass-bands is strong if the periodicity is 100 cm [Fig. 1(c)] or 150 cm [Fig. 1(d)] while they disappear if the periodicity is reduced to 50 cm [Fig. 1(b)]. In Fig. 2 we examine the performance of a Neutrino Factory front-end with 50 cm periodicity (solid line) versus a lattice with uniform field (dashed line). Our results show that the discrete case achieves same performance as the continuous one and thus is considered a viable choice for a Neutrino Factory.

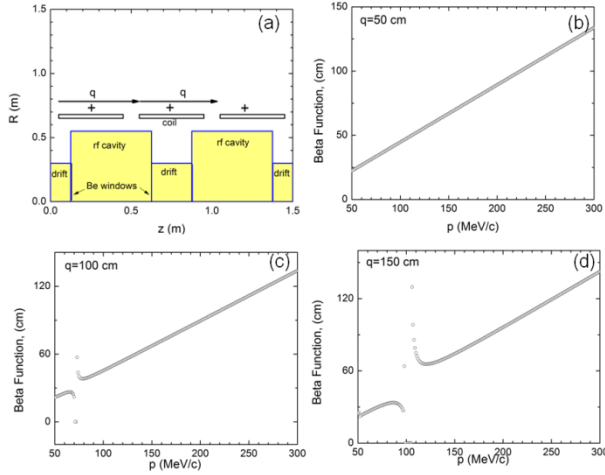


**FIGURE 1.** Coil discretization effect: (a) schematic layout of the buncher and rotator sections with parameter  $q$  indicating the periodicity of the coils; (b) transverse beta function versus momentum for  $q=50$  cm; (c) transverse beta function versus momentum for  $q=100$  cm, and (d) transverse beta function versus momentum for  $q=150$  cm;

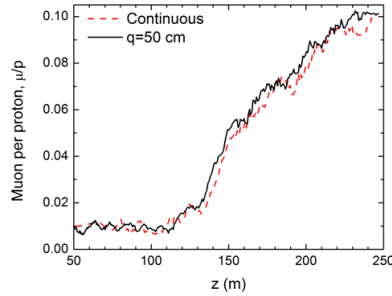


**FIGURE 2.** Accepted muon per proton rate versus distance for a lattice with a continuous solenoid (dashed line) and the case with periodicity  $q=50$  cm (solid line).

*Choice of frequencies:* As mentioned previously the front-end must be reoptimized for practicality and cost. First, in the baseline buncher simulations, 44 rf cavities were placed at 0.75 m intervals with each having a different frequency and a gradient matched to the formula shown in Eq. (1). In a more realistic implementation, the cavities need to be grouped into a smaller number of frequencies matched to input power sources. Thus, the arising question is how many rf

cavities can be grouped into a certain frequency without reducing the performance. In this section, we will attempt to answer this question and see how it will influence the performance of the front-end.

Figure 3 illustrates the accepted muons per incident proton when the cavities are grouped into 1-pair (baseline), 3-pair and 6-pair frequencies case. The simulations suggest that if the cavities are grouped into a pair of three, which corresponds to 33 discrete frequencies, then the accepted muon per proton rate is reduced by only 5%. However, if the cavities are grouped into a 6-pair configuration (12 discrete frequencies), the resulting muon per proton rate will drop by more than 20%. Another interesting observation is that although the baseline and 3-pair configuration can accomplish the same cooling rate, the 6-pair cooling performance is 15% worse since it achieves only 7.0 mm. We thus, choose to combine the cavities into a groups of three and Tables I and II show the selected frequencies and the corresponding average axial accelerating rf gradient in each frequency for the buncher and rotator, respectively.

The results presented so far have demonstrated that the rf can be grouped into a manageable number of frequencies without general loss of performance.

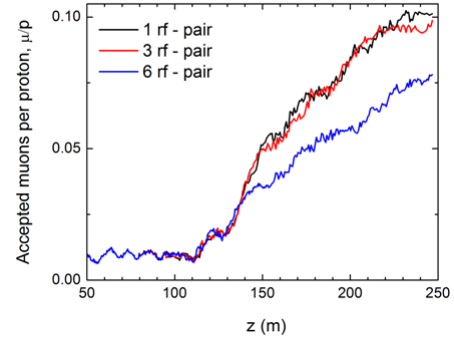


**FIGURE 3.** Effect of frequency grouping on the total number of accepted muons

*Cooling options:* From the way muons are produced, they inherently begin life in a beam with a very large phase-space volume. Ionization cooling therefore is necessary to transport the beam through a reasonable accelerator lattice [5]. In ionization cooling the fractional change in emittance is proportional to the fractional change in momentum arising from energy loss. Multiple scattering in the absorber material is a competing process that acts to increase the transverse emittance. The balance between those two processes determines whether the net cooling takes place. Clearly, one prefers to use absorbers where the product of the radiation length and the energy loss is large such as Lithium Hydride (LiH). Then, the only parameter

that is under our control is the beta function, which we want to keep as small as possible over the length of the absorber.

A key parameter that will determine the cooling rate is the width of the absorber. Thus, we attempt to vary the length of the absorber with the goal to find the optimum width that will maximize the cooling performance. In our simulation with ICOOL we assume a LiH absorber and Fig. 4(a) displays the accepted muon per proton rate versus absorber thickness,  $d$ . Clearly, the data suggest that the muon per proton rate is greatest if the absorber width is between 0.95-1.1 cm with a peak value at 1.0 cm.

As a cooler section employs more than 300 magnets it is likely that a small position uncertainty may arise so next we attempt to systematically examine the influence of those positioning uncertainties into the lattice performance. In order to study this we displace all the cooler magnets to different standard deviations of a Gaussian distribution and our results are shown in Fig. 4(b). The data suggest that that the channel managed to maintain its relatively high production ratio of muons per protons within the first 1-2 mm displacements. However, at larger displacements such as 5 mm the production of accepted muons drops by more than 50%.

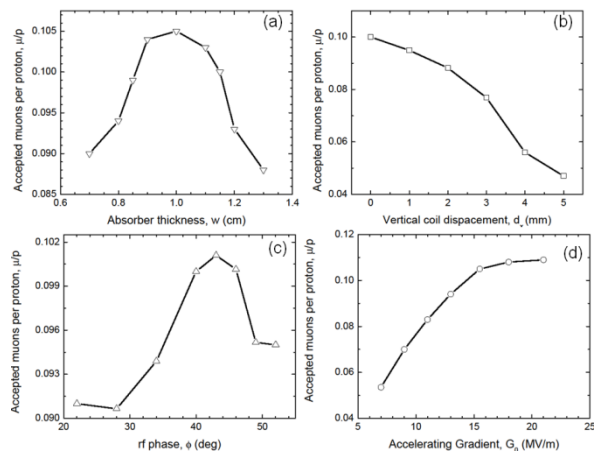


**FIGURE 4.** Dependence of accepted muons per proton from the: (a) absorber length, (b) alignment errors, (c) rf phase and (d) average rf gradient.

The electromagnetic field inside the cavity can be modeled by the time dependent equation  $G(t) = G_0 \cos(\omega t + \phi)$  where  $G_0$  represents the peak gradient of the field and  $\phi$  represents the rf phase. Typically we assume  $G_0$  to be 15.5 MV/m and the phase to be set at  $40^0$ . In Fig. 4(c) this phase is varied from 20 to  $55^0$ . We conclude that although the dependence of the muon per proton rate is weak, a

peak of the muon production rate can be seen at  $40\text{--}45^0$ .

In Fig. 4(d) we examine the consequences of using lower rf fields for the cooler section. This can be important as cavities tend to operate at lower gradients in the presence of 1 T or higher magnetic fields [6, 7]. The plot indicates, a gradient higher than 15 MV/m has little effect on the number of accepted muons. Since the cost scales with rf power and power scales with rf gradient it is therefore wise to use 15 MV/m as a optimum value for the cooler. On the other hand for values less than 15 MV/m the performance drops dramatically

## CONCLUSIONS

The sensitivity in performance of a Neutrino factory muon capture channel to variations in the design parameters was examined and some variation and constraints of the approach was discussed. For instance, we showed that the rf cavity can be grouped into an manageable number of frequencies and the collection and cooling can be developed within a practical set of parameters. In addition, we studied the lattice tolerance to magnet positioning errors and showed that a 1-2 mm displacement will not harm cooling whereas a displacement of 5 mm can reduce the final number of accepted muons by more than 50%. The rf fields and magnetic fields can now be specified to a level that a first order cost and practicality study can be implemented. While it is not yet certain what precise gradients or fields should be used, the numbers presented here can be useful as a basis in setting the scale for a Neutrino Factory front-end.

## REFERENCES

1. J. S. Berg, S. A. Bogacz, S. Caspi, et al., *Phys. Rev ST. Accel. Beams* **9**, 011001 (2006)
2. M. Apollonio et al., *Journal of Instrumentation* **4**, P07001 (2009).
3. D. Neuffer et al., Proceedings of the 1st International Particle Accelerator Conference, Kyoto, Japan, **WEPE068** (2010).
4. R. C. Fernow, Proceedings of the 1999 Particle Accelerator Conference, New York (IEEE, New York, 1999), p. 3020.
5. D. Neuffer, *Nucl. Instr. and Meth. Phys. A* **532**, 26 (2004).
6. D. Stratakis, R. C. Fernow, J. C. Gallardo, R. B. Palmer, and D. V. Neuffer, *Phys. Rev. ST Accel. Beams* **14**, 011001 (2011).
7. D. Stratakis, J. C. Gallardo, and R. B. Palmer, *Nucl. Instr. and Meth. A* **620**, p. 147 (2010)

# Progress Towards Parametric-Resonance Ionization Cooling in the Twin-Helix Channel<sup>\*</sup>

J.A. Maloney<sup>a#</sup>, B. Erdelyi<sup>a</sup>, V.A. Morozov<sup>b</sup>, Y.A. Derbenev<sup>b</sup>, R.P. Johnson<sup>c</sup>,  
and A. Afanasev<sup>d</sup>

<sup>a</sup>*Northern Illinois University, DeKalb, Illinois 60115, USA*

<sup>b</sup>*Thomas Jefferson National Accelerator Facility, Newport News, Virginia 23606, USA*

<sup>c</sup>*Muons, Inc., Batavia, Illinois 60510, USA*

<sup>d</sup>*The George Washington University, Washington, D.C. 20052, USA*

**Abstract.** Parametric-resonance Ionization Cooling (PIC) is proposed as the final 6D cooling stage of a high-luminosity muon collider. Combining muon ionization cooling with parametric resonant dynamics could allow an order of magnitude smaller final equilibrium transverse emittance than conventional ionization cooling alone. The same type of cooling channel can be used for Reverse EMittance EXchange (REME) to reduce the transverse emittance by another factor of ten. Together, PIC and REMEX can provide two orders of magnitude luminosity increase for a muon collider.

**Keywords:** parametric resonance ionization cooling.

**PACS:** 29.27.-a, 29.20.-c, 14.60.Ef, 41.85.Lc

## OVERVIEW OF PARAMETRIC-RESONANCE IONIZATION COOLING

Cooling presents a key challenge for the successful development of both a Higgs factory and muon collider. Because muons are produced as tertiary particles, a beam of a statistically acceptable number of muons will be produced with a large phase space volume. Cooling is required for acceptance into acceleration and storage structures in the machine, and reducing emittance improves luminosity from collisions. Longitudinal cooling is particular important for a Higgs factory. The need for muon cooling is complicated by the short lifetime of the muons, and non-linear effects from the complex magnetic fields of the cooling and transport channels. Ionization cooling techniques offer the best way to accomplish the substantial cooling needed within the limited muon lifetime. Parametric-resonance Ionization Cooling (PIC) is a proposed method for final stage 6D muon cooling that leverages resonance-driven strong focusing with ionization cooling to minimize angular divergence of muons in the beam.

Ionization cooling [1] is achieved by passing a particle through an energy-absorbing material, reducing the particle's momentum in all dimensions while RF fields restore longitudinal momentum. The angular divergence and energy spread are reduced

until they reach equilibrium with the stochastic effects of multiple Coulomb scattering and energy straggling. In PIC, a resonance is introduced in a period magnetic channel based on multiples of the betatron oscillation frequency. This allows the channel to reach a new equilibrium [2, 3]. The resonance perturbs the phase-space trajectories of particles at periodic locations along the channel changing their normal elliptical shapes to hyperbolic. At certain periodic focal points, muons in the beam become progressively narrower in position while diverging in angle as they pass down the channel. Without damping, the beam dynamics are not stable and the angular divergence of particles in the beam grows with every period. Placing energy absorbers followed by RF cavities at these focal points allows ionization cooling to limit the growth in angular divergence while maintaining total particle momentum and this stabilizes the beam motion. This resonance also causes a strong reduction of the beam spot size at the absorber locations leading to transverse beam emittance that is about an order of magnitude smaller than without the resonance. The longitudinal emittance is maintained through emittance exchange and shaped wedge absorbers. The absorber locations must be at points of small, but non-zero dispersion. A magnetic channel meeting the requirements for PIC could also be used for Reverse EMittance EXchange (REME) [4] by reversing the orientation of the wedge absorbers. This offers the potential of an additional reduction in transverse emittance by about another factor of 10 at the expense of longitudinal emittance.

---

\* Supported in part by U.S. DOE SBIR Grant DE-SC0005589.

# physics\_maloney@yahoo.com

One of the key principles for PIC is the correlated optics condition. Under this condition, a stable orbit for particles is maintained with betatron tunes in both the horizontal ( $\lambda_x$ ) and vertical ( $\lambda_y$ ) planes being low-integer multiples of the period of the dispersion function ( $\lambda_D$ ) for the system. The PIC also requires dispersion  $D$  such that is small, but non-zero, at the absorber to minimize energy straggling while allowing for emittance exchange to maintain constant longitudinal emittance. Thus, the optics must have correlated values such that  $a\lambda_x = b\lambda_y = c\lambda_D$  where  $a$ ,  $b$  and  $c$  are integers.

Because the PIC dynamics are very sensitive to non-linear aberrations from magnetic fringe fields, a solution using helical harmonics [5, 6, 7] has been proposed. To create dispersion in the channel two helical dipole harmonics having equal field strength and equal periods but opposite helicities are superimposed onto each other. Under this configuration, a reference muon maintains a stable orbit within the x-z midplane. A continuous straight quadrupole is superimposed to establish the correlated optics condition. It was demonstrated [6, 7] that a twin-helix channel could meet the correlated optics requirements while offering large dynamic aperture and momentum acceptance.

Beryllium wedge absorbers are added at every other periodic focal point in the channel for ionization cooling, followed shortly by RF cavities to restore and maintain the reference particle momentum. To induce resonances, two uncoupled pairs of helical quadrupole harmonics with very low field strength perturb the orbit at the focal points. For each pair of harmonics, like the primary helical dipole pair, the field strengths and periods are the same, but the harmonics in each pair have opposite helicities. One such pair is used to induce the resonance in the horizontal plane, while a second pair induces the resonance in the vertical plane.

## LINEAR MODELING IN COSY

Simulations for PIC have been performed with two different simulation codes [6, 7]. One set of simulations was performed using G4Beamline [8] (G4BL), a Geant-4 toolkit. The other used COSY Infinity [9] (COSY), a differential algebra based code that allow calculation of transfer and aberration maps for particles in the channel to arbitrary order. Because of its ability to turn on non-linear effects of various orders one at a time, COSY offers particular advantages for optimization and aberration correction. Additions to the basic beam physics package used with COSY had to be made to facilitate these simulations. These modifications included:

- Implementation of the magnetic field element for a helical harmonic pair of arbitrary harmonic order with potential for superposition of continuous straight magnetic multipoles of arbitrary order,
- Implementation of a fitting routine to determine the stable reference orbit for muon of a particular energy within the channel
- Implementation of the stochastic processes of multiple scattering and energy straggling in material
- Implementation of a particle tracking method for single particles and basic particle distributions.

Benchmarking was performed with G4BL to verify consistency of results between the two codes despite differences in the simulation methods [10]. With these modifications, simulation of the linear (first order) model of the channel was performed to verify that the simulation results were consistent with theory. The preliminary simulations were done without stochastic effects. A  $\mu^-$  with momentum of 250 MeV/c was chosen as the reference particle. The period of the helical dipole harmonic was arbitrarily set at 1 meter, and the field strengths for the harmonics and the straight quadrupole were scaled to achieve the correlated optics condition. Resonances were induced with a helical quadrupole harmonic pair (parametric lenses) for each plane that satisfied the correlated optics condition:  $\lambda_x = 2\lambda_y = 4\lambda_D$ . Simulation, shown in Fig. 2, verified that a test particle offset from the reference orbit in initial position and angle followed a hyperbolic trajectory as it travels down the channel.

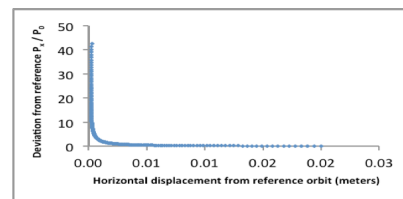


**FIGURE 1.** The basic twin-helix channel simulated in COSY with parametric lenses. Trajectory of a 250 MeV/c  $\mu^-$  launched offset in both planes from the reference orbit by 2 cm and 130 mrad is tracked every at every other focal point in the horizontal plane.

Next, beryllium wedge absorbers with a central thickness of 2 cm and a 30% thickness gradient were added at every other focal point. An idealized RF cavity was placed 3 cm after each absorber and tuned to restore momentum for the reference particle to maintain its stable orbit. Simulations for the same test particle, Fig. 3, show the effects of ionization cooling with and without using harmonics to induce the PIC resonance condition. With PIC resonances induced, strong focusing causes more reduction in the position

offset, and a much greater reduction in total offset after the same number of wedge absorbers.

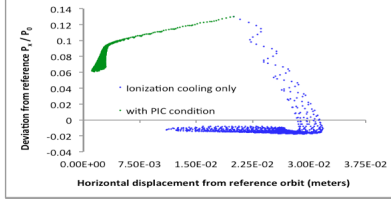


**FIGURE 3.** The full twin-helix channel simulated in COSY with and without PIC resonance. Trajectory of a 250 MeV/c  $\mu$ - launched offset in both planes from the reference orbit by 2 cm and 130 mrad is tracked at the center of each wedge absorber in the horizontal plane.

The stochastic effects of multiple scattering and energy straggling were added to the simulations to verify the equilibrium emittance and improved reduction in spot size predicted by theory. To implement multiple scattering, COSY calculates the path length each individual particle takes through the wedge absorber. This parameter,  $z$ , as well as the other parameters for that same particle and the absorber, are used to determine standard deviation for the “kick” to particle angle using the PDG formula RMS98 [11] modeling method (1). A random number generated from Gaussian distribution is used to determine the exact kick for the particle, and the result is split via polar angle between the horizontal and vertical plane. The calculated result is then applied to modify particle’s coordinates in the tracking subroutine. For energy straggling, a similar approach is used, with the Bohr approximation (2), determining standard deviation for the change in energy [12].

$$\theta_{\text{scatter}} = \frac{13.6 \text{ MeV}}{\beta c \rho} \sqrt{\frac{z}{\chi_0} \left( 1 + 0.038 \ln \left( \frac{z}{\chi_0} \right) \right)}, \quad (1)$$

$$\Omega^2_{\text{straggling}} [\text{KeV}^2] = .26 Z_{\text{absorber}} z N_t [10^{18} \text{ atoms/cm}^2]. \quad (2)$$

Where  $\chi_0$  represents the radiation length of the absorber material,  $Z_{\text{absorber}}$  is the absorber material’s atomic number,  $N_t$  is the atomic density of the absorber. Both processes are repeated for each individual particle every time the particle encounters an absorber in the channel. The results of these simulations for the horizontal plane are shown in Fig. 4 with and without the stochastic effects being included in the simulation. Even with the inclusion of these two important stochastic effects, cooling as predicted by the theory is observed [3, 7].

Simulations were also performed using an uncorrelated distribution of 1000 muons with the following standard deviations from the reference orbit: (1) offset in each plane: 2 cm.; (2) offset in angle in each plane: 130 mrad; (3) energy spread: 1%; and (4)

bunch length: 3 cm. The 6D emittance for total distribution was tracked as it travelled through the channel with and without inducing the PIC resonance condition. Fig. 5 shows the cooling factor, a figure of merit determined by dividing the final 6D emittance of the surviving particles in the beam by their initial emittance.

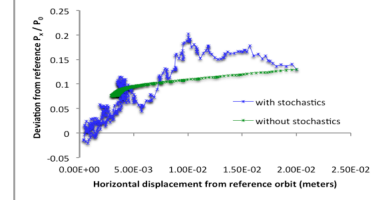


**FIGURE 4.** The full twin-helix channel simulated in COSY with and without the stochastic effects of multiple scattering and energy straggling. Trajectory of a 250 MeV/c  $\mu$ - launched offset in both planes from the reference orbit by 2 cm and 130 mrad is tracked at the center of each wedge in the horizontal plane.

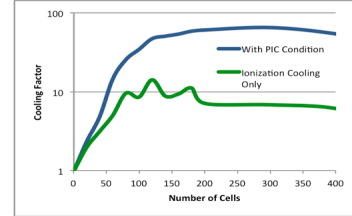


**FIGURE 5.** Comparison of cooling factor (ratio of initial to final 6D emittance) with and without PIC resonance.

As predicted by theory, 6D cooling with the PIC resonance condition reaches an equilibrium state that beyond that of ionization cooling alone by about a factor of 10.

## PROGRESS TOWARDS ABERRATION CORRECTION AND OPTIMIZATION

The baseline simulations described above provide an important tool for optimizing the PIC cooling channel. This linear model simulates the efficiency of the cooling channel where all aberrations have been perfectly corrected. Since muon beams can have a very large initial angular and energy spread, aberrations in the system dependent on these parameters can dramatically impact the final spot size of the beam.

To illustrate this, consider the progress towards aberration correction and optimization of the twin-helix channel. Through separate simulations, a preferred helical dipole harmonic period ( $\lambda_D$ ) of 20 cm was chosen for a reference momentum of 250 MeV/c, and the magnetic field strengths of the helical dipole

and straight quadrupole components scaled accordingly [4]. With COSY, the largest nonlinear aberrations in the system can be identified order by order, as well as their effects given a specified range in initial particle coordinates. This allows determination of a sensitivity of a system's optic to a range of initial beam parameters. For the twin-helix channel, Table 1 lists the largest 2<sup>nd</sup> and 3<sup>rd</sup> order aberrations affecting final spot size at the period focal points in the channel. The aberration ( $x|aa$ ), for example, shows how final horizontal position of the particle changes as a function of the square of its initial angle ( $p_x/p_0$ ) in the horizontal plane. Similarly  $b$  refers to initial angle ( $p_y/p_0$ ) in the vertical plane.

**TABLE 1.** Largest 2<sup>nd</sup> and 3<sup>rd</sup> order aberrations affecting spot size for the  $\lambda_D=20$  cm twin-helix.

Aberration	Magnitude [mm]
(x aa)	1.5
(x a $\delta$ )	2.1
(x aaa)	-17.8
(x abb)	-6.1
(y aab)	6.1
(y bbb)	1.2

Studies are currently ongoing to correct these and other significant higher order aberrations in the twin-helix channel using continuous magnetic fields, including higher order helical harmonic pairs and straight multipole fields. In all cases, the correlated optics condition must also be maintained, and the reference orbit must be recalculated since these higher order magnetic fields can modify the orbit of the reference particle. Field strength, phase offset, helicity and harmonic number provide a number of variable parameters for the system.

One such correction scheme minimizing all 2<sup>nd</sup> and 3<sup>rd</sup> order aberrations that contribute to deviation in the final position of the particle at each wedge absorber uses a straight octopole field, two pairs of helical sextupole harmonics and two pairs of helical octopole harmonics. Two pairs of helical quadrupole harmonics are also used to maintain the correlated optics in the channel. Fig. 6 shows a 3<sup>rd</sup> order simulation of this system after 20 cells.

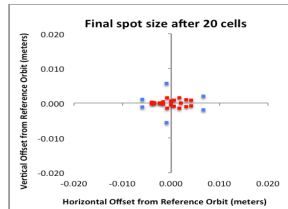


**FIGURE 6.** Tracking for concentric cones, with angular deviation of up to 120 mrad, of 250 MeV/c muons launched on reference orbit in COSY with non-linear effects through 3<sup>rd</sup> order and stochastic effects.

Particles shown in blue survive in the channel without corrections, while those shown in red show effects of the correcting magnetic fields. Survivability of muons has dramatically increased as well as focusing of the beam. Aberrations beyond 3<sup>rd</sup> order still need to be corrected.

## CONCLUSIONS AND FUTURE WORK

PIC combines muon ionization cooling with parametric-resonance dynamics to allow final equilibrium transverse beam emittance that is an order of magnitude smaller than those achievable with conventional ionization cooling alone. Linear simulations including stochastic effects have verified the predictions of PIC theory. Using the same magnetic channel, REMEX could allow reduction in transverse emittance by another factor of ten. Thus, PIC and REMEX together provide the potential to increase luminosity by two orders of magnitude.

A twin-helix magnetic channel with correlated optics has been developed for PIC. A basic model of a PIC channel with absorbers and RF cavities has been simulated in G4BL and COSY. Linear simulations in COSY have confirmed the model's validity with stochastic effects included. Compensation of beam aberrations is a challenging aspect of this channel and will be required for complete demonstration of PIC. Progress has been made on this problem and ongoing efforts continue.

## REFERENCES

1. D. M. Kaplan, in Proc. Snowmass 2001, eConf C010630 (2001) M102.
2. Y.S. Derbenev and R.P. Johnson, Phys. Rev. ST Accel. Beams 8, 041002 (2005).
3. Ya. S. Derbenev et al., arXiv:1205.3476v1 [physics.acc-ph].
4. V.S. Morozov et al., in Proc. AAC'12.
5. V.S. Morozov et al., AIP Conf. Proc. 1299 (AIP, Melville, NY, 2010), p. 664.
6. V.S. Morozov et al., in Proc. IPAC'12, New Orleans, LA, WEP005, p. 2729.
7. J.A. Maloney et al., in Proc. IPAC'12, New Orleans, LA, TUPPD011, p. 1428.
8. G4beamline, <http://g4beamline.muonsinc.com>
9. K. Makino and M. Berz, Nucl. Instrum. Meth. A 558, 346 (2005).
10. V.S. Morozov et al., in Proc. IPAC'11, San Sebastian, Spain, WEPZ009, p. 2784.
11. H. Bichsel, et al., Particle Data Group (C. Amsler et al., Phys. Lett. **B** 667, Ch 27 (2008)).
12. N. Bohr, K. Dan. Vidensk. Selsk. Mat. Fys. Medd. **18**, No. 8 (1948).